Time Resolved Ultrafast Dynamic Excitations in Semiconductors

by

THOMAS ROGER

A thesis submitted to the
University of Birmingham
for the degree of
Doctor of Philosophy

Nanoscale Physics Research Laboratory
School of Physics & Astronomy
University of Birmingham
B15 2TT
September 2012

Abstract

A set of novel time-resolved techniques are presented to probe the transient carrier dynamics of semiconductors. The techniques are particularly useful for opaque, multi-layer and multi-phase samples. Multiple incidence angle reflectometry measurements have been used to measure the plasma frequency, scattering rate and effective mass of carriers shortly after optical excitation, but prior to significant recombination. For samples of nano structured silicon embedded in an amorphous silicon matrix (*nc-Si:H*) values of $\omega_p = 1.2^{+0.3}_{-0.2} \times 10^{15}\mathrm{s}^{-1}$, $\Gamma = 2^{+1.2}_{-1} \times 10^{15}\mathrm{s}^{-1}$ and $m_{\mathrm{eff}} = 0.17$ are found, in good agreement with those found in similar optical, time-resolved studies. Time-resolved scattering and reflectivity measurements have been used to measure the characteristic timescales of carriers within samples of *nc-Si:H*, we find a decay time of carriers within the nano crystals of $\tau_{dec} = 2.2 \pm 0.2$ps, a recombination time in the matrix of $\tau_{rec} = 22 \pm 2$ps and a transfer of carriers initially excited into the nano-crystals to the amorphous matrix of $\tau_{trans} = 4 \pm 0.7$ps. These compare well with timescales measured in the bulk α-*Si* and *nc-Si* samples.

A time-resolved ellipsometry technique has been developed using a home-built and calibrated ellipsometer. The design and optimisation of the ellipsometer has been chosen carefully to study low absorption materials. The ellipsometric angles (Ψ and Δ) are measured in good agreement with commercial ellipsometry equipment. An optical model is constructed to find accurately the thin film thickness' and dielectric function dispersions of the complex multi-layer samples. The values are then fit as a function of time allowing measurement of the transient change in dielectric function. The changes of complex dielectric function are modelled using a Drude approximation revealing interesting behaviour of the scattering processes and carrier concentration in samples of *nc-Si:H* and silicon nitride (SiN_x). In samples of *nc-Si:H* we find that the carriers adopt a classical distribution through analysis of the Fermi integrals and that recombination processes conserve the average temperature of electrons, suggesting that there is no preference for recombination of carriers with higher energies. This is contrary to current understanding of carrier dynamics in bulk semiconductors.

I would like to dedicate this thesis to my friends and family...

Acknowledgements

I would like to thank Dr. Andrey Kaplan for his encouragement and support throughout my PhD, Dr. Dimitri Chekulaev and Dr. George Barreto for their expertise and assistance in the lab, Dr. Igor Yurkevich for useful discussion and assistance with theoretical modelling, Dr. James Bowen for his assistance with ellipsometry measurements, the NPRL group members past and present and Sasha Argunova for her understanding, support and patience. Finally I acknowledge funding through the Engineering and Physical Sciences Research Council (EPSRC) and equipment supplied through the Advantage West Midlands, Science City projects.

Contents

List of Figures

List of Tables

Nomenclature

Roman Symbols

ρ	Ellipsometric Ratio
nc-Si:H	Nanocrystalline Silicon Embedded in Hydrogentaed Amorphous Silicon
CPM	Constant Photocurrent Method
EMA	Effective Media Approximation
FB	Forouhi-Bloomer Model
FCA	Free Carrier Absorption
HHG	High Harmonic Generation
MSE	Mean Square Error
PECVD	Plasma Enhanced Chemical Vapour Deposition
PL	Photoluminscence
QD	Quantum Dot
RAE	Rotating Analyser Ellipsometry
RAEC	Rotating Analyser Ellipsometry with Compensator
RCE	Rotating Compensator Ellipsometry
SE	Spectroscopic Ellipsometry
SEM	Scanning Electron Microscopy

SNR	Signal-to-Noise Ratio
VHF-GD	Very High Frequency-Glow Discharge
VMI	Velocity Map Imaging
XRD	X-ray Diffraction

Chapter 1

Introduction

Ultrafast operations and processes are generally considered to be those operating on the femtosecond timescale, a unit of time equal to 10^{-15}s. To explore fundamental atomic processes on timescales as short as a few femtoseconds, one requires equipment with characteristic operating times of the same order. In the field of optics this usually implies the use of ultrafast pulse lasers [1]. Due to the large concentration of energy when a pulse of light is *squeezed* into this ultrafast regime, it is not only short lived events that can be studied but also interactions of intense light with matter and the resultant transient behaviour of atoms and molecules. So why are ultrafast pulses interesting to study? To answer this question it is useful to consider the length scales that are being dealt with. In one femtosecond a visible light pulse can travel a distance of several hundred nanometers. Obviously this distance is inconsequential in our everyday lives, however this corresponds to many thousand atomic distances (atomic distance $\sim 1\AA$), such that light interacts with thousands of atoms in just 1fs and the their response is averaged. Thus, as a femtosecond pulse interacts over this length scale we can see how this time scale may shed light on much larger, macroscopic processes. In fact many processes on the atomic scale progress on the sub-picosecond timescale. So it is important to study physical systems operating in the ultrafast regime as many of these processes are the initial steps of important mechanisms in physics, chemistry and biology.

A plethora of techniques have emerged over the past few decades, harnessing the power of emergent ultrafast optical technologies, these include; velocity map imaging (VMI), high harmonic generation (HHG), a multitude of pump-probe spectroscopy techniques, terahertz pulses and z-scan measurements to name just a few. The choice of technique is simply down to what physics one wishes to study. For example velocity map imaging provides a means to probe photoelectron processes in a wide variety of atoms and molecules [2]. This thesis concentrates on the inherent ability of ultrafast optical pulses to probe electron dynamics in semiconductor materials in a manner not achievable previously. This is performed by a set of reflectivity-based spectroscopic measurements. In particular we are interested in the excitation, transport and recombination processes of carriers that are optically excited [3–6]. This means resolving the energy distribution of carriers as a function of time following stimulus from an optical excitation. This is no easy feat, requiring careful and deliberate experiments to be performed which shed light on the surprising physics involved on the femtosecond timescale.

1.1 Review of Carrier Dynamics in Semiconductors

Events that occur in the ultrafast time regime are considered microscopic. These events are the building blocks of macroscopic processes that appear to progress on a relatively slow time frame. The processes governed by these microscopic events are numerous and diverse in their nature; in this thesis the focus will be on the transient electron dynamics on surfaces occurring on the femto- and pico-second time scale. Due to advances in ultrafast technology it is now possible to study the fundamental mechanisms and characteristic time scales in solids at room temperature. Their importance lies predominantly in the optimisation and miniaturisation of semiconductor devices used in modern day electronics [7–11]. The following is a brief description of the present understanding of ultrafast processes following optical excitation into non-equilibrium states.

In bulk semiconductors an excitation of free carriers into states above the band gap is achieved by an incident pump (excitation) pulse with frequency $\omega_{eh} > \omega_{gap}$. In direct band gap semiconductors the energy distribution of the carriers initially resembles that of the excitation spectrum, with a mean excess energy $\Delta E = \hbar(\omega_{eh} - \omega_{gap})$. Thermalisation occurs, when the excitation density is large, through carrier-carrier scattering,

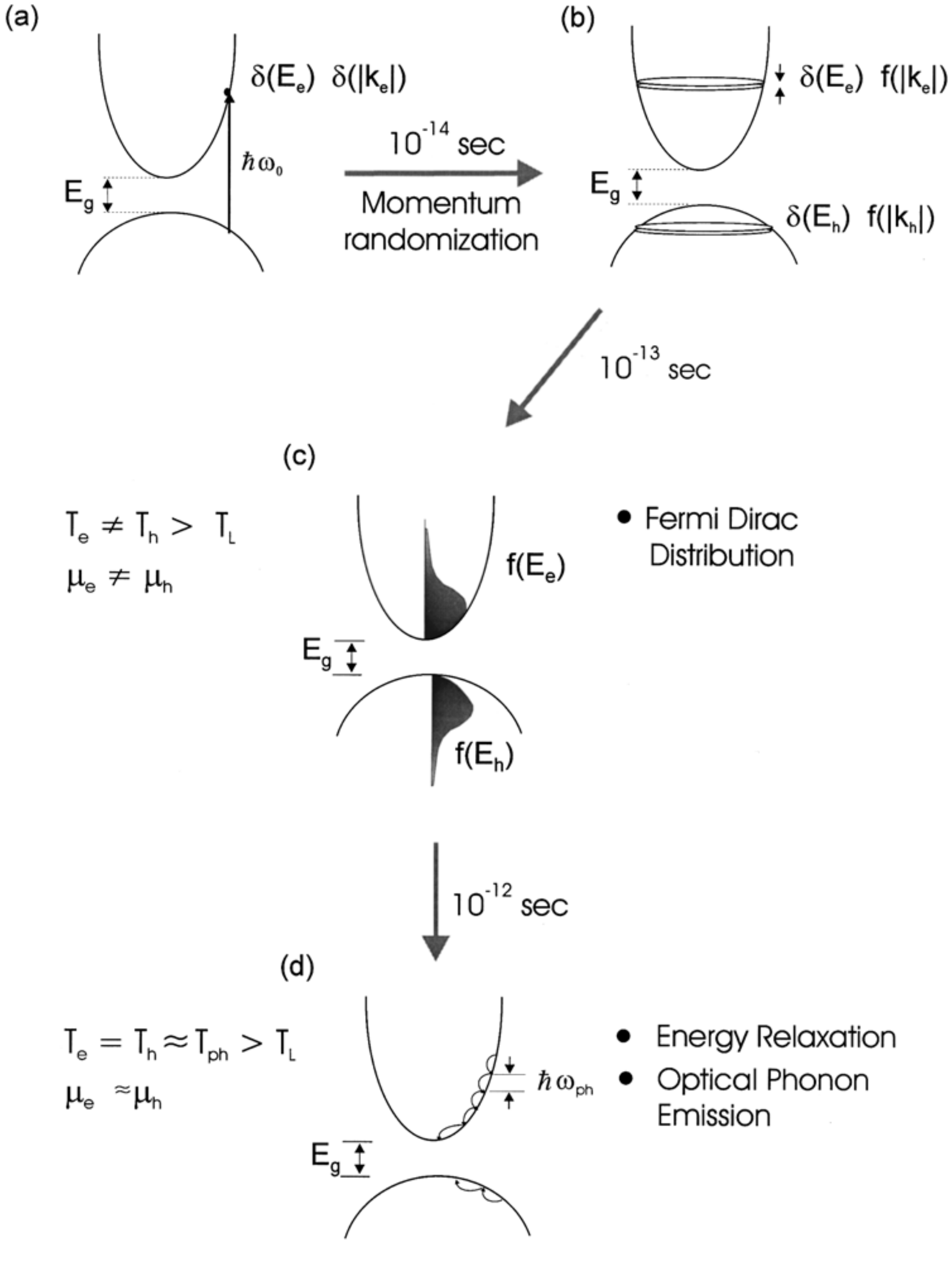

Figure 1.1: A schematic diagram illustrating the photoexcitation of a semiconductor and subsequent energy relaxation. After photoexcitation with polarized light, the carriers have delta function distribution in momentum and energy space (a). Within tens of femtoseconds momentum randomization occurs (b). Thermalization of carriers into a Fermi-Dirac distribution occurs for carrier densities greater than 10^{19} cm^{-3} via collision between carriers on the sub-picosecond timescale [10^{-13} s] (c). As time evolves the hot carriers lose their excess kinetic energy while attempting to reach thermal equilibrium with the lattice through optical phonon scattering (d). [12]

conserving the mean carrier energy. This thermalisation means that carriers scatter out of their initial states, which has the effect of broadening their energy distribution. However for nano-structured or amorphous semiconductors scattering of the carriers may proceed via interactions with defect states, phonons or boundaries between different phases of the material. In fact very little is understood about the scattering mechanisms in these kind of complex structured samples [13–17]. The temperature attributed to the thermalised carriers can be far greater than that of the lattice. This energy can be transferred to the lattice by carrier-phonon scattering, resulting in carriers relaxing into lower states in the conduction (valence) band. The Fermi distribution is reached when the temperature of the carriers is equal to that of the lattice (thermal equilibrium). If the initial energy density is high a *local* increase in temperature of the lattice can readily be observed [12]. Above a certain threshold this can induce melting of the lattice [18]. The processes here are shown schematically in figure 1.1.

It is widely accepted [19] that carrier-carrier scattering in bulk materials occurs over the first 10fs or less, relaxation of the carriers into lower states in the band and subsequent interband transitions can then ensue over the course of several nanoseconds. However in this study it is shown that nano-structuring of semiconductors can alter these characteristic time scales. Many studies have been carried out to investigate how changes of the optical properties of a sample can provide knowledge of the transient nature of surface electron dynamics [20–22]. Since the development of ultrashort pulse sources there has been considerable research into electron dynamics and optically-induced ‘phase transitions’ in dielectrics, semiconductors and metals [23–27]. The pioneering work performed by Shank *et al.* [19] investigated the effect of increasing the carrier density N_{eh} on the optical properties of crystalline silicon. The contribution of the electron-hole (e-h) plasma to the reflectivity of the sample is estimated by a simple Drude model expression for the refractive index of the plasma [19].

$$n_p = n_c(1 - \omega_p^2/\omega^2)^{1/2} \tag{1.1}$$

Here, n_p and n_c are the refractive indices of the plasma and unpeturbed crystalline silicon respectively, ω_p is the e-h plasma frequency and ω is the frequency of the incident probe light. It is important to note here that in the work of Shank (and many others) the imaginary component of the refractive index is omitted from the theory, these kind of assumptions cannot be made for more complicated samples [28–31]. From Eq. 1.1 it can be seen that as the probing frequency ω is increased above that of the e-h plasma frequency ω_p the refractive index and hence reflectivity decreases. In this case, taking a measurement of $\Delta n_p(\tau)$, where τ is the time delay with respect to the excitation, provides a method to estimate the e-h plasma frequency,

$$\omega_p = (N_{eh}e^2/m_e\varepsilon_0)^{1/2}, \tag{1.2}$$

where m_e is the free electron mass and ε_0 is the permittivity of free space. In order to relate this to a measurable property of the sample one must look at the reflectivity, absorption or transmission of the sample.

Sabbah and Riffe [32] propose that there are two linear contributions to the measured reflectivity change $\Delta R/R$: changes in the dielectric function due to free carriers in the conduction band and changes to the dielectric function due to interband transitions. The free carrier contribution can be described by a Drude model expression as seen in Shank's work [19]. While the interband contribution can be attributed to state filling, lattice temperature changes and band-gap renormalisation. For samples where $\Re(\varepsilon) \gg \Im(\varepsilon)$ and $\Re(\Delta\varepsilon) \geq \Im(\Delta\varepsilon)$ one can assume that the contribution to the change in reflectivity is only due to the real part of the dielectric function. Hence the change in reflectivity can be linked via Fresnel formulae to the real part of the refractive index, n, by;

$$\frac{\Delta R}{R} = \frac{4n_0\cos(\phi)}{(n_0^2-1)(n_0^2-\sin^2(\phi))^{1/2}}\Delta n_p, \tag{1.3}$$

where ϕ is the incidence angle and n_0 is the refractive index of the ambient medium. However, if one were to attribute the change in optical constants to both the real and imaginary parts of the complex refractive index (as we will see later) a more sophisticated approach should be taken. A method to resolve the real and imaginary parts of the refractive index based on the reflectometry procedure has been proposed by Roeser *et al.* [33], in which multiple incidence angles are used to fully resolve the complex dielectric function.

Prominent work in the study of semiconductor electron dynamics over the past few decades has relied heavily on modelling using the Drude model. Using this approximation, which describes the dielectric function's response to excitation of free carriers, it is possible to model the carriers plasma frequency and scattering rate. In the paper by Sokolowski-Tinten and von der Linde [34] a comprehensive study of the electron dynamics in silicon are presented. The data is fitted quite accurately with a Drude model response for free carrier absorption. For an excitation density of $10^{22} cm^{-3}$, probed at a wavelength of 625nm, the authors are able to estimate the optical mass $m_{opt} = 0.15$ and damping time of the carriers $\tau \approx 1$fs. These values are in fair agreement with other high carrier density measurements [35, 36] and theoretical studies [15, 37]. Other mechanisms for changes in the optical properties of the sample, such as; state and band filling as well as band gap renormalization are given little weight.

Silicon photonics, the technology giving optical functionality to silicon has recently had a resurgence corresponding to the advent of nano-structured samples with tuneable size and shape morphology. This nano-structuring has been adopted in order to realise the potential of silicon for various devices, such as; computing (waveguides, modulators, sources and detectors), photo-voltaics, sensing, optical resonators, etc [38]. Therefore an understanding of the charge dynamics in these types of materials is crucial in order to understand how these devices should be fabricated. Despite extensive studies of silicon nanocrystal materials there have been only a few attempts to understand the carrier dynamics in these types of materials [39–42]. Terahertz spectroscopy has been widely used to study nano-structured silicon due to its inherent ability to measure processes occurring on these scales, this is because their interaction length is of the same order as typical dimensions of embedded nanocyrstals. The measurable length scale is given by $L_\omega = \sqrt{D/\omega}$, where D is the diffusion coefficient of carriers in the material and ω is the probing frequency [43]. At terahertz frequencies this implies L_ω =2-10nm. Studies of nano crystalline silicon embedded in hydrogenated amorphous silicon (*nc-Si:H*) have shown non-Drude like behaviour over this extremely wide probing range [44]. These techniques benefit from access to both the real and imaginary components of the conductivity. The Drude like behaviour, seen in bulk crystalline silicon, is modelled alongside the non-Drude behaviour of *nc-Si* within the construct of the Drude-Smith model, where the complex conductivity is given by,

$$\sigma^*(\omega) = \frac{\sigma_0}{1 - i\omega\tau}\left[1 + \sum_{n=1}^{\infty} \frac{c_n}{(1 - i\omega\tau)^n}\right]. \tag{1.4}$$

Here $\sigma_0 = e^2 n_\mathrm{f} \tau / m^*$ is the dc conductivity, with n_f being the free carrier density, m^* is the effective mass, τ is the collision rate, and ω is the frequency of the excitation. The coefficient c_n represents the fraction of the carriers initial velocity that is retained after the n$^{\mathrm{th}}$ collision. Knowledge of the conductivity and scattering rate provide invaluable information when designing silicon photonic materials [38]

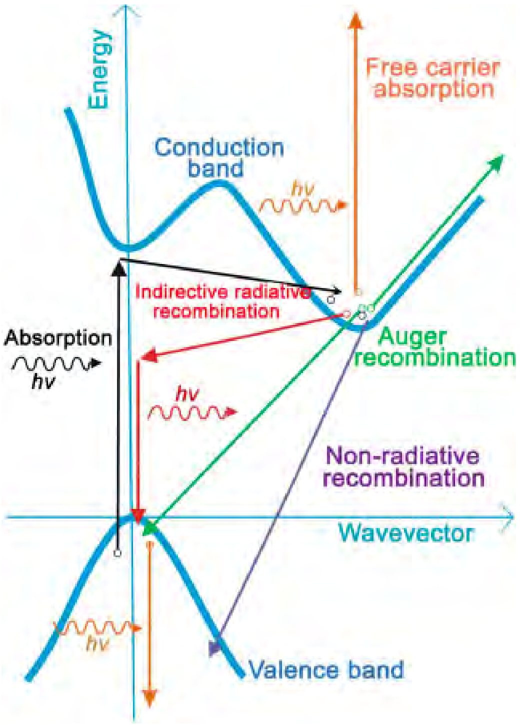

Figure 1.2: Energy band gap scheme for silicon. The arrows indicate the paths available for excitation and recombination of carriers. Black arrows: indirect absorption. Red arrows: phonon assisted (indirect) non-radiative recombination. Blue arrow: non-radiative recombination. Green arrows: Auger recombination. Orange arrows: free-carrier absorption mechanism. [38]

There is a general belief that in order to take silicon photonics to the next level there needs to be improvements in all-silicon active devices [38]. Despite improvements through hybrid technologies and ion implanted materials, research is focussed on micro- and nano-crystalline silicon embedded in hydrogenated amorphous silicon. Perhaps the device that encapsulates this desire for an all silicon material most, is that of a silicon laser. It is important therefore to understand why photoemission is so difficult to achieve in silicon materials [45]. The issue here lies in the band structure of silicon, it's indirect band gap, shown in Fig 1.2, means that radiative recombination of electrons and holes requires a momentum conserving phonon, thus e-h pairs have relatively long lifetimes. This is coupled with a generally large diffusion length for carriers (typically a few μm) making it likely that carriers encounter luminescence killing centres, such as defects, before they are likely to recombine [20].

However, there are certain systems of silicon for which these problems can, to some extent, be overcome. With the advent of nanocrystalline silicon (*nc-Si:H*), whose shape and size morphology can be well controlled, photoluminescence has become possible [46]. In order to achieve this kind of emission it is required that the crystalline phase is retracted to just a few nm. It has be shown that the efficiency of this emission are a consequence of the particle-in-a-box argument for an infinite quantum well, in which as the spatial confinement of the box is increased, the overlap of the e-h wavefunctions becomes larger, leading to an increase in the probability of radiative emission. Furthermore, due to the spatial confinement of the carriers, the diffusion length is restricted making it less likely for the carriers to encounter defects. As a result of the nanostructuring of silicon, the linear and nonlinear optical properties of the sample can be wildly altered [46, 47].

The nonlinear response of *nc-Si:H* has been of particular interest due to the possible applications in all-optical switching and other photonic devices [48–50]. Ma *et. al.* describe a z-scan measurement of *nc-Si:H* in which they show the tuneable nonlinear absorption properties of the sample at photon energies slightly below the band gap. Here they propose that photons below the band gap create carriers that are excited into the Urbach tail states via a phonon-assisted transition. However as the photon energy approaches the band gap they believe either two-photon absorption or free carrier absorption may then occur, leading to the nonlinear behaviour seen in some of these materials.

1.2 Summary of Current Understanding

The literature published over the past few decades describes a mechanism of optical carrier excitation and decay depicted as follows. Initially the carriers are excited above the band gap with a distribution equal to the excitation spectrum. Over the first few femtoseconds the carriers thermalize through electron-electron collisions transferring energy between each other until an equilibrium is reached, this can take the form of either a classical Boltzmann distribution [37] or a quantum Fermi-Dirac distribution [12]. The dependence on which route the system proceeds, in order to assume this distribution is unclear [37]. The carriers reach their destined distribution after $\sim 10^{-13}$s with equal temperature for electrons and holes $T_e = T_h$ but different chemical potentials $\mu_e \neq \mu_h$ (see Fig. 1.1). It is widely believed that over the following picoseconds (10^{-12}s), the carriers lose energy and relax toward the band extrema releasing optical phonons, heating the lattice. Recombination processes in bulk [4, 51] and surface states [52] transfer electrons back to the valence band on timescales longer than the lattice equilibrium time (i.e. the time in which carriers and the lattice have reached thermal equilibrium) [53–55]. We aim to show, over the course of this thesis, that this picture of carrier excitation and relaxation is not always valid.

Chapter 2

Novel Semiconductor Materials

The following is a summary of two samples that have shown particularly interesting phenomena. The first is a composite material of nano-crystalline silicon spheres embedded in a matrix of amorphous silicon, a material that has been developed as a novel absorber for future solar cell technologies. The second is a sample of silicon nitride, which exhibits photoluminescence over a relatively wide bandwidth. The fabrication and basic characteristics of each sample are discussed.

2.1 Crystalline Silicon Inclusions Embedded in Hyrdogenated Amorphous Silicon (*nc-Si:H*)

Samples of nano (micro) crystalline silicon embedded in a hydrogenated amorphous silicon matrix (*nc-Si:H*) were supplied by Sirica DC (Israel) and were fabricated via a plasma enhanced chemical vapour deposition (PECVD) method and characterised at the Institute of Microtechnology (IMT) in Switzerland. The technique was initially perfected by Veprek and Marecek [56] to fabricate hydrogenated microcrystalline silicon μc-Si:H. Later, Usui *et. al.* [57] and Spear *et. al.* [58] published what is now the standard form for PECVD. The precise details and parameters of this technique can be found elsewhere [59]. Nanocrystalline formations are grown in an amorphous silicon matrix by controlling the ratio of hydrogen H_2 to silane SiH_4. The authors state that this ratio, $[SiH_4]/[SiH_4 + H_2]$, controls the size and morphology of the crystallites. The sample, shown in Fig 2.1, consists 500-nm-thick layers of hydrogenated amorphous sil-

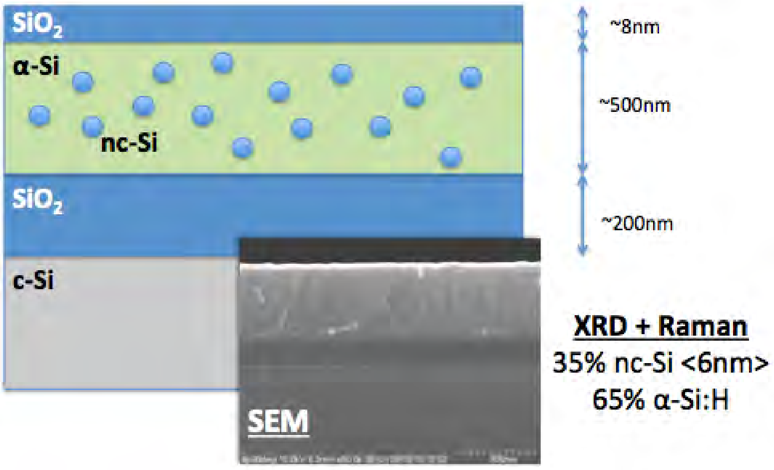

Figure 2.1: Multi-layer structure of a sample of nano crystalline silicon embedded in an amorphous silicon matrix (*nc-Si:H*). The sample substrate is a crystalline silicon wafer with a ∼200nm layer of silicon dioxide. The *nc-Si:H* layer is approximately 500nm thick, consisting of 35% spherical inclusions of *nc-Si* with an average diameter of $\langle a \rangle = 6$nm. The sample was prepared by Sirica DC (Israel) in conjunction with the Institute for Microtechnology (IMT)

icon (α-*Si:H*) containing nanocrystalline silicon *nc-Si* (not visible in the SEM image due to similar dielectric constant of the two phases of the composite material). A crystalline silicon substrate covered by 200nm of silicon oxide was used to grow the layers. We used standard methods of micro-Raman and XRD [60–62] analysis (see appendix A) to estimate that about 35% of the total layer volume was occupied by *nc-Si* with a mean diameter of <a> = 6 nm.

Figure 2.2 shows a typical absorption spectra for the samples of micro/nano- crystalline silicon described here, this is plotted alongside curves for a crystalline silicon wafer and intrinsic hydrogenated amorphous silicon. It shows that μc-Si:H (nc-Si:H) closely follows the curve of *c-Si*, with a slight red-shift. It is believed that the red-shift occurs due to scattering from the rough μ*c-Si:H* layer [64]. Furthermore, at energies $\geq$ 1.8eV there may also be a contribution due to absorption within the amorphous phase. The samples produced by Vallat-Sauvain *et. al.* [59] are part of research into materials which may be used as novel absorbers in thin-film solar cells. The materials are designed with respect to their spectral response, photodegradation stability and other basic solar cell parameters.

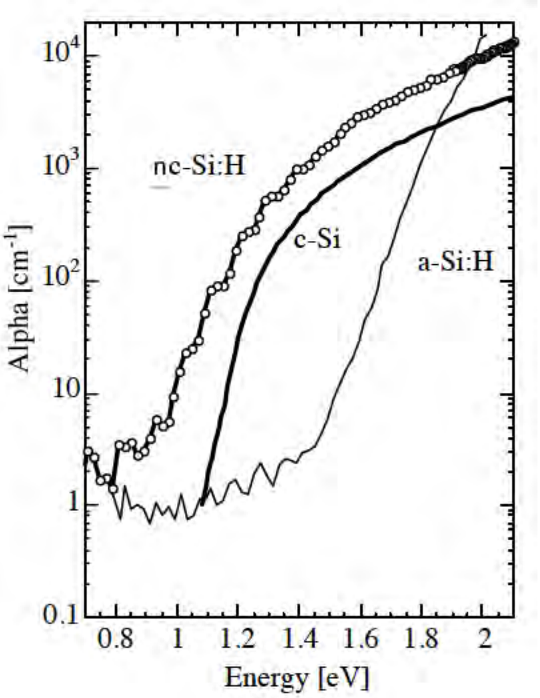

Figure 2.2: Optical absorption of a μc-Si:H layer deposited by very high frequency-glow discharge (VHF-GD). The measurement was made by constant photocurrent method (CPM) in [63] and is compared with measurements of amorphous and crystalline silicon.

2.2 Silicon Nitride (SiN_x)

As discussed in Sec. 1.1 quantum confinement of silicon nanostructures has provided a breakthrough in electro-optical devices [65]. Due to the enhanced radiative recombination rate of electrons and holes, a wide range of luminescence wavelengths has been observed in porous and nano-crystalline silicon [66]. Due to the structural disorder of amorphous silicon, along with its intrinsically higher band-gap (1.6eV) compared to that of crystalline silicon (1.1eV), the luminescence efficiency is much greater [67]. These effects are advantages when producing light of wavelengths in the blue and shorter spectral region. The dependence of the luminescence properties with size and morphology of the amorphous silicon quantum dots (α-Si QD) also lead to important information with regard to the carrier mobility. In fact there is relatively little known about transport properties of carriers in these types of samples compared to crystalline silicon [68].

Primarily it has been left to theoretical works to study α-Si quantum structures

[69, 70]. The issue here is that it is very difficult to grow truly zero-dimensional α-*Si* QD structures. Generally standard amorphous silicon samples suffer from natural defects that act to quench radiative recombination. Therefore it is seen of upmost importance to create α-*Si* QD's of high quality when studying the origin of light emission and quantum confinement. Silicon nitride is an excellent matrix for use with these α-*Si* QD's due its lower tunnelling barrier compared to a silicon dioxide (SiO_2) matrix [71–73]. The samples discussed in this thesis are grown with a technique based on the processes developed by Park *et. al.* [68, 74].

Table 2.1: Table of experimental parameters detailing the values used in the plasma enhanced chemical vapour deposition (PECVD) routine to fabricate samples of SiN_x and GaAs.

Sample	SiH_4 $[\frac{cm^3}{min}]$	N_2 $[\frac{cm^3}{min}]$	NH_3 $[\frac{cm^3}{min}]$	N/Si [%]	E_{PL} [eV]	ΔE_{PL} [eV]	I_{PL}^{532nm} [%]	I_{PL}^{405nm} [%]	E_T [eV]	E_U [meV]	d [nm]
SiN_x 276	16	20	181	84	1.55	0.53	469	1470	2.32	190	440
GaAs	-	-	-	-	1.4	0.03	100	100	-	-	∞

Samples of SiN_x, obtained from Sirica DC (Isreal), are prepared via plasma enhanced vapour deposition (PECVD), in which ammonia (NH_3) is used as a source of nitrogen (N_2), which is diluted in silane and used along with pure nitrogen gas (99.9999%) as the reactant gases [74]. Silicon wafers are used as the sample substrates. Details of the flow rate, total pressure, plasma power and growth temperature can be found from Ref. [76]. A full list of the deposition parameters and optical constants are listed in table 2.1. Additional N_2 gas is used to control the growth rate of the silicon nitride film, in turn controlling the size and morphology of the α-Si QD structures. Fig. 2.3 show the PL response of the sample used in these studies. SEM measurements confirm a film thickness of 440nm for the silicon nitride layers. Further information regarding this sample, such as; absorption spectra, SEM images and time-resolved photoluminescence can be found in Appendix B.

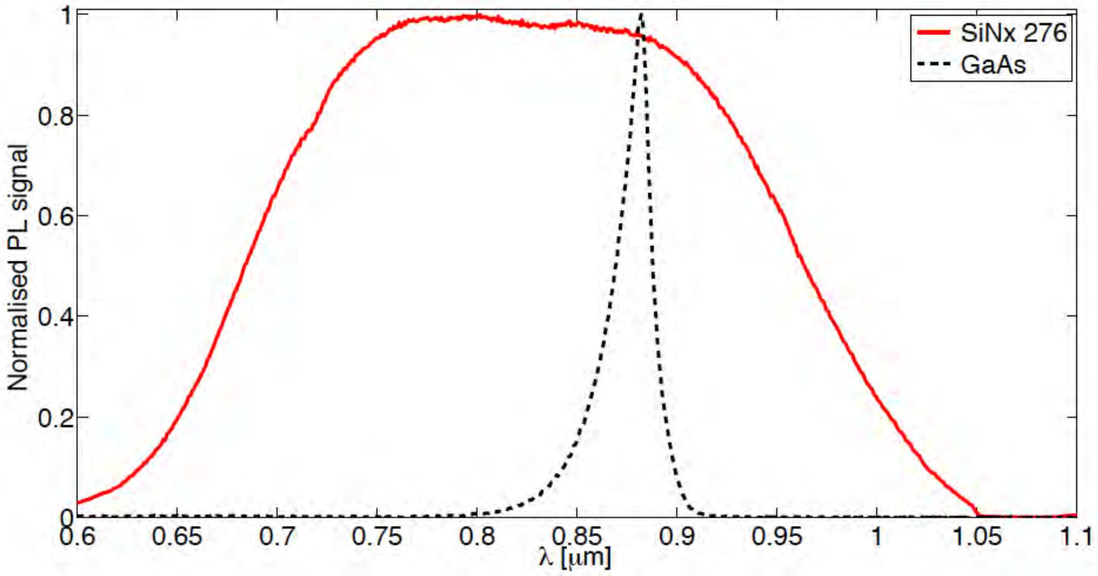

Figure 2.3: Normalised photoluminescence intensity measured in samples of SiN_x as a function of wavelength. Excitation is performed with a wavelength of 532nm with an average power of 10mW. [75]

Chapter 3

Experimental Methods & Theory

A number of techniques are available to measure the optical parameters of semiconductors, the following sections will describe two methods to resolve the refractive indices and, in the second case, thin film thickness' of opaque, multilayer semiconductor materials. The first method, known as reflectometry [77], is a simple yet effective method to resolve the reflection coefficients of samples. The second, ellipsometry [78, 79], is far more complex and allows, with appropriate caveats, the ability to resolve completely the complex optical parameters of the sample. Later sections will deal with using the measured optical parameters, resolved as a function of time, to infer information about the dynamics of carriers in these samples. This include discussions about time-resolved techniques, utilising a pump-probe schematic to optically excite and probe the material as well as introducing theoretical models used to develop an understanding of the physics involved with the interaction of light in these materials.

3.1 Reflectometry & Ellipsometry

The use of optics in the measurement of the physical properties of materials has been in use for several centuries. Since Sir Isaac Newton's observation of interference rings [80] optics have been used to measure the intrinsic properties of materials in a non-invasive manner. The observations of Newton would presently be classed under the term interferometry or *reflectometry*. Despite its early conception, reflectometry techniques were confined to academic laboratories and only began to show up in industrial applications in the 1960's [81]. The basic principle behind all modern reflectometry techniques is an extremely simple one. A beam of monochromatic light is incident upon a sample and a measurement of the light before and reflected light after the sample is taken. When measuring the intensity of the beam the technique provides the absolute reflectance of the sample.

In the following sections, techniques will be discussed that are capable of resolving important optical parameters of various opaque semiconductors. We will start by considering what salient information can be drawn from reflectometry measurements. To start, we take the assumption that the measurement is performed at normal incidence, this means that all the cosine terms of the Fresnel coefficients are equal to unity. Furthermore, due to the axial symmetry of the measurement at normal incidence, there is no way to discern between s- (perpendicular) and p- (parallel) polarised waves. The description used throughout this chapter for the polarisation state of light follows that of Clarke and Grainger [82].

Considering a plain surface (with no film), the Fresnel reflection coefficient is given by;

$$r_{13} = \frac{N_3 - N_1}{N_3 + N_1}. \tag{3.1}$$

Where N_3 is the complex index of refraction for the substrate and N_1 is the index of refraction of the surrounding medium/ambient (usually air, $N_1 = 1.0 - i0.0$). N.B. In this discussion the term N_2 has been reserved for the complex index of refraction of a thin film on top of the substrate. The absolute reflectance is related here by

$$R = |r_{13}|^2, \tag{3.2}$$

at this stage it is trivial to see how one can draw information about the refractive index directly from a measurement of the absolute reflectance of the sample. However it is not possible to separate the real and imaginary components (n_3, k_3).

In order to truly resolve both components of the refractive index, for all types of samples, and without assumption, a different approach should be taken. In this text the method used to obtain these parameters is that of ellipsometry. Ellipsometry measurements are performed using light of precisely known polarisation. The polarised light is reflected from or transmitted through a sample, and the resultant light is detected using an 'analyser' to ascertain the change in polarisation of the light due to its interaction with the sample. The nomenclature for 'ellipsometry' came from the fact that the polarised light often becomes elliptically polarised following reflection (or transmission). The technique measures two fundamental values (ψ, Δ). These are the amplitude ratio ψ and the phase difference Δ between the two orthogonal components (p- (parallel) and s- (perpendicular)) of the polarised light. Ellipsometry has become an attractive measurement tool due to its non-perturbative nature and high sensitivity to small interfacial effects, such as the composition of thin films. In order to achieve a truly non-perturbative technique the wavelength and intensity of the light must be properly chosen.

In this text we look at a technique known as spectroscopic ellipsometry. The range of wavelengths over which one scans can provide information on different atomic processes, depending on the range of photon energies and the structure of the material [78]. Ellipsometry has been widely applied to evaluate optical constants as well as thin film thicknesses in a plethora of solid state materials to great effect [83–86]. Recent advances allow for *in situ* measurements of these parameters, e.g. allowing the possibility to track the temporal evolution of thin-film growth [87]. However, for the purpose of this text only *ex situ* measurements (i.e. after the sample has been prepared) will be considered. The ability to extract knowledge of the optical constants is rather difficult directly from the absolute values (ψ, Δ) and so in normal practice an optical model is constructed for data analysis.

Unlike reflectometry measurements, ellipsometry allows one to directly measure both the refractive index n and extinction coefficient k. From these values (n, k) one can define the complex refractive index $N \equiv n - ik$. The sign here is based on whether one chooses to describe the extinction coefficient as a gain or loss, the convention used is based on the temporal evolution of the light wave defined by $e^{i\omega t}$ (rather than $e^{-i\omega t}$) as defined by Muller and other participants at the International Conference on Ellipsometry [88, 89]. From measurements of the complex refractive index one can draw the complex dielectric constant ε and absorption coefficient α. Which are found by the simple relations; $\varepsilon = N^2$ and $\alpha = 4\pi k/\lambda$.

3.1.1 Principles of Measurement & Terminology

In order to discuss how one would perform a spectroscopic ellipsometry measurement, it is useful to define precisely what parameters of the beam should be measured. In order to do so we define the fields of the EM wave using Maxwell's equations [90]. Let (E_{ip}, E_{is}), (E_{rp}, E_{rs}) and (E_{tp}, E_{ts}) represent the p- and s- components of the electric vectors of the incident, reflected and transmitted waves respectively. By matching the tangential components of **E** and **H** fields across an ambient/substrate interface the Fresnel complex-amplitude coefficients for reflection and transmission are retrieved.

$$r_p = \frac{N_3\cos\phi_1 - N_1\cos\phi_3}{N_3\cos\phi_1 + N_1\cos\phi_3} \qquad r_s = \frac{N_1\cos\phi_1 - N_3\cos\phi_3}{N_1\cos\phi_1 + N_3\cos\phi_3} \tag{3.3}$$

$$t_p = \frac{2N_1\cos\phi_1}{N_3\cos\phi_1 + N_1\cos\phi_3} \qquad t_s = \frac{2N_1\cos\phi_1}{N_1\cos\phi_1 + N_3\cos\phi_3} \tag{3.4}$$

Snell's law, $N_1\sin\phi_1 = N_3\sin\phi_3$, can then be used to recast the equations 3.3 in a form that is only dependent on the angle of incidence ϕ_1 and complex indices of refraction N_1 & N_3.

$$r_p = \frac{N_3\cos\phi_1 - N_1\sqrt{1-(\frac{N_1}{N_3}\sin\phi_1)^2}}{N_3\cos\phi_1 + N_1\sqrt{1-(\frac{N_1}{N_3}\sin\phi_1)^2}} \quad r_s = \frac{N_1\cos\phi_1 - N_3\sqrt{1-(\frac{N_1}{N_3}\sin\phi_1)^2}}{N_1\cos\phi_1 + N_3\sqrt{1-(\frac{N_1}{N_3}\sin\phi_1)^2}} \tag{3.5}$$

As with all reflectometry techniques the reflectance is defined as the ratio of the outgoing (reflected) wave intensity to that of the incoming (incident) wave. These are given by the square of the complex-amplitude Fresnel coefficients, such that;

$$R_p = |r_p|^2 \quad \text{and} \quad R_s = |r_s|^2. \tag{3.6}$$

The main ellipsometric values (ψ, Δ) can now be considered. In order to investigate the effect of reflection (or transmission) on the amplitude and phase of the wave separately it is useful to write the complex Fresnel coefficients as,

$$r_p = |r_p|\exp(i\delta_p), \qquad r_s = |r_s|\exp(i\delta_s). \tag{3.7}$$

Figure 3.1(a) represents a normal plane wave reflection from a surface and shows both p- and s-wave components. In general these components are not necessarily in phase. When each component is reflected from the surface there is a possibility of a phase shift and this phase shift may not be equal for both components. The phase difference for p- and s-wave components can be defined as δ_p and δ_s respectively. The value Δ (often referred to as Delta or 'Del') is then related to these parameters by:

$$\Delta = \delta_p - \delta_s. \tag{3.8}$$

Delta, therefore, is the phase difference induced by the surface between the p- and s-waves, and can take values between 0° and $+360^\circ$ (or -180° and $+180^\circ$, depending on preference) [79].

The reflection not only induces a phase change, but also an amplitude reduction for both p- and s-waves. As with the phase change the amplitude reduction will not necessarily be equal for p- and s-waves. The total reflection coefficients for p- and s-waves defined in Eq. 3.5 are in general complex, ψ is defined in relation to the magnitudes of these coefficients in the following manner;

$$\tan\psi = \frac{|r_p|}{|r_s|}, \tag{3.9}$$

ψ is therefore the angle whose tangent is the ratio of the magnitudes of the total reflection coefficients, and can take values ranging between 0° and 90° [79]. It is now useful

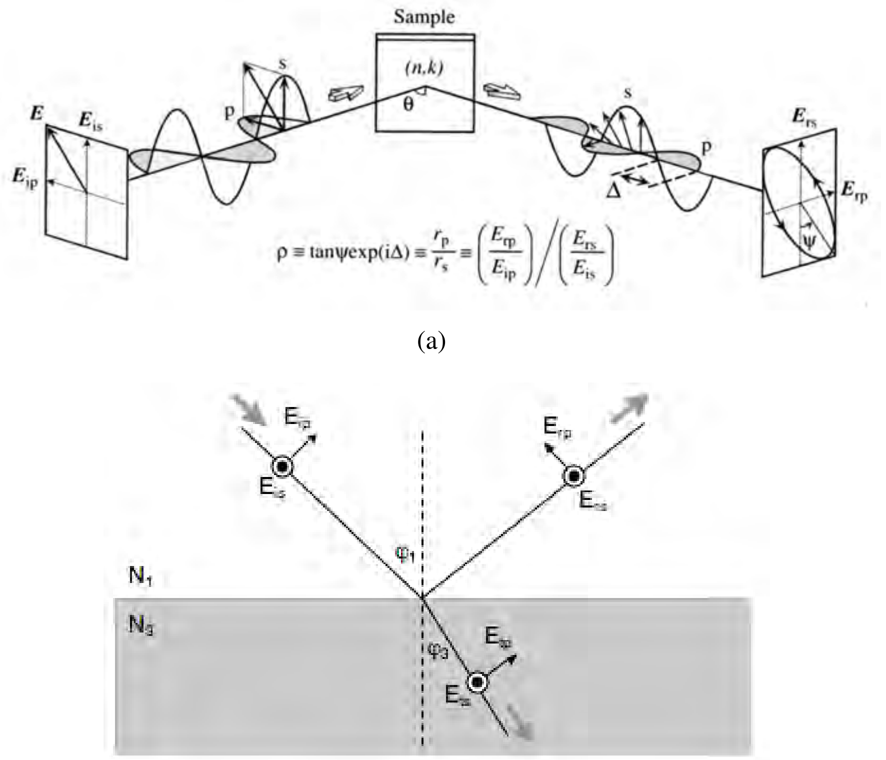

(a)

(b)

Figure 3.1: 3.1(a) Measurement principle of ellipsometry [78] 3.1(b) Electric field **E** for p- and s- polarisations, in this diagram E_s is perpendicular to the page. ϕ_1 and ϕ_2 are the angles of incidence and refraction respectively, and N$_1$ and N$_2$ are the complex refractive indices of the ambient and substrate.

to define ρ as the complex ratio of the total reflection coefficients, that is;

$$\rho = \frac{r_p}{r_s}. \tag{3.10}$$

The fundamental equation of ellipsometry defined by Azzam and Bashara [91] is then,

$$\rho = \tan\psi e^{i\Delta}. \tag{3.11}$$

The amplitude and phase components of ρ can be attributed to the tangential and exponential parts of this function respectively. It is important to note that when performing an ellipsometry measurement one should assume that the measured values of ψ and Δ are always correct (as long as the ellipsometer is functioning correctly). However, the quality of the optical constants that are extracted from this data rely heavily on the accuracy of the optical model.

3.1.2 Reflections from Ambient/Substrate Systems

To model an optical system accurately one must first appreciate what constitutes a thin film as apposed to a substrate. A material is defined as a substrate when knowledge of any materials beneath it or any lower boundary is *not* required. A material is considered a thin film when any light emerging from its top surface is a combination of reflections from both the top and bottom surfaces. It is convenient to start by considering a substrate with no film. A material is considered a substrate if it is sufficiently absorbing and thick enough that light incident onto its upper surface does not reach it's lower boundary (back side).

In SE a set of $\psi(\lambda)$ and $\Delta(\lambda)$ values are collected. In the case of a substrate (with no film), the optical constants can be retrieved directly with no need for any regression analysis. Following the same convention as previously (section 3.1), ψ and Δ can be inverted to give values of the optical constants $n(\lambda)$ and $k(\lambda)$. The complex relation is given by;

$$N_3 = N_1 \tan\phi_1 \sqrt{1 - \frac{4\rho \sin^2\phi_1}{(\rho+1)^2}}, \tag{3.12}$$

where ρ is the complex combination of Δ and ψ described by equation 3.11. N_1 and N_3 are the complex indices of refraction for the surrounding medium and the substrate respectively, and ϕ_1 is the angle of incidence of the incoming beam. These quantities are illustrated in figure 3.1(b).

Assuming that $k_1 = 0$, Eq. 3.12 is separable into two real functions;

$$\varepsilon' = n_3^2 - k_3^2 = n_1^2 \sin^2\phi_1 \left[1 + \frac{\tan^2\phi_1(\cos^2 2\psi - \sin^2\Delta \sin^2 2\psi)}{(1+\sin 2\psi \cos\Delta)^2}\right], \tag{3.13}$$

and

$$\varepsilon'' = 2n_3k_3 = \frac{n_1^2 \sin^2\phi_1 \tan^2\phi_1 \sin 4\psi \sin\Delta}{(1+\sin 2\psi \cos\Delta)^2}. \tag{3.14}$$

Where ε' and ε'' are the real and imaginary parts of the dielectric function $\varepsilon = \varepsilon' + i\varepsilon''$. Equations 3.13 & 3.14 can then be solved for n and k. The physically correct values of which will involve positive values of both n and k. The equations show that the complex index of refraction of medium 3 can be determined if the index of refraction of the incident medium (1) is known and the ellipsometric ratio ρ is measured for one angle of incidence ϕ_1.

Figures 3.2(a), 3.2(b) and 3.2(c), show the variation of the phase shifts (δ_p,δ_s), the reflectances (R_p, R_s) and the ellipsometric parameters (ψ, Δ) with incidence angle ϕ ($= \phi_1$) when light is incident upon the surface of a semiconductor (silicon). When p-polarised light is incident onto the interface between two transparent media (such as air/glass) the reflected wave at a certain angle is completely transmitted (in an ideal system), this angle of incidence is known as the *Brewster angle* ϕ_B. At this angle the incident wave is completely refracted into the second medium. For other interfaces such as air/semiconductor, the reflectance of the p-polarised light R_p does not reach zero, but still shows the characteristic minimum (whose value is dependent on the extinction coefficient k). This angle is known as the *pseudo-Brewster angle*.

Figure 3.2(a) shows that the reflectance R_p has a minimum at the pseudo-Brewster angle, while Fig. 3.2(b) shows that the phase shift of the p-polarised light δ_p experiences a transition from 2π for $\phi_1 < \phi_B$ to π for $\phi_1 > \phi_B$. If one considers the s-polarised components, the reflectance R_s shows a monotonic increase with incidence angle, while the phase shift δ_s remains constant at π. These measurements are the basis for the variation of the ellipsometric angles (ψ, Δ) shown in Fig. 3.2(c). One should note how Δ drops from a value of π below Brewster's angle to zero just after it, while ψ experiences a minimum at Brewster's angle. Another important angle to consider is known as the *principal angle* at which Δ reaches $\frac{1}{2}\pi$. The difference between the principal angle and the pseudo-Brewster angle is normally very small and tends to zero as the extinction coefficient k approaches zero. It is worth noting that the transition of Δ (from π to zero) becomes sharper as the value of the extinction coefficient becomes smaller. At the principal angle, incident light polarised at an azimuth to the plane of incidence, other

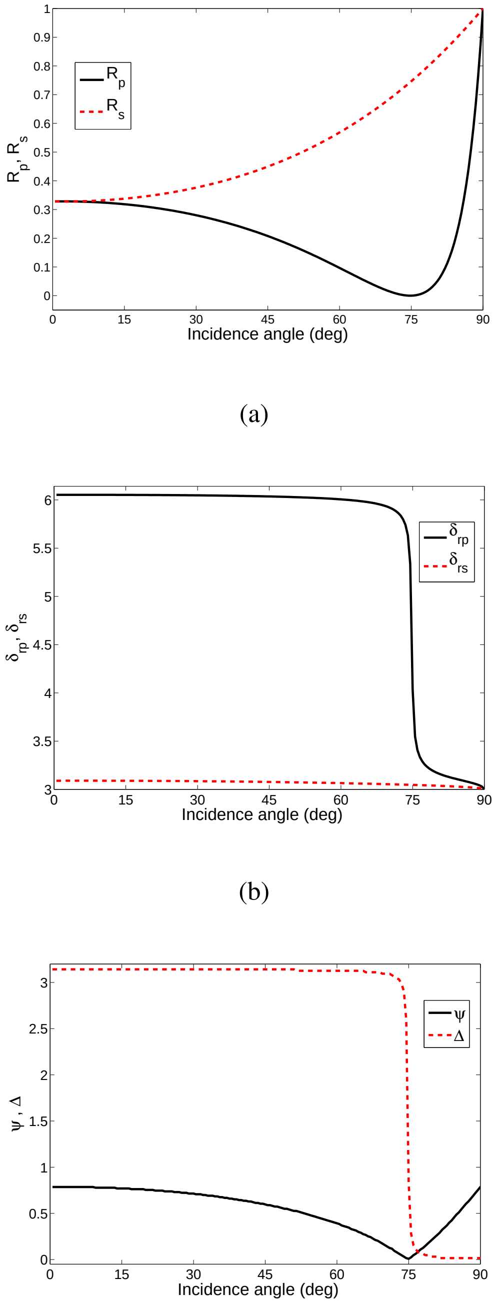

(a)

(b)

(c)

Figure 3.2: (a) The intensity reflectances R_p and R_s, (b) reflection phase shifts δ_{rp} and δ_{rs} and (c) ellipsometric angles ψ and Δ as functions of incidence angle ϕ for an air/silicon interface $N_{si} = 3.681 - i0.05$

than zero or $\frac{1}{2}\pi$, is reflected elliptically polarised. This follows because the s- and p-components, which are oscillating in phase prior to reflection acquire a phase difference Δ of $\frac{1}{2}\pi$ upon reflection.

3.1.3 Reflection from Ambient-Film-Substrate Systems

An extremely important part of ellipsometry is the case when the optical system to be analysed is that of a substrate with a single layer film. Figure 3.3 shows an example of such a system, the thickness of the film is labelled d and is sandwiched between two semi-infinite media (ambient and substrate). The film is considered to have parallel boundaries with respect to the ambient and substrate interfaces. The ambient, film and substrate are all homogeneous and optically isotropic, with complex indices of refraction N_1, N_2 and N_3 respectively.

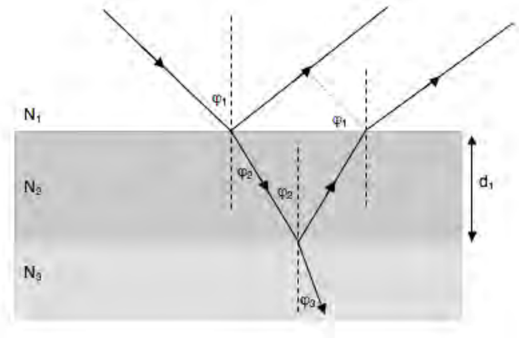

Figure 3.3: Optical interference in a thin film formed on a substrate. ϕ_1, and ϕ_2 are the angles of incidence and refraction in each of the 3 media respectively, N_1, N_2 and N_3 are the complex refractive indices of the ambient and substrate, and d_1 is the thin film thickness.

A plane wave that is incident upon the film (medium 2) at an angle ϕ_1 will have a reflected component in the ambient (medium 1) and transmitted wave at an angle ϕ_3 in the substrate (medium 3). The aim of this section is to relate the complex amplitudes of the reflected and transmitted waves to that of the incident wave for both p- and s-polarised incident beams. The procedure (originally performed by Drude [92]) is based on the physical picture in Fig. 3.3. In the following discussion the incident amplitude of the wave is assumed to be unity and polarised in either the p- or s- direction (the subscripts to denote this polarisation have been dropped for simplicity).

This picture is as follows; the incident wave is partially reflected from the (1, 2) boundary with an intensity according to the Fresnel reflection coefficients [equations 3.3-3.4]. The transmitted wave undergoes multiple internal reflections at the (2, 3) and

(2, 1) boundaries, these boundaries are in general not perfectly reflective and as such a small component is leaked out upon each reflection. It is useful to denote the Fresnel reflection and transmission coefficients for the boundaries (2, 1) and (2, 3) by r_{21}, t_{21} and r_{23}, t_{23} respectively. The resultant reflected wave in the ambient can be resolved from the complex amplitudes of the successive partial wave reflections r_{12}, $t_{12}t_{21}r_{23}e^{-i2\beta}$, $t_{12}t_{12}r_{21}r_{23}^{2}e^{-i4\beta}$, ... , and similarly for the transmitted wave in the substrate, which is made up of $t_{12}t_{23}e^{-i\beta}$, $t_{12}t_{21}r_{21}r_{23}e^{-i3\beta}$, ... , where β is the phase change experienced by the wave as it traverses the film from one boundary to the other (1, 2) to (2, 3). β can be defined as;

$$\beta = 2\pi\left(\frac{d_1}{\lambda}\right)N_2\cos\phi_2, \tag{3.15}$$

in terms of the free-space wavelength λ, thickness of the film d_1, the complex refractive index of the film N_2 and the angle of refraction (with respect to the normal) inside the film ϕ_2. Alternatively it can be defined in terms of the angle of incidence ϕ_1 by;

$$\beta = 2\pi\left(\frac{d_1}{\lambda}\right)\left(N_2^2 - N_1^2\sin^2\phi_1\right)^{1/2}. \tag{3.16}$$

Using the relations for the Fresnel reflection coefficients, $r_{10} = -r_{01}$ and $t_{01}t_{10} = 1 - r_{01}^2$ [93]. The addition of all the partial wave reflections results in an infinite geometric series who's summation provides the total reflected amplitude:

$$r = \frac{r_{12} + r_{23}e^{-2i\beta}}{1 + r_{12}r_{23}e^{-i2\beta}}. \tag{3.17}$$

Reinserting the polarisation dependence into equations 3.17, the following equations are retrieved.

$$r_p = \frac{r_{12p} + r_{23p}e^{-2i\beta}}{1 + r_{12p}r_{23p}e^{-i2\beta}}, \qquad r_s = \frac{r_{12s} + r_{23s}e^{-2i\beta}}{1 + r_{12s}r_{23s}e^{-i2\beta}}. \tag{3.18}$$

The Fresnel reflection coefficients at the boundaries (1, 2) and (2, 3) can be readily obtained from equations 3.3.

$$r_{12p} = \frac{N_2 \cos\phi_1 - N_1 \cos\phi_2}{N_2 \cos\phi_1 + N_1 \cos\phi_2}, \qquad r_{23p} = \frac{N_3 \cos\phi_2 - N_2 \cos\phi_3}{N_3 \cos\phi_2 + N_2 \cos\phi_3}, \tag{3.19}$$

$$r_{12s} = \frac{N_1 \cos\phi_1 - N_2 \cos\phi_2}{N_1 \cos\phi_1 + N_2 \cos\phi_2}, \qquad r_{23s} = \frac{N_2 \cos\phi_2 - N_3 \cos\phi_3}{N_2 \cos\phi_2 + N_3 \cos\phi_3}. \tag{3.20}$$

The three angles (ϕ_1, ϕ_2 and ϕ_3) contained in the equations (3.19, 3.20), which are the angles of propagation of the waves in the media 1, 2 and 3 respectively, can be related to each other via Snell's law as follows;

$$N_1 \sin\phi_1 = N_2 \sin\phi_2 = N_3 \sin\phi_3. \tag{3.21}$$

Applying the above theory to a practical system requires that certain conditions are met. Heavens [94] noted that there are three conditions for the theory to hold true; (*i*) the lateral dimension of the film should be many times that of its thickness to ensure one can use the approximation of an infinite number of reflections in the film, (*ii*) the bandwidth of the source, the degree of collimation, and the beam spot size as well as the film thickness should be such that the multiply-reflected waves combine coherently, and (*iii*) the film should not be amplifying. In general all of these conditions are met within a standard ellipsometry experiment, and more importantly in the experiments carried out here.

As the *interface* Fresnel coefficients for reflection (equations 3.18) are different for the ambient/film/substrate system compared to the *interface* coefficients for the ambient/substrate system, it is evident that the *overall* Fresnel coefficients must also be different. However, in a similar manner to the ambient/substrate case, the basis for ellipsometry on ambient/film/substrate systems is to measure the amplitude attenuation and phase change of the reflected and transmitted waves for both p- and s- components. Therefore one would use equations 3.10 and 3.11 in a manner akin to that of ambient/substrate ellipsometry calculations.

In most cases of reflection ellipsometry one can assume the case of a three-phase optically isotropic ambient/film/substrate system as described. The measured ellipsometric value $\rho = \frac{r_p}{r_s}$ can be modified by substitution of the complex amplitude reflection coefficients in equations 3.19-3.20;

$$\tan\psi e^{i\Delta} = \rho = \frac{r_{12p} + r_{23p}e^{-i2\beta}}{1 + r_{12p}r_{23p}e^{-i2\beta}} \times \frac{1 + r_{12s}r_{23s}e^{-i2\beta}}{r_{12s} + r_{23s}e^{-i2\beta}}, \tag{3.22}$$

where the ambient/film (r_{12p}, r_{12s}) and the film/substrate (r_{23p}, r_{23s}) interface Fresnel coefficients can be related to the optical properties of the system via equations 3.19, 3.20 and β. The phase change experienced by the light as it traverses the film, is related to the optical properties by equation 3.16. Therefore equation 3.22 relates the ellipsometric angles (ψ, Δ) to the refractive indices of the ambient N_1, the film N_2 and the substrate N_3, as well as the thickness of the film d_1, for given wavelengths of the ellipsometer λ and the angle of incidence ϕ_1. The dependence of ρ can then be written,

$$\tan\psi e^{i\Delta} = \rho(N_1, N_2, N_3, d_1, \lambda, \phi_1). \tag{3.23}$$

Equation 3.23 can subsequently be split into amplitude and phase components represented by the following real equations.

$$\psi = \tan^{-1}|\rho(N_1, N_2, N_3, d_1, \lambda, \phi_1)|, \tag{3.24}$$

$$\Delta = \arg[\rho(N_1, N_2, N_3, d_1, \lambda, \phi_1)], \tag{3.25}$$

where $|\rho|$ and $\arg(\rho)$ are the absolute value and argument (angle) of the complex function of ρ respectively. Although in this discussion it may seem that the solution to equation 3.22 is trivial, it is, in fact, for systems with more than 2 unknowns, rather complex. Indeed it can only be dealt with in a satisfactory manner with the use of a computer program. It is worth noting that ρ depends on no less than *nine* arguments: the real and imaginary components of all three complex refractive indices (N_1, N_2, N_3), the film thickness d_1, the beam wavelength λ, and the incidence angle ϕ_1.

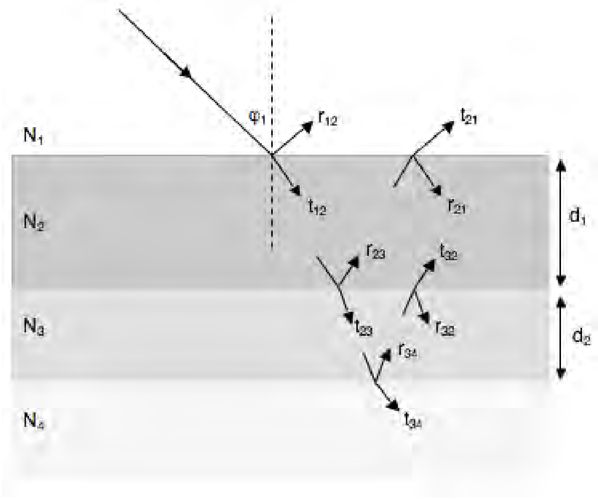

Figure 3.4: Fresnel coefficients and optical parameters for a three-layer structure. r$_{i,j}$ and t$_{i,j}$ are the complex Fresnel amplitude reflection and transmission coefficients for each of the media, N$_1$, N$_2$, N$_3$ and N$_4$ are the complex refractive indices of the 4 media, and d$_1$ and d_2 are the thin film thickness.

3.1.4 Multilayer Systems

The same procedure as described by section 3.1.3 can be extended to that of multilayer systems. Figure 3.4 shows a typical optical model for a 3-layer system. This is a system where two films are formed on a substrate. To solve this model, one first solves the problem set out in section 3.1.3 to find the Fresnel coefficients for a two layer system as described by Eq. 3.18. This is done for the substrate, and two film layers: 2, 3 & 4, as follows,

$$r_{234} = \frac{r_{23} + r_{34}\exp(-i2\beta_2)}{1 + r_{23}r_{34}\exp(-i2\beta_2)}. \tag{3.26}$$

The phase variation here, is given by $\beta_2 = \frac{2\pi d_2}{\lambda} N_3 \cos\phi_3$, which can be recast to include the incidence angle ϕ_1 and complex indices of refraction N_1 and N_3 using Snell's law 3.21. From equation 3.26 it is possible to obtain the amplitude coefficients for the 3-layer system;

$$r_{1234} = \frac{r_{12} + r_{234}\exp(-i2\beta_1)}{1 + r_{12}r_{234}\exp(-i2\beta_1)}. \tag{3.27}$$

Using this method it is possible to find an equation for the amplitude coefficients for a system of any number of layers. Putting equation 3.26 into 3.27 one retrieves the equation for a 3-layer system as;

$$r_{1234} = \frac{r_{12} + r_{23}\exp(-i2\beta_1) + [r_{12}r_{23} + \exp(-i2\beta_1)]r_{34}exp(-i2\beta_2)}{1 + r_{12}r_{23}\exp(-i2\beta_1) + [r_{23} + r_{12}\exp(-i2\beta_1)]r_{34}exp(-i2\beta_2)} \tag{3.28}$$

In a similar fashion to that of the previous section one can use the standard ellipsometric equation 3.11 along with Eq. 3.28 to resolve the ellipsometric angles (ψ, Δ). The next section contains further information on how exactly one should carry out an ellipsometry experiment including the advantages and pitfalls of two commonly used techniques. The first of these techniques is the simplest and most widely used, this involves rotating an analyser (polariser) positioned after the surface to measure the change in the polarisation due to the surface. The second method is more sophisticated, used to measure samples with small extinction coefficients, a rotating compensator (quarter-waveplate) is used in conjunction with a fixed analyser to resolve the change in polarisation for a given sample. This setup is discussed in the following sections.

3.1.5 Rotating Analyser Ellipsometry (RAE)

Ellipsometry experiments can be explained in terms of Jones (or Mueller, for poorly polarised systems) matrices. These matrices are a system for describing the polarisation state of light and the effect that optical components have on this polarisation state. Here we will implement a simple Jones matrix formulation [95] (table 3.1) to a standard PSA_R (Polariser-Sample-(rotating)Analyser) configuration. The Jones matrix formulation is useful for polarised light and is implemented with simple 2x2 matrices.

The rotating analyser ellipsometry setup is described as follows:

$$\mathbf{L}_{out} = \mathbf{AR}(A)\mathbf{SR}(-P)\mathbf{PL}_{in}, \tag{3.29}$$

where $\mathbf{L}_{out}$ is the light detected by a light detector and is given by $\mathbf{L}_{out} = [E_A, 0]^T$, the symbol T denotes the transposed matrix ($a_{ij} = a^T_{ji}$). In Eq. 3.29, $\mathbf{L}_{in}$ is the normalised Jones vector corresponding to incident light ($\mathbf{L}_{in} = [1,0]^T$), A of the rotation matrix $\mathbf{R}(A)$ represents the rotation angle of the analyser, and P is the rotation angle of the polariser. In order to express the transmission of light through a polariser, the electric

Table 3.1: Jones matrices for optical elements and co-ordinate rotation

Optical Element	**Symbol**	**Jones Matrix**
polariser (analyser)	**P** or **A**	$\begin{bmatrix} 1 & 0 \\ 0 & 0 \end{bmatrix}$
Compensator (Retarder)	**C**	$\begin{bmatrix} 1 & 0 \\ 0 & \exp(-i\delta) \end{bmatrix}$
Co-ordinate rotation	$\mathbf{R}(\alpha)$	$\begin{bmatrix} \cos\alpha & \sin\alpha \\ -\sin\alpha & \cos\alpha \end{bmatrix}$
Sample	**S**	$\begin{bmatrix} \sin\psi\exp(i\Delta) & 0 \\ 0 & \cos\psi \end{bmatrix}$

field (E_{ip}, E_{is}) co-ordinates of Fig. 3.1(a) must first be rotated such that the transmission axis of the polariser is parallel to that of the E_{ip} axis. After transmission of the light the co-ordinates are rotated back to their original position. In the Jones formulation this is expressed by $\mathbf{R}(-P)\mathbf{P}\mathbf{R}(P)$. If we consider that only light transmitted by the polariser is taken into account, the term $\mathbf{R}(P)$ is eliminated from $\mathbf{R}(-P)\mathbf{P}\mathbf{R}(P)$ and similarly for the analyser term we remove, $\mathbf{R}(-A)$, where the light transmitted through the analyser is detected independent of the co-ordinate rotation. Eq. 3.29 can be written in matrix form as

$$\begin{bmatrix} E_A \\ 0 \end{bmatrix} = \begin{bmatrix} 1 & 0 \\ 0 & 0 \end{bmatrix} \begin{bmatrix} \cos A & \sin A \\ -\sin A & \cos A \end{bmatrix} \begin{bmatrix} \sin\psi\exp(i\Delta) & 0 \\ 0 & \cos\psi \end{bmatrix} \times \begin{bmatrix} \cos P & -\sin P \\ \sin P & \cos P \end{bmatrix} \begin{bmatrix} 1 & 0 \\ 0 & 0 \end{bmatrix} \begin{bmatrix} 1 \\ 0 \end{bmatrix}. \tag{3.30}$$

For $P = +45^\circ$ the equation simplifies to,

$$\begin{bmatrix} E_A \\ 0 \end{bmatrix} = \begin{bmatrix} 1 & 0 \\ 0 & 0 \end{bmatrix} \begin{bmatrix} \cos A & \sin A \\ -\sin A & \cos A \end{bmatrix} \begin{bmatrix} \sin\psi\exp(i\Delta) \\ \cos\psi \end{bmatrix}. \tag{3.31}$$

Neglecting the $1/\sqrt{2}$ proportional term. Expansion of Eq. 3.31 provides the equation for the transmitted amplitude E_A.

$$E_A = \cos A \sin \psi \exp(i\Delta) + \sin A \cos \psi. \tag{3.32}$$

Therefore the light intensity measured at the detector is given by [82]

$$I = |E_A|^2 = I_0(1 + S_1 \cos 2A + S_2 \sin 2A), \tag{3.33}$$

where, I_0 represents the average intensity of one 'optical cycle', S_1 and S_2 are the Stoke's parameters given by,

$$S_1 = -\cos 2\psi \quad \& \quad S_2 = \sin 2\psi \cos \Delta. \tag{3.34}$$

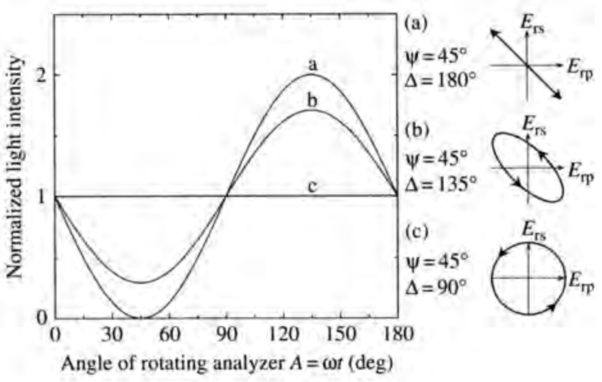

Figure 3.5: normalised light intensity in rotating-analyser ellipsometry (RAE), plotted as a function of the angle of rotating analyser $A = \omega t$. This figure summarizes the calculated results when the polarisation states of reflected light are (a) $\psi = 45°$, $\Delta = 180°$, (b) $\psi = 45°$, $\Delta = 135°$ and (c) $\psi = 45°$, $\Delta = 90°$. [78]

Fig. 3.5 shows the normalised light intensity detected according to Eq. 3.33. In order to find the values of the Stoke's parameters (S_1, S_2) the value of Δ was changed between 90° and 180° while ψ was kept constant. Figure 3.5 shows the intensity plot for three surfaces with constant ψ and different Δ values. As Δ is scanned between 90° and 180° the light emerging form the surface is transformed from circular, through elliptical, to linear polarisation. For samples with $k > 0$ one would expect an intensity plot similar to that in fig 3.5(b).

3.1.6 Rotating Analyser Ellipsometry with Compensator (RAEC)

In RAE the Stoke's parameter S_3 is not measured, this causes an error in measurement of Δ around $\Delta \cong 0°$ and $180°$. This is due to the ambiguity of the cosine of Δ in equation 3.34. Introduction of a compensator into the RAE setup allows one to overcome these problems [96]. Using Jones matrices RAE with compensator can be described as follows;

$$\mathbf{L}_{out} = \mathbf{AR}(A)\mathbf{CSR}(-P)\mathbf{PL}_{in}, \tag{3.35}$$

where the compensator is described by,

$$\mathbf{C} = \begin{bmatrix} \exp(-i\delta) & 0 \\ 0 & 1 \end{bmatrix} \tag{3.36}$$

In Eq. 3.35, **C** has simply been substituted into Eq. 3.29. The compensator here has been defined with its fast axis perpendicular to the plane of the surface (i.e. s-polarised). This is to simplify the equations (if the compensator was aligned parallel to the surface then one would use $\mathbf{R}(-C)\mathbf{CR}(C)$ instead of just **C**). The polarisation shift δ caused by the compensator is expressed as a function of C. If an incident polarisation $P = +45°$ is assumed then Eq. 3.35 becomes,

$$\begin{aligned} \begin{bmatrix} E_A \\ 0 \end{bmatrix} &= \begin{bmatrix} 1 & 0 \\ 0 & 0 \end{bmatrix} \begin{bmatrix} \cos A & \sin A \\ -\sin A & \cos A \end{bmatrix} \begin{bmatrix} \exp(-i\delta) & 0 \\ 0 & 1 \end{bmatrix} \begin{bmatrix} \sin\psi \exp(i\Delta) \\ \cos\psi \end{bmatrix} \\ &= \begin{bmatrix} 1 & 0 \\ 0 & 0 \end{bmatrix} \begin{bmatrix} \cos A & \sin A \\ -\sin A & \cos A \end{bmatrix} \begin{bmatrix} \sin\psi \exp[i(\Delta - \delta)] \\ \cos\psi \end{bmatrix} \end{aligned} \tag{3.37}$$

Here we see that the compensator introduces a shift on Δ but not on ψ. This tells us that the compensator does not affect the amplitudes of the s- and p-polarisation components but instead the relative phase between them. Therefore RAE with compensator can be described by simply replacing Δ by $\Delta' = \Delta - \delta$, the intensity detected is then given by

$$I = I_0[1 + S_1 \cos 2A + (S_2 \cos\delta - S_3 \sin\delta)\sin 2A]. \tag{3.38}$$

Where the third Stoke's parameter S_3 is defined as,

$$S_3 = -\sin(2\psi)\sin\Delta. \tag{3.39}$$

Evidently, this means that the measurement of all three Stoke's parameters S_{1-3} becomes possible. From Eq. 3.38 it is clear that the two components S_1 and $(S_2\cos\delta - S_3\sin\delta)$ are the measured Fourier coefficients in this measurement technique. To resolve S_2 and S_3 it is evident that two or more measurements with different values of δ should be taken [96]. The compensator (quarter waveplate) has the property that it produces a $\delta = 90^\circ$ phase shift for an incident polarisation $P = 45^\circ$ and a $\delta = 0^\circ$ shift for incident polarisation parallel to the fast or slow axis of the compensator. So for a constant incident polarisation of $P = 45^\circ$, there is a $\delta = 0^\circ$ phase shift when $C = 45^\circ (= P)$ and $\delta = 90^\circ$ phase shift when $C = 0^\circ$. Reference to Eq. 3.38 reveals that S_2 is obtained for $\delta = 0^\circ$ and S_3 when $\delta = 90^\circ$.

3.1.7 Rotating Compensator Ellipsometry (RCE)

The Jones matrix formulation for a rotating compensator ellipsometer in the PSC$_R$A (Polariser-Sample-(rotating)Compensator-Analyser) configuration is expressed as;

$$\mathbf{L}_{out} = \mathbf{A}\mathbf{R}(A)\mathbf{R}(-C)\mathbf{C}\mathbf{R}(C)\mathbf{S}\mathbf{R}(-P)\mathbf{P}\mathbf{L}_{in}. \tag{3.40}$$

This is found by simply inserting $\mathbf{R}(-C)\mathbf{C}\mathbf{R}(C)$ into Eq. 3.35. If it is assumed that the polariser and analyser angles are $P = 45^\circ$ and $A = 0^\circ$ respectively, and that the incident light is polarised such that $\mathbf{L}_{in} = [1,0]^T$ then the expansion of Eq. 3.40 is given by

$$\begin{aligned}\begin{bmatrix} E_A \\ 0 \end{bmatrix} &= \begin{bmatrix} 1 & 0 \\ 0 & 0 \end{bmatrix} \begin{bmatrix} \cos C & -\sin C \\ \sin C & \cos C \end{bmatrix} \begin{bmatrix} 1 & 0 \\ 0 & \exp(-i\delta) \end{bmatrix} \\ &\times \begin{bmatrix} \cos C & \sin C \\ -\sin C & \cos C \end{bmatrix} \begin{bmatrix} \sin\psi\exp[i(\Delta)] \\ \cos\psi \end{bmatrix}. \end{aligned} \tag{3.41}$$

Here we describe the compensator with its fast axis parallel to the surface (p-polarised) as opposed to section 3.1.6 where the compensator is aligned perpendicular to the surface (s-polarised). Substitution of $\delta = 90°$ into Eq. 3.41 yields the electric field amplitude,

$$E_A = (\cos^2 C - i\sin^2 C)\sin\psi\exp(i\Delta) + (1+i)\cos C\sin C\cos\psi). \tag{3.42}$$

The light intensity detected then follows (derivation in appendix D);

$$I = I_0(2 + S_1 - 2S_3\sin 2C + S_1\cos 4C + S_2\sin 4C). \tag{3.43}$$

It is clear from Eq. 3.43 that as the compensator is rotated, the Stoke's parameters S_{1-3} can be determined as the Fourier coefficients. The polarisations indicated in Fig. 3.6 are for light detected after the compensator. Figure 3.6(a) shows that for reflected linear polarisation [(ψ, Δ) = (45°, 180°)] the intensity varies with a period of 90° ($\cos 4C$). If we suppose that reflected light is polarised at $-45°$, as shown, the light transmitted through the compensator ($C = 0°$) will be right-circular polarised (E_R). Recall that the phase of the s-polarisation lags when $C = 0°$ (i.e. when the compensator fast axis is parallel to the plane of the surface (p-polarised)). This right-circular polarised light further transmitted through the analyser $A = 45°$, in this case we resolve the light into parallel and perpendicular components with respect to the surface and note that only the parallel component is transmitted through the analyser to be subsequently detected.

When the compensator then rotates to $C = 45°$, the slow axis coincides with the reflected linear polarisation ($E_{-45°}$), such that the light is transmitted with no phase change. This light is then perpendicular to the transmission axis of the analyser and as such the detected light intensity goes to a minimum. When the compensator is rotated further to $C = 90°$ the reflected light is transformed to left-circular polarised (E_L), and as a result the detected light intensity returns to a maximum. In a similar fashion to that of $C = 45°$, when the compensator is rotated to $C = 135°$ the detected intensity drops to a minimum again. So, in a PSC$_R$A configuration reflected linear polarised light oscillates with compensator angle with a period of 90°, in this respect it is straightforward to see that the Stoke's parameters S_1 and S_2 are measured as Fourier coefficients of $\cos 4C$

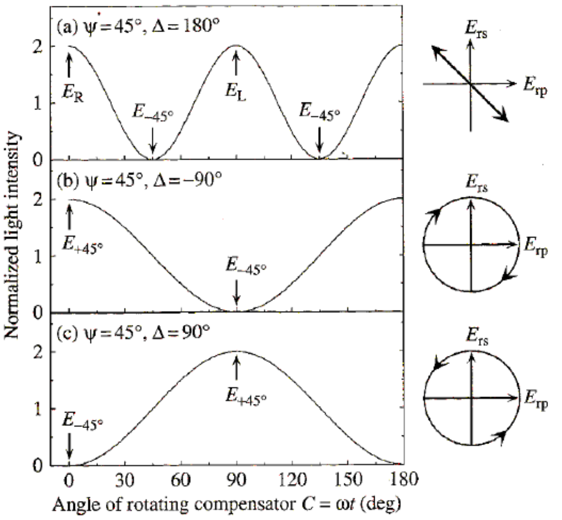

Figure 3.6: Normalised light intensity for rotating-compensator ellipsometry (RCE), plotted as a function of compensator angle C. The figure summarises the calculation results when the polarisation states of reflected light are (a) $\psi = 45°$, $\Delta = 180°$, (b) $\psi = 45°$, $\Delta = -90°$ and (c) $\psi = 45°$, $\Delta = 90°$. The polarisation (denoted by an arrow) represent the polarisation states of reflected light emerging from the rotating compensator [78].

and $\sin 4C$.

Figure 3.6(b), shows the recorded intensity for light reflected with right-circular polarisation. Here, we see a 180° period ($\cos 2C$, see Eq. 3.43). If the Stoke's vector $[S_0, S_1, S_2, S_3]^T$ of reflected light is then represented by $\mathbf{L}_R = [1, 0, 0, 1]^T$ (right-circular polarised), the polarisation state emerging from the compensator is given by

$$\mathbf{L}_{out} = \mathbf{R}(-C)\mathbf{C}\mathbf{R}(C)\mathbf{L}_R. \tag{3.44}$$

Mueller matrices (an extension of the Jones matrix formulation) developed by Hans Mueller [91], simplifies this description. Using Mueller matrices the polarisation state of the light Eq. 3.44 is given by [78]

$$\mathbf{L}_C = [1, -\sin 2C, \cos 2C, 0]^T \tag{3.45}$$

This shows that right-circular polarised light incident onto the compensator ($\delta = 90°$) is transformed to linear polarisation described by $-\sin 2C$ (S_1) and $\cos 2C$ (S_2). The direction of the linear polarisation then changes with the angle of the compensator (i.e. analogous to the RAE system). This can be seen from Eq. 3.45 when $C = 0^\circ$ is substituted and $\mathbf{L}_C = [1,0,1,0]^T$ is obtained, which represents E_{+45°. The light intensity detected is therefore maximised for $C = 0^\circ$. If the compensator is then rotated to $C = 90^\circ$ then the polarisation is rotated to E_{-45° and therefore light intensity is minimised.

For left-circular polarised reflected light, the light from the compensator is found by substitution of $\mathbf{L}_R = [1,0,0,-1]^T$ into Eq. 3.44,

$$\mathbf{L}_C = [1, \sin 2C, -\cos 2C, 0]^T. \tag{3.46}$$

As with right-circular polarised light, here the light transmitted by the compensator at an angle $C = 0^\circ$, the light becomes linearly polarised. From Fig. 3.6 it is seen that the variation of light intensity with C is opposite to that of the right-circular polarised case. This means that the signs of the Stoke's parameters have been reversed. Therefore linear polarised light is detected as the component of light oscillating at four times the compensator frequency (4ω), circularly polarised light is detected at twice the compensator frequency (2ω) and elliptically polarised light is detected as a superposition of these 2ω and 4ω components.

3.2 Time-Resolved Techniques

Perhaps the most common use for ultrafast technologies is to study time-resolved processes in solid-state, chemical and biological materials. Ultrafast pulses provide an excellent basis for taking 'stop-action' snapshots of processes in a manner akin to taking photographs of high-speed processes using a flash lamp [1]. In the following sections studies of photo-excited carriers in solid-state materials will be considered. Examples of a vast array of studies in semiconductor materials can be found here [97]. These include reflection, luminescence, absorption and scattering spectroscopy, which reveal processes of the electronic band structure, phonons, excitons, defect states, surface interactions etc. Not only this but due to the extreme nature of the light being used one can gain access to the temporal evolution of nonlinear, non-equilibirum and transport properties of semiconductors [97].

As a multitude of techniques are available within the pump-probe remit, the general scheme of a typical pump-probe measurement is discussed. Fig. 3.7 depicts a standard pump-probe measurement, in which an intense pump pulse excites a medium into some non-equilibrium state. A shortly following probe pulse of smaller intensity, such that the system is not excited further, then probes the material to detect any change in the samples optical properties. We may write that the pump pulse excites some change in the optical property of the sample O such that,

$$O(t) \rightarrow O_0 + \Delta O(\tau - \tau_0) \tag{3.47}$$

where O_0 is the unperturbed sample's optical property O and $O(\tau - \tau_0)$ is that property some time τ following excitation at τ_0. The delay between the measurement time τ and the excitation time τ_0 represents the delay between the probe and pump pulses $\Delta\tau$. If one is free to vary the measurement time τ via some method of delaying the probe pulse, the transient change in the optical property can be mapped as a function of time. This scheme provides a correlation function, similar to those measured by common pulse length measurements, such as autocorrelation [18].

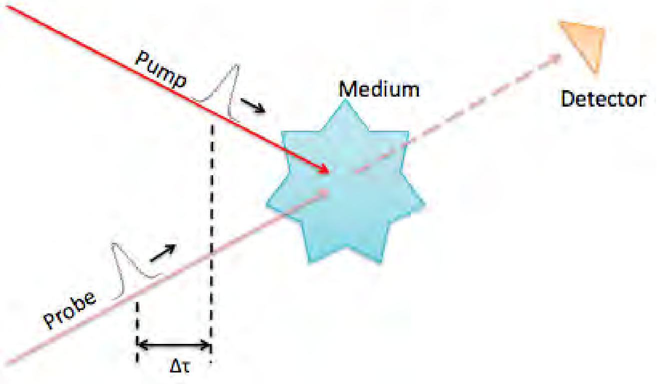

Figure 3.7: Schematic of a standard non-collinear pump-probe experiment. A short intense pulse of light is incident upon a sample at time $\tau = 0$ in order to 'pump' the sample into some non-equilibrium state. A less intense pulse is incident some time following excitation $\tau > 0$, to 'probe' a change in an optical parameter such as transmission (shown), reflection or absorption. A photodetector is used following the sample to measure the transient change in the desired optical parameter.

Measurement of the optical properties of semiconductors can lead to interesting information about their intrinsic processes. Spectroscopy provides a unique tool to study the distributions of excitations (electrons, holes, excitons, phonons, plasmons, etc.) and their subsequent relaxation paths. Combining these methods with spatially resolved techniques [50, 98], one can gain knowledge of the transport properties of these dynamic excitation in any number of bulk and nano structured semiconductors. Due to the complexity of these processes it can be crucial to choose the right probing method, for instance transmission measurements of the sample provide an excellent tool to study absorption, whereas reflectivity measurements tend to be sensitive to refractive index changes as well as absorption [1]. However, it is not just reflectivity measurements that provide information about the refractive index, interferometric measurements as well as spectroscopic techniques in which the phase can be measured lend themselves to exploring the complex refractive index of samples $N \equiv n - ik$.

3.2.1 TR-Reflectometry

In order to map how the refractive index N of an opaque semiconductor evolves on the femtosecond time scale one can modify a typical reflectometry setup (sec 3.1) by combining it with a pump-probe approach (sec 3.2). The choice of pump and probe photon energies, mode of detection and geometry of the system must all be carefully chosen. The detector used operates, in general, on a slow time scale with respect to the length of the pulse and the dynamics being studied, averaging in this time-integrated manner means that the resolution of the system is down to the method of pump-probe delay. For instance, in the measurements shown here, the resolution of the system is given by the incremental steps of a 1-D translation stage. Furthermore, when considering what dynamics are to be studied the photon energies of the probe should be carefully considered, the case in which the pump and probe are of the same wavelength is known as degenerate, whereas for pump and probe beams separated in energy the system is non-degenerate. A schematic for the degenerate case, used in these works, is shown in Fig. 3.8.

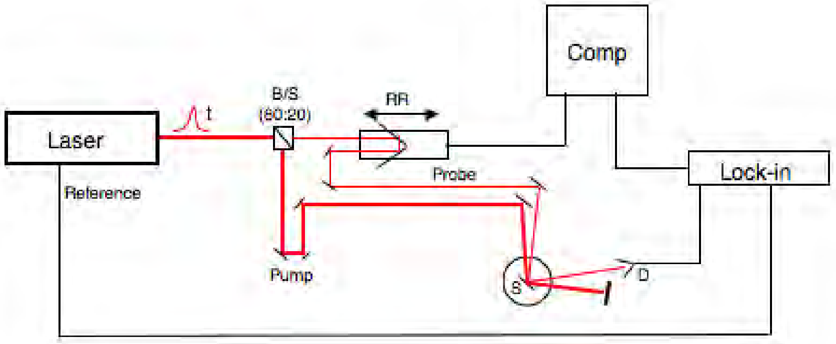

Figure 3.8: Schematic diagram of a typical time-resolved pump-probe reflectometry setup. Where *t* is the duration of the ultrashort pulse, B/S is a partial beamsplitter, RR is a retro-reflector mounted on an automated micrometer translation stage, S is the sample being analysed mounted on a rotation stage with (x, y, z) μm controls, D is a silicon photodiode connected to a lock-in amplifier and Comp is a computer with LabView software for control of the translation stage.

In all subsequent studies the same basic setup is used, here, the output of an amplified Ti:sapphire ultrafast oscillator, producing ultrafast pulses with pulse duration, repetition rate, average pulse energy and bandwidth of $\sim$ 45fs , 1kHz, $\sim$ 4W and $\sim$ 60nm respectively, are attenuated and then split by a $R80:T20$ beamsplitter. The reflected component (the probe) is passed through a motorised 1-D translation stage with sub-μm control, while the transmitted component (the pump) traverses a fixed optical path. This provides the pulse delay between pump and probe components. The beams are combined onto the sample with a non-collinear geometry. Furthermore, the beams are polarised at azimuths orthogonal to one another and the pump beam blocked following the sample to avoid interference. The probe is then detected with a standard silicon photodiode and processed with a lock-in amplifier to maximise the signal-to-noise-ratio (SNR).

If a standard silicon photodiode detector is replaced with a spectrometer and the probing beam is of sufficient bandwidth a spectroscopic reflectometry measurement may be performed. Measurement of the reflectance of the sample as a function of time and wavelength can lead to interesting observations about the sample properties including the electronic band structure, plasma frequency, absorption and scattering dynamics [41].

3.2.2 TR-Ellipsometry

The procedures and calibration in this section are based on the paper: **Time-resolved Ellipsometry to Study Extreme Non-equilibrium Electron Dynamics in Nanostructured Semiconductors, MRS Proceedings Spring 2012, DOI: 10.1557/opl.2012.1262 (2012)** [99]

As apposed to the inherent ambiguities of time-resolved reflectometry measurements, in which only the amplitude change of reflectance is measured as a function of the probe delay, time-resolved ellipsometry measurements allows for complete determination of the complex refractive index with time ($N(t) = n(t) - ik(t)$). Ellipsometry measurements, as described in sec 3.1, measure both the amplitude and phase of the beam. The ellipsometry method used here is that of rotating compensator ellipsometry in the PSC$_R$A (polariser - sample - (rotating) compensator - analyser) configuration.

The ellipsometry system that is described hereafter was built in the probe arm of the reflectometry setup, discussed in section 3.2.1. The home built ellipsometer uses an Edmund Optics linear high-contrast (10,000:1) glass broadband (750-1400nm) polariser to set the initial polarisation state of the beam. The focused beam is combined with the pump beam non-collinearly at the sample surface (as in the reflectometry setup) and the resultant reflected beam is passed through a combination of compensator and analyser before being detected. The compensator used was a Newport Optics broadband (700-1000nm) achromatic quarter ($\lambda/4$) wave plate, providing little dispersion over the range of wavelengths used. The compensator was mounted in a New Focus motorised 'ground-worm gear' rotation mount providing accurate rotation of the optic to 0.01°. The analyser was a Thorlabs Glan-Thompson polariser with an extinction ratio of 100,000:1 and was set up prior to the detector in order to measure the polarisation change as described previously. The beam is detected using a standard large aperture Thorlabs silicon photodetector and processed using a Stanford Research lock-in amplifier detecting the signal at the laser repetition rate.

This method provides certain advantages over other techniques that make it an ideal choice when working with multilayer low absorption semiconductors. Due to the technique's sensitivity to changes in the phase parameter Δ and sensitivity to this parameter near 0° and 180°. Low absorption samples, whose phase changes quickly at incidence angles near the Brewster angle, can therefore be measured accurately. The method is also inherently sensitive to thin film thicknesses of multilayer samples due to measurement of the amplitude and phase of the beam [78].

The Jones formulation [95] was used in section 3.1 to mathematically describe the detected intensity of the measurement. It has been noted from equation 3.43 that the Stoke's vectors can be described by the second and fourth order Fourier components oscillating at 2× and 4× the compensator frequency ω_C. Equation 3.43 may therefore be recast as,

$$I(C) = A_0 + A_2 \cos 2C + B_2 \sin 2C + A_4 \cos 4C + B_4 \sin 4C. \tag{3.48}$$

Where C is the angle of the compensator and the Fourier coefficients, A_i and B_i, where i is the order of oscillation frequency, are given by;

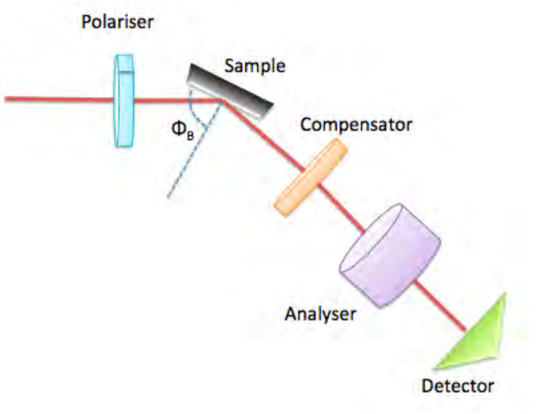

Figure 3.9: Generalized scheme for a rotating compensator ellipsometry (RCE) measurement. The incident light is polarised prior to the sample at an angle of P. The light is then incident onto a sample at an incidence angle Φ, at which point it undergoes reflection (shown), transmission and/or absorption processes. The reflected (in this case) light transmits a compensator (usually a quarter wave plate, $\lambda/4$) and an analyser prior to being detected with a photodetector or spectrometer. Rotation of the compensator through 360° provides an intensity profile as per Eq. 3.43, yielding the Stoke's vectors S_i of the sample.

$$\begin{aligned}
A_0 &= \frac{1}{\pi}\int_0^\infty I(C)dC \\
A_2 &= \frac{2}{\pi}\int_0^\infty I(C)\cos 2CdC \\
B_2 &= \frac{2}{\pi}\int_0^\infty I(C)\sin 2CdC \\
A_4 &= \frac{2}{\pi}\int_0^\infty I(C)\cos 4CdC \\
B_4 &= \frac{2}{\pi}\int_0^\infty I(C)\sin 4CdC
\end{aligned} \tag{3.49}$$

These coefficients can then be formulated in terms of the ellipsometric parameters [100], giving,

$$\begin{aligned} A_0 =& 1 - \cos 2P \cos 2\Psi \\ &+ \frac{1}{2}[\cos 2A(\cos 2P - \cos 2\Psi) + \sin 2A \sin 2P \sin 2\Psi \cos\Delta], \quad (3.50) \\ A_2 =& -\sin 2A \sin 2P \sin 2\Psi \sin\Delta, \quad (3.51) \\ B_2 =& \cos 2A \sin 2P \sin 2\Psi \sin\Delta, \quad (3.52) \\ A_4 =& \frac{1}{2}[\cos 2A(\cos 2P - \cos 2\Psi) - \sin 2A \sin 2P \sin 2\Psi \cos\Delta], \quad (3.53) \\ B_4 =& \frac{1}{2}[\cos 2A \sin 2P \sin 2\Psi \cos\Delta + \sin 2A(\cos 2P - \cos 2\Psi)]. \quad (3.54) \end{aligned}$$

For the case where the polariser angle $P = 45^\circ$ and the analyser angle $A = 0^\circ$ equations 3.50-3.54 can be simplified,

$$\begin{aligned} A_0 &= 1 - \frac{1}{2}\cos 2\Psi, \quad (3.55) \\ A_2 &= 0, \quad (3.56) \\ B_2 &= \sin 2\Psi, \quad (3.57) \\ A_4 &= \frac{1}{2}\cos 2\Psi, \quad (3.58) \\ B_4 &= \frac{1}{2}\sin 2\Psi \cos\Delta. \quad (3.59) \end{aligned}$$

It should be noted that these equations are only valid for a perfect compensator. Furthermore the Fourier coefficient A_0, the zeroth order component, should not be used as it may contain interference from other sources. We also omit the Fourier component A_2 which provides a zero for this set of experimental parameters. The ratios of the Fourier coefficients should only be used as the absolute intensity is not measured in standard ellipsometry measurements. Hence the Fourier coefficients B_2 and B_4 will be scaled with respect to A_4 to provide,

$$\frac{B_2}{A_4} = -2\tan 2\Psi \sin\Delta \tag{3.60}$$

$$\frac{B_4}{A_4} = -\tan 2\Psi \cos\Delta \tag{3.61}$$

If we now define two parameters $X_1 \equiv -\frac{B_2}{2A_4}$ and $X_2 \equiv -\frac{B_4}{A_4}$, then the ellipsometric angles can be straightforwardly defined in terms of these parameters as,

$$\tan 2\Psi = \sqrt{X_1^2 + X_2^2} \tag{3.62}$$

$$\tan\Delta = X_1/X_2 \tag{3.63}$$

Due to the nature of these tangent equations the values of Ψ and Δ must be rescaled using the signs of the Fourier coefficients. A procedure for correcting the ellipsometric parameters was proposed by Boer *et. al.* [100] and is presented in table 3.2. Due to both parameters having tangent dependence, there are no regions in the Ψ-Δ plane in which the ellipsometer loses accuracy.

Table 3.2: In order to determine the correct values of Ψ and Δ the signs of the Fourier coefficients A_4 and B_4 should be known. The value of Ψ and Δ measured should be corrected as shown in the table in which, the indices designate in which order the steps should be performed. These transformations are based on Eq. 3.63 [100].

$A_4 > 0 \rightarrow \Psi_2 = 90^\circ - \Psi_1$	
$A_4 < 0 \rightarrow \Psi_2 = \Psi_1$	
$B_4 > 0 \rightarrow \Delta_2 = \Delta_1$	$\Delta_2 < 0 \rightarrow \Delta_3 = \Delta_2 + 360^\circ$
$B_4 < 0 \rightarrow \Delta_2 = \Delta_1 + 180^\circ$	$\Delta_2 > 0 \rightarrow \Delta_3 = \Delta_2$

For the ellipsometer to work effectively it is clear that positions of P, C and A should be well defined and accurately calibrated for proper fitting of the intensity profile to be performed. Initially it is worth considering the calibration of the polariser angle, P, and analyser, A. The technique commonly used to align these optics was developed by McCrackin *et. al.* [101] and then later adapted by Ghezzo [102]. Initially the compensator is removed and a highly reflective surface is used in place of the sample (it is important that the sample adds no ellipticity to the beam). McCrackin [101] noted that in this case the intensity transmitted by the analyser was proportional to,

$$I = 4L^2 + \frac{4\chi^2}{\tan^2\Psi\sin^2\delta} - \frac{8L\chi}{\tan\Psi}\left(\frac{\cos\Delta}{\tan\delta} - \sin\Delta\right), \tag{3.64}$$

where $L = A - \pi/2$, δ is the phase difference between p- and s- components of polarised light transmitted by the polariser and χ is related to the polariser angle by

$$\chi = P\tan\delta. \tag{3.65}$$

Eq. 3.64 is only valid when the polariser and analyser angles are set almost parallel and perpendicular to the plane of incidence, respectively. Using equations 3.64 & 3.65 we find and expression for the intensity in terms of P:

$$I = 4L^2 + \frac{4}{\tan^2\Psi}(\chi^2 + P^2) - \frac{8L}{\tan\Psi}(P\cos\Delta - \chi\sin\Delta). \tag{3.66}$$

With the analyser set perpendicular to the plane of incidence, a minimum of light transmission is found for polariser angles which satisfy $\partial I/\partial P = 0$, along with equation 3.66 and the definition of L, the angle of P providing minimum transmitted light intensity is given by,

$$P = (A - \pi/2)\tan\Psi\cos\Delta. \tag{3.67}$$

With equation 3.67 at hand, it can be seen that by incrementing the position of A and finding the minimum light intensity using P a set of points (A,P) are found. This procedure is repeated for a different incidence angle and another curve is found which follows,

$$P = (A - \pi/2)\tan\bar{\Psi}\cos\bar{\Delta}, \tag{3.68}$$

where $\bar{\Delta}$ and $\bar{\Psi}$ are the new set of azimuths for this incidence angle. Now, by eliminating A from equations 3.67 & 3.68, we find,

$$P(1 - \frac{\tan\Psi\cos\Delta}{\tan\bar{\Psi}\cos\bar{\Delta}}) = 0. \tag{3.69}$$

If the incidence angles are chosen carefully such that each lies on either side of Brewster's angle for the reflective surface, Heavens [94] shows that,

$$\frac{\tan\Psi\cos\Delta}{\tan\bar{\Psi}\cos\bar{\Delta}} < 0, \tag{3.70}$$

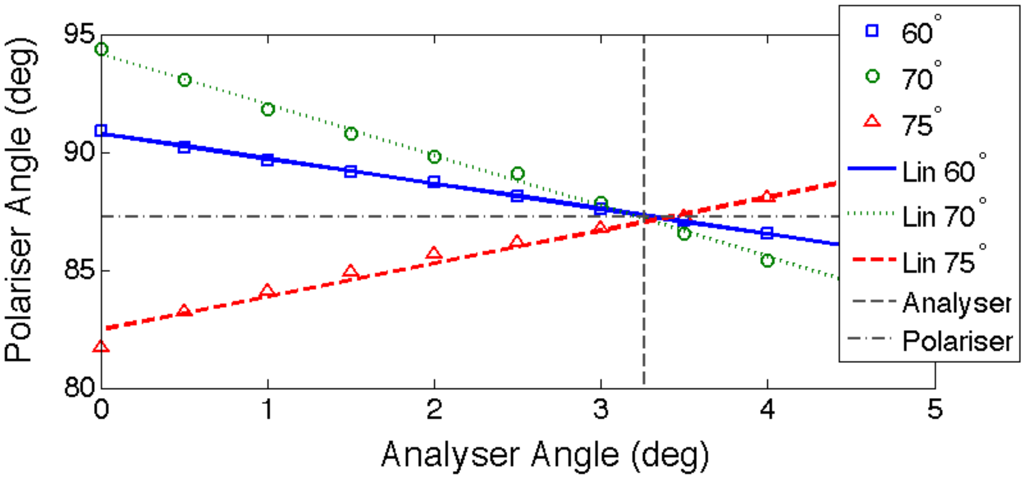

Figure 3.10: Calibration of the azimuths of polariser and analyser for use in ellipsometry measurements. The values of polariser angle P and analyser angle A, according to the housing of the optics, are plotted as per Eq. 3.67. The crossing points of these vectors provides the precise alignment of polariser and analyser such that they are exacty orthogonal with azimuths equal to $P = 90°$ and $A = 0°$.

such that equation 3.69 can only be satisfied for $P = 0°$, leading via equation 3.68 to a corresponding analyser angle of $A = \pi/2 = 90°$. Using the intersection of the two curves described by 3.67 & 3.68 the polariser and analyser can be calibrated extremely accurately. Fig. 3.10 shows the alignment procedure described here for three separate incidence angles providing a calibration such that the true position of the polariser and analyser can be aligned with the scale readings on the housing of these optics.

With the polariser and analyser calibrated it is then possible to accurately rotate the polariser and analyser to $P = 45°$ and $A = 0°$ respectively. With this arrangement the sample is then removed and the arms of the ellipsometer brought in-line such that the incidence angle is equal to $\phi_i = 0°$. Rotating the compensator through 0°-360° it is then possible to model the intensity detected following the analyser given a perfectly aligned compensator via Jones matrix formulation (using the same method as in appendix D) as follows,

$$I_{det} = \frac{1}{2} + \frac{1}{2}\cos(2C)\sin(2C). \tag{3.71}$$

Plotting experimental data against this theoretical model (shown in Fig. 3.11) it is possible to see the shift required to align the compensator precisely. In the procedure used for analysis in this text the shift in compensator required is given by the difference between the second minima of the experimental and theoretical curves (this choice is arbitrary). The slight variation of the measured intensity as a function of compensator angle with respect to the theoretical curve is due to the non-perfect nature of the compensator (such as inhomogeneities of the optic across the beam profile).

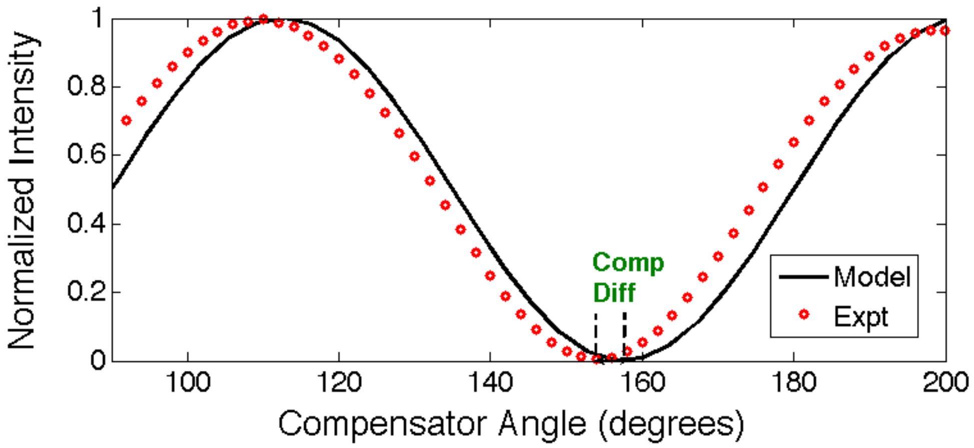

Figure 3.11: Calibration of compensator ($\lambda/4$). The intensity of light is measured in a PCA configuration (no sample). Comparing theoretically predicted intensity (black line) with experimentally measured data (red symbols) allows for the mis-match in alignment angle of the compensator C to be found and adjusted for.

Given that the ellipsometer is fully calibrated as described above, one can then perform a standard fitting procedure. Fitting equation 3.48 to the detected intensity as a function of the probe wavelength (λ) and probe delay (τ), is the fundamental procedure for all time-resolved spectroscopic ellipsometry measurements. Fig. 3.12 shows a typical intensity curve as a function of compensator angle, fitted for a single probing wavelength at a fixed delay time. In a time-resolved spectroscopic ellipsometry measurement a set of wavelength and time increments would be processed simultaneously to map the change of the ellipsometric parameters $\Psi(\lambda,\tau)$ and $\Delta(\lambda,\tau)$.

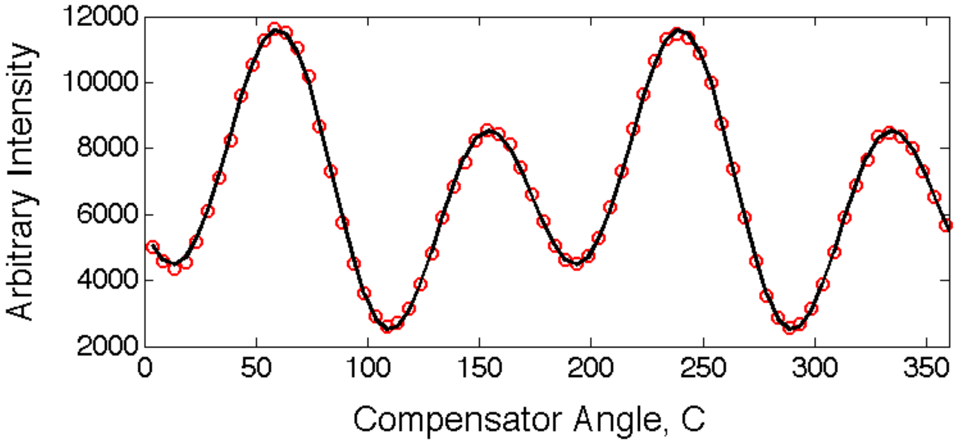

Figure 3.12: The intensity of light for a rotating compensator ellipsometry (RCE) measurement at a wavelength $\lambda = 760$nm. The data (red symbols) are fitted using Eq. 3.48 (black line) to yield the ellipsometric parameters Ψ and Δ. This procedure is performed in a TR-RCE measurement for all probing wavelengths and probe delay times τ separately.

Once this set of data has been measured an optical model should be built and the appropriate treatment using Fresnel formulae should then be performed as per section 3.1.

3.2.3 Multiple Angle and Pump Fluence Reflectometry

Performing spectroscopic reflectometry at multiple incidence angles or multiple fluences provides a convenient way to measure unambiguously certain sample parameters, such as the optical mass of carriers, absorption, plasma frequency and scattering time. In order to do this a standard spectroscopic reflectometry measurement should be performed as described in section 3.2.1. The measurement can then be repeated for multiple incidence angles to provide a set of data to which a model of carrier absorption (such as the Drude model) can be applied. Via application of the same model to all multi-angle reflectometry measurements, ambiguity in the fitting parameters can be avoided. Similarly, for measurements at different pump fluences fitting can be made to multiple measurements to analyse different optical parameters.

In order to fit a time-dependent carrier absorption model to a multiple layer system, such as those often measured with ellipsometry measurements, an optical model should first be made. In order for reflectometry measurements to be applicable one must know all of the optical constants and film thickness' before the model can be applied. The best method to resolve these parameters is to perform a static ellipsometry measurement first. Once the optical model has been evaluated, the model of carrier absorption can be applied to the dielectric function dispersions of the appropriate layer(s). This procedure should be applied to fit the change in reflectance measured as a function of the probe delay and probing wavelengths (see reference [103]).

3.2.4 Time-Resolved Scattering Measurements

The intense research into the time domain evolution of carrier dynamics in semiconductor materials has been driven by improvements to electro-optical devices whose speed, efficiency and optical non-linear behaviour they determine. Pump-probe spectroscopy has been the standard tool of investigation into these processes, however in nano-structured samples these techniques suffer from spatial averaging of the signal, blurring the contributions of the composite phases of the material. Despite the interest into composite materials, due to their multitude of uses in photo-voltaics, all-optical switching etc., little is known about their optical excitation and decay channels [34]. Due to the inherent complexity of composite materials, theoretical models have struggled to predict their dynamics [104–108], leaving only a few experimental measurements to provide an insight into these processes [109–112].

In order to resolve the contribution of both phases in a typical nano-structured semiconductor, such as nano-crystalline silicon (*nc-Si:H*), a combination of pump-probe reflectometry and scattering can be performed (shown schematically in Fig. 3.13). Here, the former provides knowledge of the spatially averaged contribution of the phases, while the latter describes their differences [113]. A model can then be provided to describe the dependence of the dielectric function upon excitation. In a manner similar to that of the multi-angle reflectometry described in section 3.2.3, an optical model should

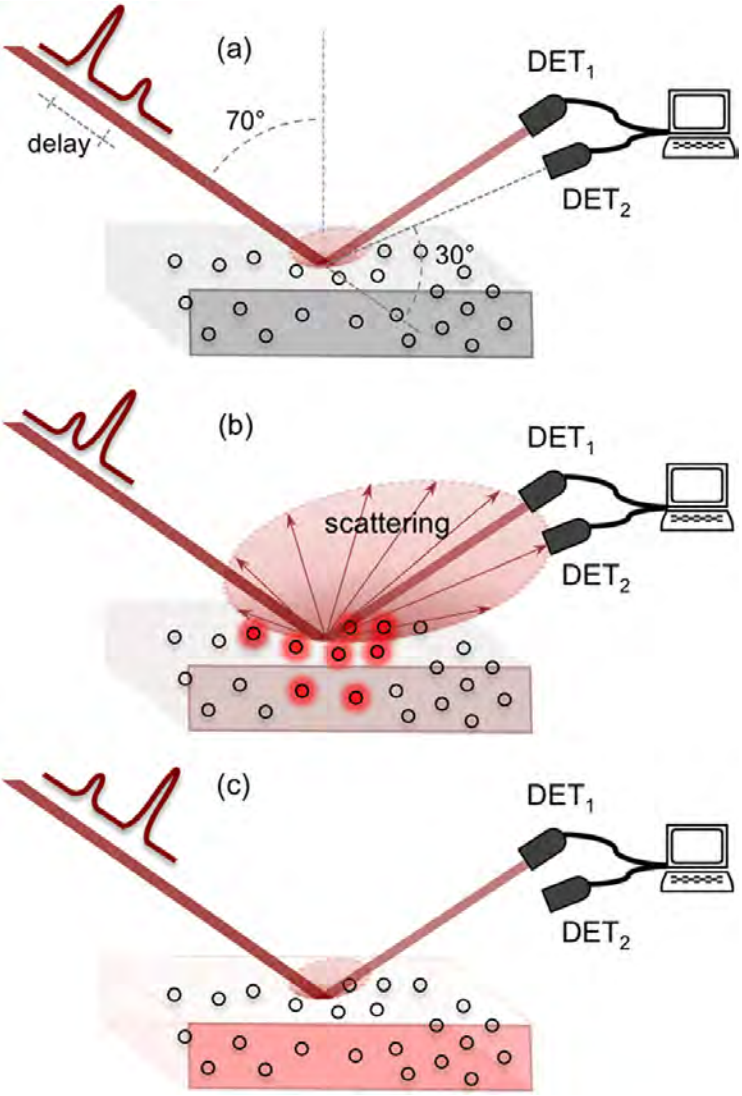

Figure 3.13: Schematic representation of a combined reflectivity and scattering measurement. The detectors, DET$_1$ and DET$_2$, are oriented to measure the specular and off-specular components of reflected light from the sample. The panels, from top to bottom, correspond to different relative probe delays, before, shortly after and longer after pump excitation. In panel (a) the dielectric functions of the matrix and nano crystals are approximately equal, $\varepsilon_m \approx \varepsilon_{nc} \neq 0$, this is because neither phase has a surplus of excited carriers prior to pump excitation. The measured reflected intensities, prior to the pump pulse, for each component are used as a reference. (b) Shortly after the pump $\varepsilon_m > \varepsilon_{nc}$ and $N_{nc} > N_m$, resulting in a negative change seen in specular reflectivity and a positive change in scattered intensity. (c) A long time after the pump $\varepsilon_m \approx \varepsilon_{nc}$ and $N_{nc} = N_m \neq 0$, carriers have 'leaked' into the matrix and the concentration of carriers in the sample is almost uniform. Following this time, recombination of carriers and holes in both the nano crystalline and amorphous phases reduces the average concentration and reflectivity recovers to its initial value. [113]

first be given for the sample utilising a technique such as ellipsometry. The specific details of how to resolve the dynamics in each of the phases are described in Sec. 3.3.5.

3.3 Theoretical Models

The techniques described hitherto all rely on an assumption of how to model the system being studied. In the majority of cases, before the model can be applied, it is crucial to understand the structure of the sample being studied. There are a number of diagnostic methods to measure the structure of materials, which include scanning electron microscopy, atomic force microscopy, x-ray diffraction, Raman spectroscopy etc. Utilising these methods it is possible to build up a mathematical model of the sample for use in analysis. The following section describes how the specific materials that constitute the sample can be modelled, once the general structure of the sample has been determined.

3.3.1 Designing an Optical Model

All optical models start by defining the layer structure of the sample. A method to deal with absorption, transmission and multiple reflections in the samples studied here is described in Sec. 3.1.3, using Fresnel formulae. For spectroscopic techniques it is essential to describe the dielectric functions of each layer with a dispersive model. A number of different models are used in order to model crystalline and amorphous materials. For samples with layers of mixed phases further modelling is required through effective media approximations [114]. The most simple material modelled here is that of silicon dioxide (SiO_2) due to the lack of absorption over the probing energies, a Lorentz model, based on a simple forced, damped harmonic oscillator is used.

The classical Lorentz model describes the electric field polarisation when a negatively charged electron interacts with the positive nucleus to create a dipole moment. Fig. 3.14 shows how the interaction of electron and nucleus can be modelled as a spring, which is forced via the AC field of the probing electric field, $E = E_0 \exp(i\omega t)$. The electron is modelled to oscillate in the direction of this field about the static nucleus, slowed by a frictional force. The system is described in terms of the forces acting upon the

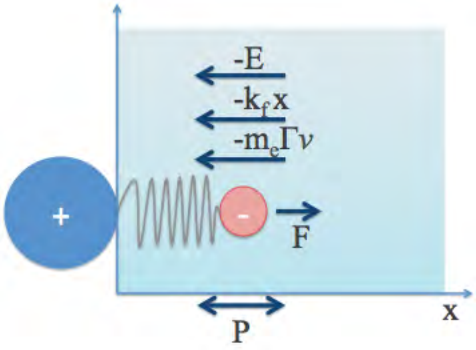

Figure 3.14: Physical picture of the Lorentz model, a negatively charged electron oscillates with respect to a stationary positively charged ion (nucleus). The system is modelled by a forced, damped oscillator with resonant frequency ω_0.

electron by,

$$m_e \frac{d^2x}{dt^2} = -m_e\Gamma\frac{dx}{dt} - m_e\omega_0^2 x - eE_0\exp(i\omega t), \tag{3.72}$$

where m_e and e are the mass and charge of the electron, Γ is the frictional force parameter (describing the scattering of electrons), ω_0 is the resonant frequency of the system and ω is the probing frequency. Solving this differential equation by putting in the solution $x(t) = a\exp(i\omega t)$ we find,

$$a = \frac{-eE}{m_e}\frac{1}{(\omega_0^2 - \omega^2) + i\Gamma\omega}. \tag{3.73}$$

The polarisation can then be given by $P = -eN_e x(t)$, where N_e is the number density of electrons in the system. Substitution into Eq. 3.73 and the common identities $\mathbf{P} = \varepsilon_0\chi\mathbf{E}$ and $\chi = \varepsilon - 1$, provides the equation for dielectric function [78],

$$\varepsilon = \varepsilon_\infty + \frac{(\varepsilon_s - \varepsilon_\infty)\omega_0^2}{\omega_0^2 - \omega^2 + i\Gamma\omega} \tag{3.74}$$

Where ε_∞ is the dielectric function at a frequency far greater than the probe frequency $\omega_\infty \gg \omega$ and ε_s is the dielectric function for DC probing $\omega_s \ll \omega$. As glass (SiO_2) does not display any absorption features in the probing frequencies used here, we can described the dispersion in the absence of scattering parameter Γ. Fig. 3.15 shows the dispersion of SiO_2 over a wavelength range of 400-850nm given values of ε_s, ε_∞ and ω_0 of 2.5, 1 and 12 respectively [115]. As their is no absorption and therefore $\Gamma = 0$ there is no imaginary component of the dielectric function for SiO_2.

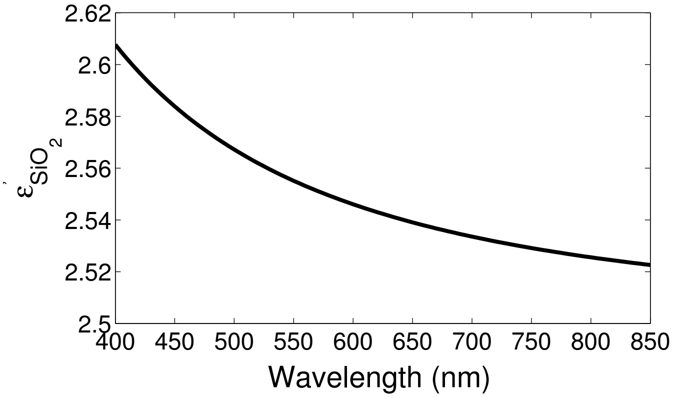

Figure 3.15: Dielectric function dispersion of silicon dioxide, SiO_2. Within the wavelength range probed here, there are no absorption features in this material and therefore there is no imaginary component of the dielectric function. The dielectric function is modelled with a simple Lorentz model.

Amorphous and crystalline materials are much more complex due to the inherent nature of the electronic band structure in the material. There have been many attempts to describe the multitude of materials that are categorised under the umbrella of amorphous and crystalline semiconductors [78, 116–119]. In order to model the sample of nano-crystalline silicon embedded in hydrogenated amorphous silicon (*nc-Si:H*) a model proposed by Forouhi and Bloomer [117, 118] is used to describe both the amorphous and crystalline phases of the nano-crystalline layer as well as the crystalline silicon substrate. The description of this model (FB) is simplest for amorphous materials, in which the imaginary part of the refractive index is given by,

$$k(E) = \frac{A(E-E_g)^2}{E^2 - BE + C} \qquad \omega > \omega_g \tag{3.75}$$

$$= 0 \qquad \omega \leq \omega_g \tag{3.76}$$

where A, B and C are constants which satisfy $A > 0$, $B > 0$, $C > 0$ and $4C - B^2 > 0$, E_g is the optical band gap and E is the probing energy. The real part of the refractive index

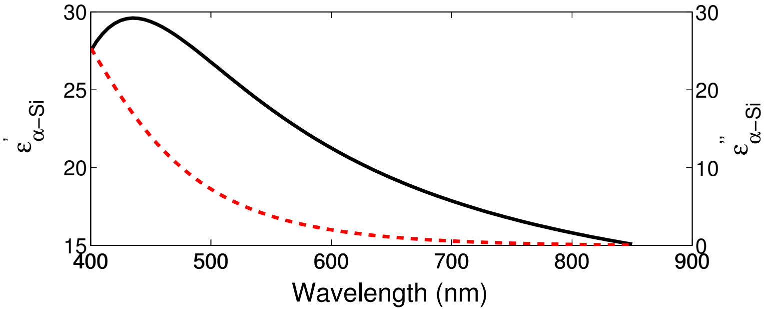

Figure 3.16: Dielectric function dispersion for amorphous silicon α-Si. The real (solid line) and imaginary (dashed line) components of the dielectric function are modelled using a Forouhi-Bloomer [118] approach.

is then related through the Kramers-Kronig relation [120] to give,

$$n(E) = \sqrt{\varepsilon_\infty} + \frac{B_0 E + C_0}{E^2 - BE + C}. \tag{3.77}$$

Where B_0 and C_0 are constants related to A, B and C such that,

$$B_0 = \frac{A}{Q}\left[-\frac{B^2}{2} + E_g B - E_g^2 + C\right], \tag{3.78}$$

$$C_0 = \frac{A}{Q}\left[(E_g^2 + C)\frac{B}{2} - 2E_g C\right], \tag{3.79}$$

$$Q = \frac{1}{2}\sqrt{4C - B^2}. \tag{3.80}$$

For the amorphous phase of the nano-crystalline silicon sample, the dispersion of the complex dielectric function, $\varepsilon^{'}(\lambda)$ and $\varepsilon^{''}(\lambda)$, are shown in Fig. 3.16 fitted using the FB model whose constants are shown in table 3.3. The real and imaginary components of the dielectric function are related to the refractive index and extinction coefficient by $\varepsilon = (n + ik)^2$.

For crystalline samples this model should be adapted. Forouhi and Bloomer adapted the model for amorphous materials by deducing the extinction coefficient $k(E)$. Modelling a one-electron model with a finite excited electron state lifetime [118]. The refractive index $n(E)$ is then related again by the Kramers-Kronig relation as the Hilbert transform of $k(E)$ [118]. Due to the long range symmetry in crystalline materials there are a number of peaks in the dispersion of $k(E)$, these are related to the symmetry points in the Brillouin zone. This leads to a re-casting of equation 3.76 to include these different peaks.

$$k(E) = \left[\sum_{i=1}^{q} \frac{A_i}{E^2 - B_i E + C_i}\right](E - E_g)^2 \qquad \omega > \omega_g \tag{3.81}$$

$$=0 \qquad \omega \leq \omega_g \tag{3.82}$$

the states i correspond to these different symmetry points and the number of these points q are defined by the crystalline structure of the semiconductor in question. Similarly, the equation for the refractive index is given by re-forming equation 3.77 as,

$$n(E) = \sqrt{\varepsilon_\infty} + \sum_{i=1}^{q} \frac{B_{0i} E + C_{0i}}{E^2 - B_i E + C_i}. \tag{3.83}$$

Where A_i, B_i, C_i, B_{0i} and C_{0i} are similar to those described in equations 3.80. For the crystalline phase of the nano-crystalline layer and the crystalline silicon substrate the values of the constants A_i, B_i, C_i, ε_∞ and E_g are given in table 3.3, while the dispersions for each material are given in Figs. 3.17(a) & 3.17(b). N.B. The unusually high value of ε_∞ has been seen in other works [121].

For samples of silicon nitride (SiN_x) a model is used based on that proposed by Tauc *et. al.* [122]. Due to the amorphous nature of the silicon nitride layer a simple model is used, this is a result of the blurring of the states when compared to crystalline materials. Here we define the refractive and extinction coefficient by,

$$n(\omega) = n_\infty + \frac{B(\omega - \omega_j) + C}{(\omega - \omega_j)^2 + \Gamma_j^2}, \tag{3.84}$$

$$k(\omega) = \frac{f_j(\omega - \omega_g)^2}{(\omega - \omega_j)^2 + \Gamma_j^2} \qquad \omega > \omega_g$$

$$= 0 \qquad \omega \leq \omega_g \tag{3.85}$$

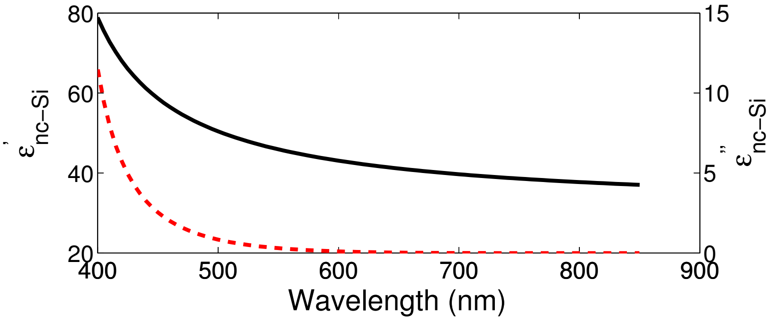

(a)

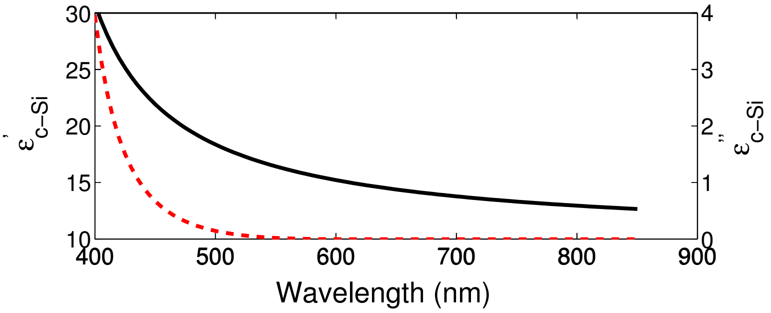

(b)

Figure 3.17: Dielectric function dispersion for crystalline, *c-Si*, and nano crystalline silicon, *nc-Si*. The real (solid line) and imaginary (dashed line) components of the dielectric function are modelled using a Forouhi-Bloomer [118] approach.

where B and C are positive constants relating to the parameters Γ_j, f_j, the probing frequency ω and the band gap frequency ω_g. The values of the parameters n_∞, ω_g, f_j, ω_j and Γ_j are shown in table 3.3 and the related dispersions of $n(\lambda)$ and $k(\lambda)$ are shown in Fig. 3.18.

Having defined each of the layers' dispersions the final task is to define the effective dispersion of any mixed phase layers. In order to model the nano-crystalline silicon inclusions embedded in amorphous silicon we need to mix the two dispersions shown in Figs. 3.17(a) & 3.16. The Bruggeman effective-medium approximation (EMA) [123, 124] is a mixing rule for heterogeneous composites. For a composite material with complex dielectric constants ε_1 and ε_2 with volume filling fractions of f and $1-f$ respectively the EMA model assumes a mixture of approximately spherical grains. The model holds for spherical inclusions that are well separated such that the total volume can be considered dilute [125, 126]. The effective dielectric function of the material ε_{eff}

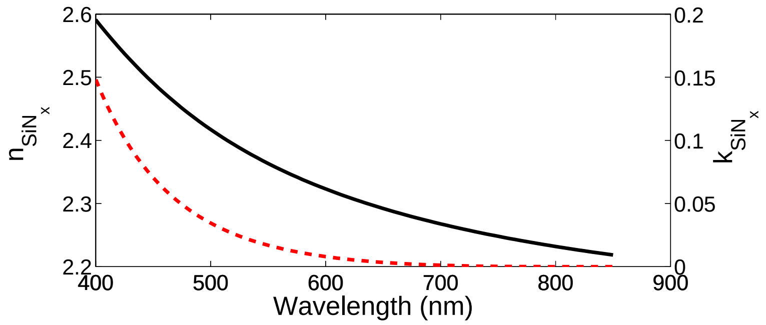

Figure 3.18: Refractive index dispersion for silicon nitride, SiN_x. Refractive index, n (solid line) and extinction coefficient, k (dashed line) are modelled using a Tauc-Lorentz model [122].

relies on the assumption (known as self-consistent effective medium approximation) that the material surrounding the spherical inclusions can be modelled as a homogeneous matrix and also that first order approximation for a dilute composite can be used [127–129].

The derivation of the EMA model used to describe the effective dielectric function of the nano-crystalline silicon is described by Zhang *et. al.* [130], who presents a self-consistent three-dimensional Bruggeman effective medium model which has continuous spectral density. Self-consistency results in the equation for a two phase composite material that follows,

$$f\frac{\varepsilon_{\text{eff}}-\varepsilon_1}{2\varepsilon_{\text{eff}}+\varepsilon_1}+(1-f)\frac{\varepsilon_{\text{eff}}-\varepsilon_2}{2\varepsilon_{\text{eff}}+\varepsilon_2}=0. \tag{3.86}$$

Where ε_1 and ε_2 are the dielectric functions of nano-crystals and amorphous silicon matrix respectively, f is the volume filling fraction of the nano-crystals and ε_{eff} is the effective dielectric function of the layer as a whole. Solving this equation to provide a relation for ε_{eff} in terms of the other 3 parameters gives,

$$\varepsilon_{\text{eff}}=\frac{1}{4}(\gamma+\sqrt{\gamma^2+8\varepsilon_1\varepsilon_2}), \tag{3.87}$$

where the parameter γ is represented by the symmetric function $\gamma=(3f_1-1)\varepsilon_1+(3f_2-1)\varepsilon_2$, and f_1 and f_2 are the volume filling fractions of each of the two phases of the

Table 3.3: Fitted parameters for dielectric function dispersions of α*-Si, c-Si, nc-Si* and *SiN*$_x$ modelled with Forouhi-Bloomer and Tauc-Lorentz models.

Sample	ε_∞	A	B	C	E_g
α-Si	3.71	1.09	6.67	12.72	1.27
	ε_∞	A_i	B_i	C_i	E_g
c-Si (substrate)	5.664	0.011	6.86	11.778	2.065
		0.054	7.361	13.625	
		0.153	8.632	18.817	
		0.047	10.314	26.859	
nc-Si	19.985	0.011	6.86	11.778	1.7058
		0.054	7.361	13.625	
		0.153	8.632	18.817	
		0.047	10.314	26.859	
	n_∞	ω_g	f_j	ω_j	Γ_j
SiN$_x$	1.8165	1.5656	0.2210	4.3038	1.4505

composite. Fitting of the EMA model should be performed based on XRD and Raman analysis of the sample in question, alternatively spectroscopic ellipsometry provides a useful tool to fit the volume filling fraction of complicated composite layers. The effective dispersion of the nano-crystalline silicon inclusions layer is plotted in Fig. 3.19 based on a filling fraction of $f \simeq 0.3$ and the dispersions for *nc-Si* and α*-Si* from Figs. 3.17(a) & 3.16.

Having created this complicated optical model, based on measurements of XRD, Raman, SEM etc., for each of the samples under study, the quality of the model can be tested. The sample of *nc-Si:H* is modelled using Fresnel formulae for a 4-layer system as per section 3.1.4, the top oxidation layer of SiO$_2$ is fitted by varying the thickness of the layer between 0.1-10nm. The 2nd layer utilises the EMA model described above as well as the dispersions of α*-Si* and *nc-Si* described by the FB model. A third layer of SiO$_2$ is modelled using the simple Lorentz model and finally the substrate is modelled with the dispersion of *c-Si*. A commercial ellipsometer (Horiba Jobin-Yvon UVISEL) has been used to measure the ellipsometric parameters $\Psi(\lambda)$ and $\Delta(\lambda)$ and using equation 3.11 along with an iterative fitting procedure to vary the film thicknesses, the quality of the optical model is assessed. Fig. 3.20 shows that the optical model is of very good

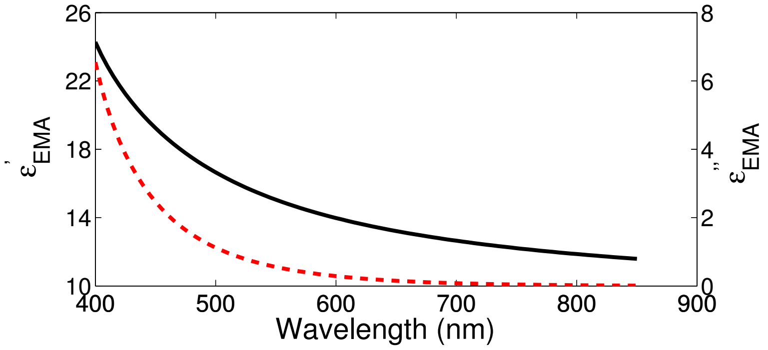

Figure 3.19: Effective dielectric function dispersion for nano crystalline silicon embedded in amorphous silicon matrix, *nc-Si:H*. The dielectric function is found by mixing the dispersions of nc-Si and α-Si using an effective media approximation proposed by Bruggeman [123].

quality, fitting with a mean squared error defined by,

$$MSE = \frac{1}{2N-M}\sum_{i=1}^{N}\left[\left(\frac{(\Psi_i^{cal}-\Psi_i^{exp}}{\sigma\Psi_i^{exp}}\right)^2+\left(\frac{\Delta_i^{cal}-\Delta_i^{exp}}{\sigma\Delta_i^{exp}}\right)^2\right] \tag{3.88}$$

where N is the number of data points, M is the number of parameters (2) and σ is the standard deviation of the experimentally acquired data Ψ_i^{exp} and Δ_i^{exp}. Using this equation we find a value of $MSE = 1\times10^{-4}$. The SiN_x sample is a much simpler system constituting of only a silicon nitride thin film and *c-Si* substrate, here the SiN_x thin film is modelled using the modified Tauc-Lorentz dispersion. The model is compared to the experimentally measured values of the ellipsometric parameters in Fig 3.21 and fits with a $MSE = 0.0018$. A summary of the fitting parameters for the *nc-Si:H* and SiN_x samples are shown in table 3.4

Table 3.4: Parameters for fitting of ellipsometry measurements performed with a commercial ellipsometer. The film thickness for the multilayer structures and volume fraction of mixed phase layers are used for fitting. The mean square error (MSE) for each fitting is also given.

Sample	d_1	d_2	d_3	f	MSE
nc-Si:H	10.7nm	482nm	188nm	0.27	1×10^{-4}
SiN_x	440nm	-	-	-	0.0018

Note: high value of d_1 due to surface roughness.

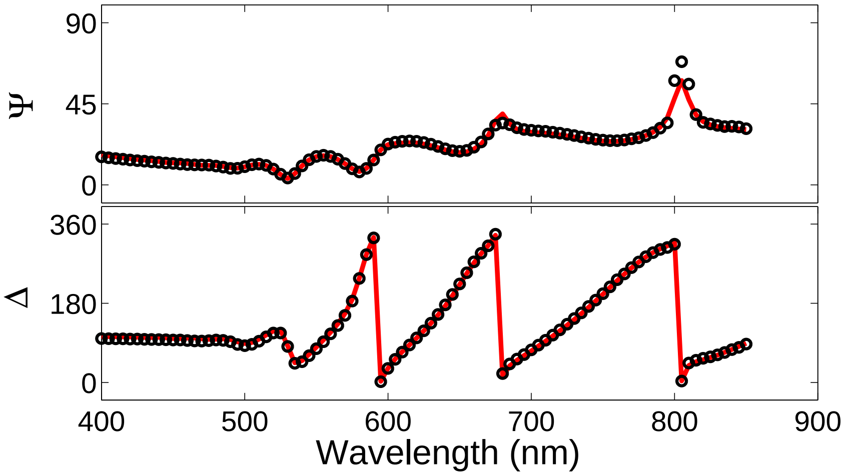

Figure 3.20: Ellipsometry measurement performed with a commercial ellipsometer (Horiba Jobin-Yvon) providing Ψ and Δ values over a range of wavelengths between 400-900nm (symbols). The values are fitted with an optical model using Fresnel formulae (solid line) and making use of the dielectric function dispersions outlined in this section. The *nc-Si:H* sample is modelled based on measurements of SEM, XRD and μ-Raman.

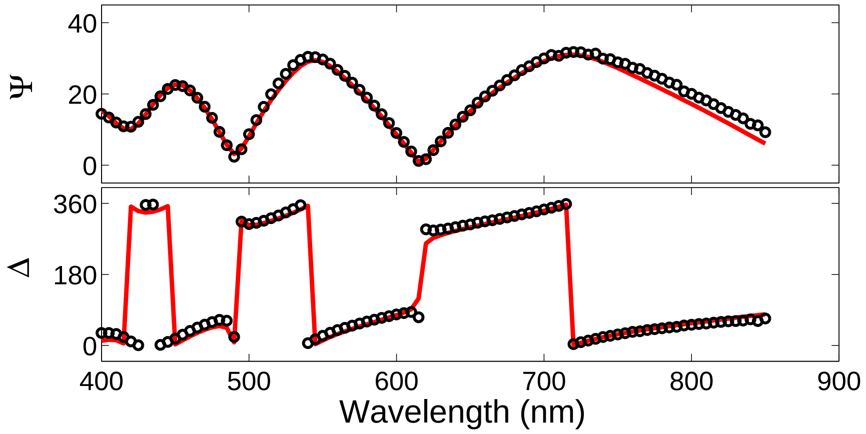

Figure 3.21: Ellipsometry measurement performed with a commercial ellipsometer (Horiba Jobin-Yvon) providing Ψ and Δ values over a range of wavelengths between 400-900nm (symbols). The values are fitted with an optical model using Fresnel formulae (solid line) and making use of the dielectric function dispersions outlined in this section. The SiN_x sample is modelled based on the measurements of XRD and absorption analysis.

3.3.2 Drude Theory

Thus far we have only considered how to describe theoretically the optical properties of samples while in their equilibrium state i.e. with no optical (or otherwise) pumping of electrons. In order to model accurately the dielectric function change as a function of the probe delay, we must consider how to adapt the dielectric dispersions given in section 3.3.1. If we assume free electron absorption (FCA) takes place within the semiconductor a resultant change in the dielectric function will be observed. Considering the electronic band structure for a generic semiconductor, as shown in Fig. 3.22. When the conduction band displays a large number of free carriers (holes) ($> 10^{18}\text{cm}^{-3}$), the semiconductor displays a metallic-like behaviour. If one of these electrons somehow scatters, either from a point defect, another electron, a phonon etc., it collects some change in momentum $k \rightarrow k + k'$. This change in wave vector allows free carrier absorption to occur, changing the absorption coefficient α_{FCA}. Therefore it is trivial to see that the absorption coefficient increases with carrier (hole) density, N_e. The transport of the free carriers within the conduction band is usually described by the Boltzmann equation or Fermi integrals [131], however we limit this description of FCA to classical Drude theory.

We treat the theory of electron absorption here in a similar manner to that of the Lorentz model in section 3.3.1. By assuming an electrostatic force F_x applied to the semiconductor such that the electrons move with a speed $\langle v \rangle$ in the direction of the force x until it scatters with a time interval $\langle t \rangle$. Here the parentheses $\langle \rangle$ signify the average value of velocity and scattering time of the electrons. The free electrons are therefore described by,

$$F_x = m_{\text{eff}} \frac{\langle v \rangle}{\langle \tau \rangle}, \tag{3.89}$$

where m_{eff} is the effective mass of the carriers. We also note that the electron's velocity depends on the applied electric field E such that $\langle v \rangle = -\mu E$, with μ being the drift mobility of the electrons. Making use of the the fact that the force is related to the field

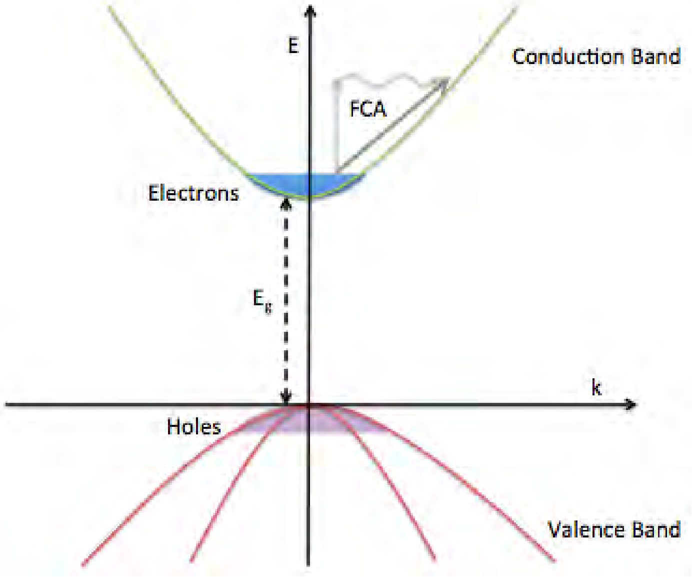

Figure 3.22: Representation of free carrier absorption (FCA) in semiconductor materials. Carriers can be excited within the conduction band via phonon assisted transitions in order to gain the momentum k required to move along the parabolic energy band.

by $F_e = -eE$ we find,

$$\mu = \frac{e\langle t\rangle}{m_{\text{eff}}}. \tag{3.90}$$

This shows us that as the drift mobility of the electrons increases, the time between scattering events increases and therefore the absorption of free carriers α_{FCA} goes down. Given the definition of the conductivity $\sigma = eN\mu$ and recalling Eq. 3.89 we find,

$$m_{\text{eff}}\frac{d^2x}{dt^2} = -F_x + F_e = -\frac{m_{\text{eff}}}{\langle\tau\rangle}\frac{dx}{dt} - eE_0\exp(i\omega t). \tag{3.91}$$

Using the solution $x = a\exp(i\omega t)$ in the same manner as in the derivation of the Lorentz oscillator and setting $\Gamma \equiv \langle\tau\rangle^{-1}$, the dielectric function for free carrier absorption is given by,

$$\begin{aligned}\varepsilon &= \varepsilon_\infty - \frac{Ne^2}{m_{\text{eff}}\varepsilon_0}\frac{1}{\omega^2 - i\omega\Gamma},\\ &= \varepsilon_\infty - \frac{\omega_p^2}{\omega^2 - i\omega\Gamma}.\end{aligned} \tag{3.92}$$

The plasma frequency,

$$\omega_p = \sqrt{\frac{Ne^2}{m_{\text{eff}}\varepsilon_0}} \tag{3.93}$$

and scattering frequency Γ can then be used as fitting parameters for time-resolved measurements of the dielectric function as described in sections 3.2.1, 3.2.2 & 3.2.4. Multiplying through by the complex conjugate of the denominator provides the free carrier absorption contribution for both the real and imaginary components of the dielectric function.

$$\varepsilon' = \varepsilon_\infty - \omega_p^2 \frac{\omega^2}{\omega^4 + \Gamma^4} \tag{3.94}$$

$$\varepsilon'' = -\omega_p^2 \frac{\Gamma\omega}{\omega^4 + \Gamma^4} \tag{3.95}$$

3.3.3 Fitting Drude Parameters with Pump Fluence

Fitting of the Drude model to the time-resolved reflectometry is achieved in conjunction with the optical model to find the change in reflection coefficients $r_p(\tau)$ and $r_s(\tau)$. If a single time delay is picked out and the pump fluence varied it is possible to plot the plasma frequency as a function of the pump fluence F. Given equation 3.93 and the relation between the pump fluence and number of carriers created,

$$N = \frac{A_\alpha F}{d\hbar\omega} \tag{3.96}$$

where $A_\alpha = \alpha/\pi r^2$ is the absorbance of the sample, d is the thin layer thickness and ω is the probing frequency, the relation between plasma frequency and the effective mass m^* is given by,

$$\omega_p^2 = \frac{AFe^2}{d\varepsilon_0\hbar\omega m_e}\frac{1}{m^*} = \alpha F. \tag{3.97}$$

$$\alpha = \frac{Ae^2}{d\varepsilon_0\hbar\omega m_e m^*} \tag{3.98}$$

The slope of equation 3.97, α, provides the effective mass of the carriers.

3.3.4 Ellipsometry Fitting

Having seen how a static spectroscopic ellipsometry measurement is performed (section 3.1.7), the model can be adapted to fit data as a function of the probe delay. To apply a model of carrier absorption, we must first decide which layers are likely to be effected. Once the 'active' layers have been decided the dielectric function dispersions can be fitted using a model (such as Drude) by finding the contribution to the (complex) dielectric function that fits the ellipsometric parameters Ψ and Δ. In order to do this the unperturbed dielectric function (ε_0) is modified as follows,

$$\begin{aligned} \varepsilon^{'}(t) &= \varepsilon_0^{'} + \varepsilon_D^{'} = \varepsilon_0^{'} - \omega_p^2 \frac{\omega^2}{\omega^4 + \Gamma^2\omega^2}, \\ \varepsilon^{''}(t) &= \varepsilon_0^{''} + \varepsilon_D^{''} = \varepsilon_0^{''} + \omega_p^2 \frac{\Gamma\omega}{\omega^4 + \Gamma^2\omega^2}. \end{aligned} \tag{3.99}$$

For each time delay corresponding to a pair of $\Psi(\lambda,t)$ and $\Delta(\lambda,t)$, equations 3.99 are used to iteratively best fit the change in dielectric constant, making use of equation 3.88. The fitting parameters here are the Drude parameters $\omega_p(t)$ and $\Gamma(t)$, which provide an insight into the carrier dynamics undergone after intense optical pumping.

3.3.5 Scattering Theory

In traditional pump-probe measurements in which the reflectivity is measured as a function of time $R(t)$ the dielectric function can be resolved by [34, 132],

$$R(t) = \left| \frac{1 - \sqrt(\varepsilon)}{1 + \sqrt(\varepsilon)} \right|^2 \tag{3.100}$$

The dielectric function can then be related to the number of free carriers (N) excited in the sample by the Drude equation 3.92. The Drude parameters ω_p and Γ have been measured extensively in samples of bulk crystalline [32, 133, 134] and bulk amorphous silicon [135]. However, when measurements are made in composite materials the contribution from each of the phases are mixed and the effective dielectric function is measured instead. This can be modelled with a simple Maxwell-Garnett approximation.

$$\varepsilon_{\text{eff}} = \varepsilon_m + 3f\varepsilon_m \frac{\varepsilon_{nc} - \varepsilon_m}{\varepsilon_{nc} + 2\varepsilon_m - f(\varepsilon_{nc} - \varepsilon_m)} \tag{3.101}$$

where ε_m, ε_{nc} are the dielectric function of the host matrix and nano-crystals respectively and f is the volume filling fraction of the nano-crystals. Through equations 3.92 & 3.101 we find that the change of the effective dielectric function depends on both the number of carriers in the nano-crystals $N_{nc}(t)$ as well as the number of carriers in the host matrix $N_m(t)$. Therefore measurements of the reflectivity cannot provide knowledge of the separate functions of carrier density without resorting to additional assumptions.

One can also measure the scattering intensity, dependent on the scattering efficiency Q_{scat}, such that,

$$I_s = KI_iQ_{\text{scat}} \tag{3.102}$$

where I_i is the probing intensity and K is a geometrical factor describing the collection efficiency of the scattered light from the irradiated volume [136]. In this case the dielectric functions of both the nano-crystals and the host matrix are described within the scattering efficiency,

$$Q_{\text{scat}} = \frac{8}{3}\left(\frac{2\pi < a >}{\lambda}\right)^4 \left|\frac{\varepsilon_{nc} - \varepsilon_m}{\varepsilon_{nc} + \varepsilon_m}\right|^2, \tag{3.103}$$

where $< a >$ is the average size of the embedded spherical inclusions and λ is the probing wavelength. Measurement of the scattered intensity therefore provides knowledge of the carrier densities within the nano-crystals and the matrix, but this time instead of their sum it provides their difference. So combining measurements of reflectivity and scattering it is possible to resolve unambiguously the contribution of free carriers to the dielectric function from both phases of a composite material.

Chapter 4

Results & Discussion

This chapter outlines the results for experiments proposed in the *Experimental Methods & Theory* chapter. Discussion of the results are presented in each section, summarising salient information obtained about carrier dynamics in samples of nano crystalline silicon *nc-Si:H* and silicon nitride SiN_x. In particular the distribution of electrons shortly after excitation is discussed, revealing surprising behaviour of a classical electron gas in samples of *nc-Si:H*.

4.1 Reflectometry

A basic reflectometry measurement is outlined in Sec. 3.1. A measurement of the change of reflectivity is performed using a standard pump-probe apparatus. A ~50fs pulse (shown in red in Fig. 4.1) is split into two unequal pulses of $\sim 600\mu W$ and $\sim 6\mu W$ using a pellicle beamsplitter and recombined non-collinearly onto a sample of *nc-Si:H*. Pump and probe spot sizes of $\sim 250\mu m$ and $\sim 50\mu m$ were used providing a pump fluence of ~1.2mJ/cm^2. An angle of incidence of $\phi_i = 65^\circ$ was used, close to the samples Brewster angle. A step size of 10fs was used to delay the probe with respect to the pump pulse. The pump-probe spatial overlap was checked using a microscope objective and CCD camera, while the temporal overlap is checked using a standard intensity autocorrelation [18] measurement at the sample position.

A silicon photodiode and lock-in amplifier were used to measure the reflected inten-

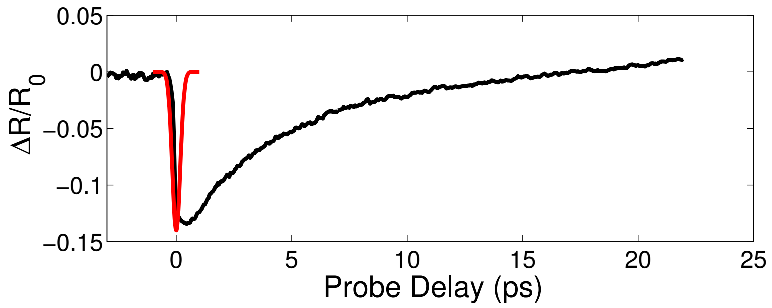

Figure 4.1: Transient reflectivity data (solid black line) plotted as a function of probe delay time (τ). The Reflectivity data is normalised to the initial reflectance (prior to the pump $\tau < \tau_0$) to provide $\Delta R/R_0$, indicating the fractional change in reflectance following excitation. The pump pulse duration (solid red line) and temporal position are shown, indicating that the reflectivity changes on the same time scale as the leading edge of the pulse function.

sity while minimising the noise from other sources. The reflectivity change $\Delta R(\tau)/R_0$ has been measured for probe delays up to 23ps following excitation, in which time the reflectivity change has reached zero. The reflectivity change consists of an excitation region (0-0.5ps) and two decay regions (0.5-2ps and 2-22ps). The reflectivity change is plotted in Fig. 4.1, we propose that the change in reflectivity is solely due to the change of refractive index $N \equiv n - ik$ of the *nc-Si* layer, however due to the restrictive nature of the measurement the component of the complex refractive index (n or k) responsible is not resolved and instead in this type of measurement it is left to speculation about which is responsible. The magnitude of the change seen here is much larger ($10\times$) than that seen in bulk silicon (1%) for similar excitation parameters [19, 32], we propose that the large change in reflectivity (up to 15%) is likely due to the amplification of the signal by multiple reflections in the sample as well as an enhanced carrier absorption through the crystallites, which is discussed in detail in the following sections (Sec. 4.4).

Measuring as a function of pump fluence between 0.6mJ/cm^2-2mJ/cm^2, below the cumulative melting fluence for silicon based samples [35], provides a means to see how the change in reflectivity varies as the number of carriers in the sample is increased. For the range of pump fluences measured, a linear variation of reflectivity change was seen (see Fig. 4.11). This implies that the processes responsible are linear. However a nonlinear contribution cannot be discounted as the range of pump fluences used cover a relatively small region (< 1 order of magnitude), below which no reflectivity change is detected and above which, the sample approaches its melting fluence of $4.4 mJ/cm^2$ [26].

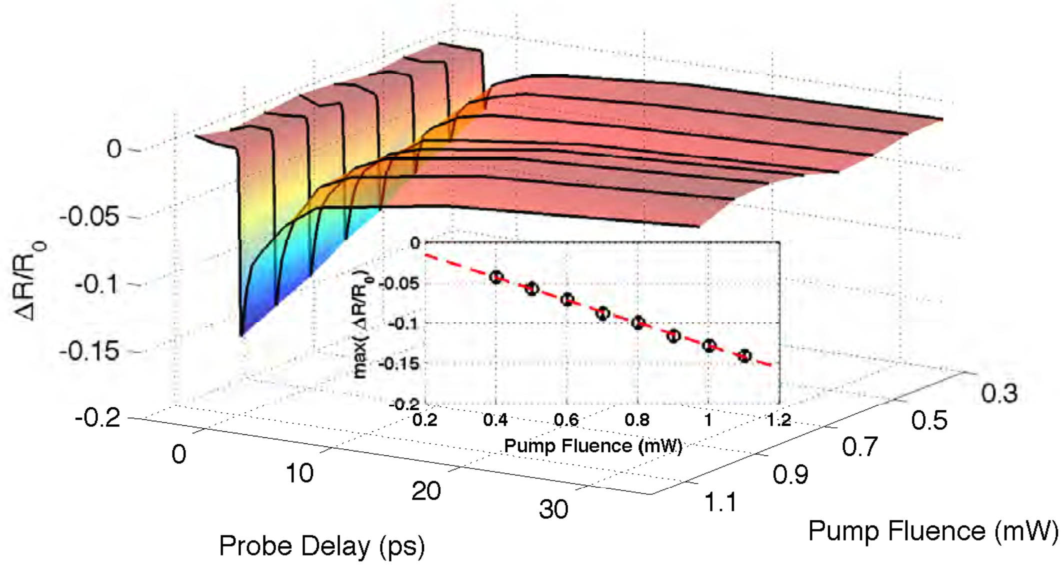

Figure 4.2: Transient reflectivity change $\Delta R/R_0$ as a function of both probe delay (τ) and pump fluence. The reflectivity is measured with a photodetector, averaging over all probing wavelengths. Inset: maximum change in reflectivity as a function of pump fluence, experimental data points (symbols) and linear fit (dashed line).

Replacing the silicon photodetector with a spectrometer (Ocean Optics QE65 Pro) one can measure how the reflectance changes with the probing wavelength. Figure 4.3 shows that over the bandwidth of the probe pulse (~60nm centred about 795nm) the reflectance varies from a negative change at low probing wavelengths to a positive change at high wavelengths. The point at which the reflectance change flips between these two regions shows a characteristic shift (consistent with the blue shift of a Fabry-Perot fringe as the dielectric function decreases), with probe delay (τ), which can be modelled using Drude theory for free carrier excitation. This is discussed in further detail in section 4.3.

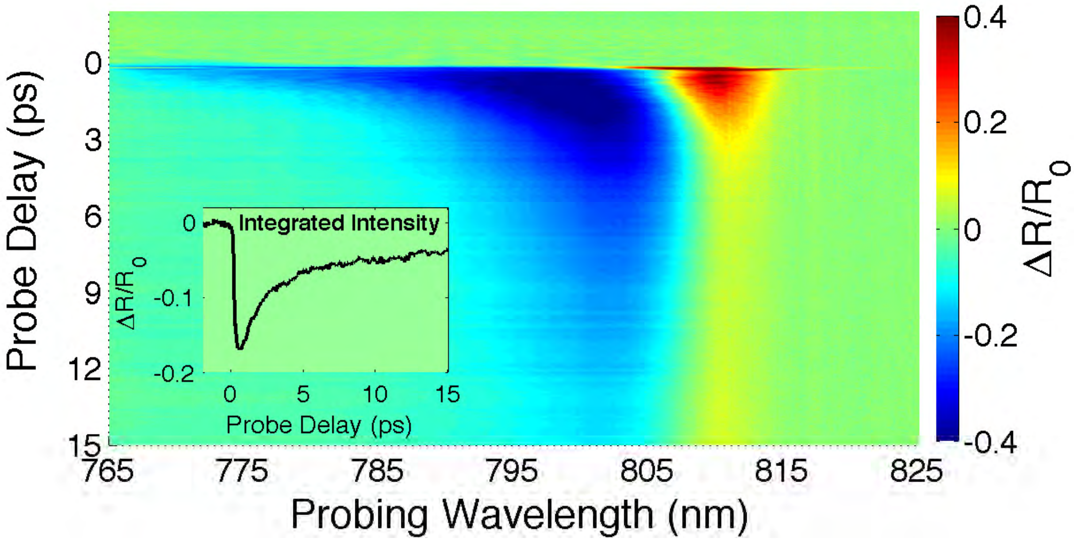

Figure 4.3: Transient reflectivity change as a function of probing wavelength, measured using a spectrometer (Ocean Optics QE65 Pro). Inset. Integrated reflectivity data from main graph.

4.2 Scattering

The discussion and results in this section are based on the paper: **Resolving the ultrafast dynamics of charge carriers in nano composites, Applied Physics Letters, 100, 241906 (2012)** [113]

The results from a traditional pump-probe reflectivity measurement are presented alongside scattering measurements in Fig. 4.4. The data here have been normalised with respect to the initial values prior to the pump excitation such that; $\Delta R(t)/R_0 = (R(t) - R_0)/R_0$ and $\Delta I_S(t)/I_0 = (I_S - I_0)/I_0$. Both signals show an almost instantaneous change upon excitation with the pump pulse, remarkably, the reflectivity change ΔR shows an initial negative change, while the scattering intensity ΔI_S shows an initial positive change. Furthermore, it can be seen that the reflectivity decay lasts longer, implying the contribution from two different relaxation mechanisms [113]: a rapid decay (proceeding on the same timescale as the scattered intensity change), taking place over the first few picoseconds, and a slow decay proceeding over tens of picoseconds. The absence of the slow component in the scattered intensity profile suggests (via Eq. 3.103) that the difference between the dielectric functions of the *nc-Si* and the α-*Si* matrix reach an indistinguishable level during the first few picoseconds.

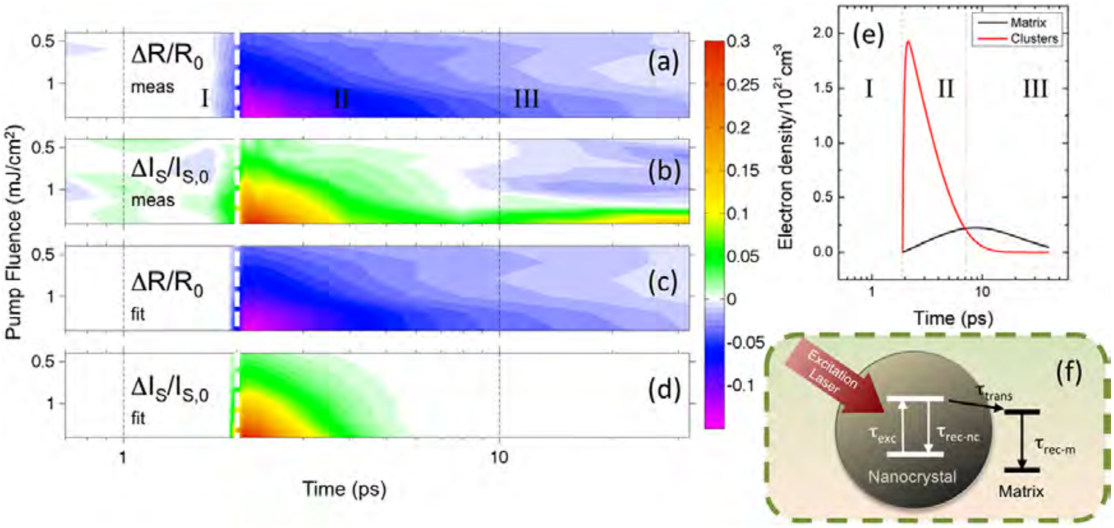

Figure 4.4: Time-resolved optical response of the free carriers in *nc-Si:H*. (a), (b) Measured and (c), (d) calculated 2-D contour maps of the transient reflectivity change $\Delta R/R_0$ and scattering intensity change $\Delta I/I_0$. The x-axis shows the probe delay (on logarithmic scale) while the y-axis corresponds to the fluence of the pump laser. The pump arrival time is highlighted with a white dashed line at ~2 ps. The regions I, II, and III correspond to the conditions described in Fig. 3.13. (e) The carrier dynamics in the nanocrystals and the matrix reconstructed from (c) and (d) at a fluence of 1 mJ/cm^2. (f) Schematic representation of the photo-excited carrier dynamics in the material; carriers are pumped in the nanocrystals with a response time τ_{exc}, excited carriers can recombine within the *nc-Si* through $\tau_{\text{rec-nc}}$ or leak into matrix states at a rate τ_{trans} which then recombine within $\tau_{\text{rec-m}}$ (see Table 4.1) [113]. NB. The increase in $\Delta I/I_0$ in (b) is likely due to lattice heating when operating at maximum fluence, which is not taken into account in our analysis.

We assume that thermal effects do not contribute significantly to the signal as the fractional change of the dielectric function expected due to the lattice temperature increase, would be indistinguishable at the pump fluences used [133, 134]. We also expect that changes due to thermal effects take place over 4ps and longer, later than the main optical response observed. Using equations 3.102 & 3.103, the transient change in both reflectivity and scattering intensity can be reconstructed (see Figures 4.4(c) and 4.4(d)). This is achieved by iteratively fitting the contribution to the dielectric function from the change in carrier density in both the *nc-Si* and the *α-Si* matrix. The fitting parameters $N_{nc}(\tau)$ and $N_m(\tau)$ can be well described by a combination of exponential functions (shown in Fig. 4.4(e)) from which relevant time scales can be extracted. These are tabulated in table 4.1.

Table 4.1: Characteristic time scales in *nc-Si:H*, measured using reflectivity and scattering measurements. Data here has been obtained by fitting of Figs. 4.4(a) & 4.4(b). [113]

Component	*nc-Si*	α-*Si*
Excitation time, τ_{exc} (fs)	85±10	...
Decay time, τ_{dec} (ps)	2.2±0.2	...
Transfer time, τ_{trans} (ps)	4.0±0.7	
Recombination time, τ_{rec} (ps)	4.9±0.5	22±4
N at 0.4 mJ/cm^2 (10^{20}cm^{-3})	8.1±0.1	1.7±0.1
N at 1.4 mJ/cm^2 (10^{20}cm^{-3})	27.0±0.1	2.6±0.1

The values and timescales of the carrier densities, $N_{nc}(\tau)$ and $N_m(\tau)$, reveal salient information about the carrier dynamics occurring in these types of composite materials, not achievable with other methods [44, 121, 137]. An excitation of the *nc-Si* was measured to be almost instantaneous with pump excitation, proceeding on the order of the pulse duration, $\tau_{exc} = 85$fs. However, the maximum concentration of carriers in the host matrix is reached a few picoseconds later. By correlating the carrier densities in the nano-crystals and the matrix τ_{dec} we propose that the decay in the *nc-Si* consists of two components, a recombination of carriers within the crystals τ_{rec_nc} and a transfer of charge to the host matrix τ_{tran}. These processes are depicted in Fig. 4.4(f), where the recombination time is approximated by,

$$\tau_{rec\_nc} \approx \tau_{dec}\tau_{trans}/(\tau_{trans} - \tau_{dec}) = 4.9ps \tag{4.1}$$

The estimate of the recombination time here is similar to the surface state decay times measured in nanocrystalline films (3ps) [109]. Furthermore, the slow decay time measured in the α-*Si* matrix of 22ps is similar to that measured in bulk amorphous silicon [135], which is attributed to multiparticle recombination.

The consistency of this approach has been verified by measuring the reflectivity and scattering intensity as a function of the fluence at a fixed probe delay of ~100fs. These measurements are seen in Fig. 4.5. Also plotted is the calculated relative scattering

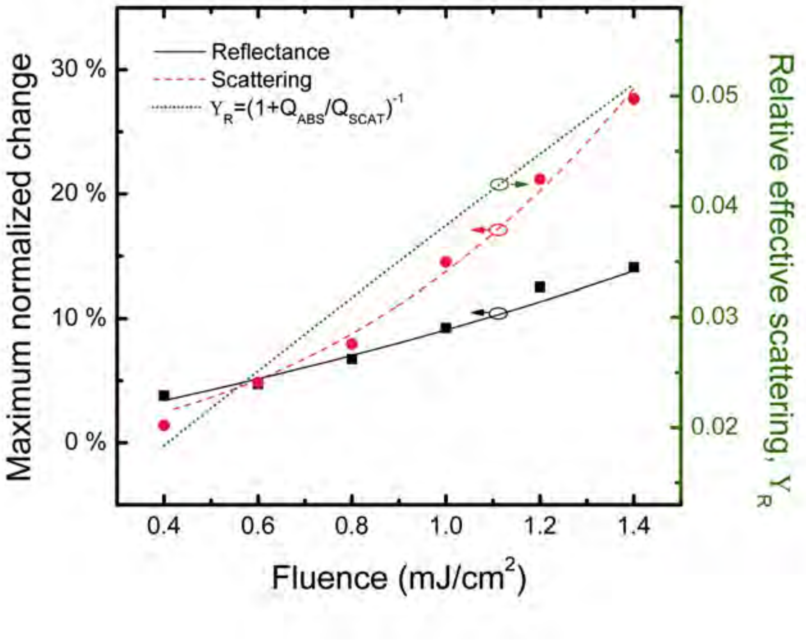

Figure 4.5: Dependence of the optical properties of *nc-Si:H* on pump fluence. The LHS y-axis shows the maximum change in reflectivity change and scattering intensity while the RHS y-axis corresponds to the relative scattering efficiency. Symbols represent experimental data, while lines represent calculations. [113]

efficiency, $Y_{scat} = Q_{scat}/(Q_{scat}+Q_{abs})$, where Q_{abs} is the absorption efficiency. It should be noted that absorption exceeds the scattering intensity significantly. This means that scattering can only be observed from *nc-Si* close to the surface, due to the dominance of absorption deeper within the layer. Comparison of the scattering and absorption probabilities also implies that the contribution due to multiple scattering events toward the total scattering intensity is insignificant, as statistically, following a single scattering event, the scattered photon is then absorbed [113].

4.3 Multi-Incidence Angle & Fluence Dependent Reflectivity Measurements

The discussion and results in this section are based on the paper: **Enhanced carrier-carrier interaction in optically pumped hydrogenated nanocrystalline silicon, Applied Physics Letters, 101, 14 (2012)** [103]

As described in the previous section, we have taken time-resolved measurements of the reflectivity using a standard femtosecond pump-probe setup. The details of the delay line and the calibration procedure can be found in section 3.1 and previous publications by the group [113, 138]. The laser parameters and alignment procedure are the same as used for the reflectometry measurements in the previous section with the reflected probe pulse being wavelength-analyzed using a spectrometer (Ocean Optics QE65 Pro).

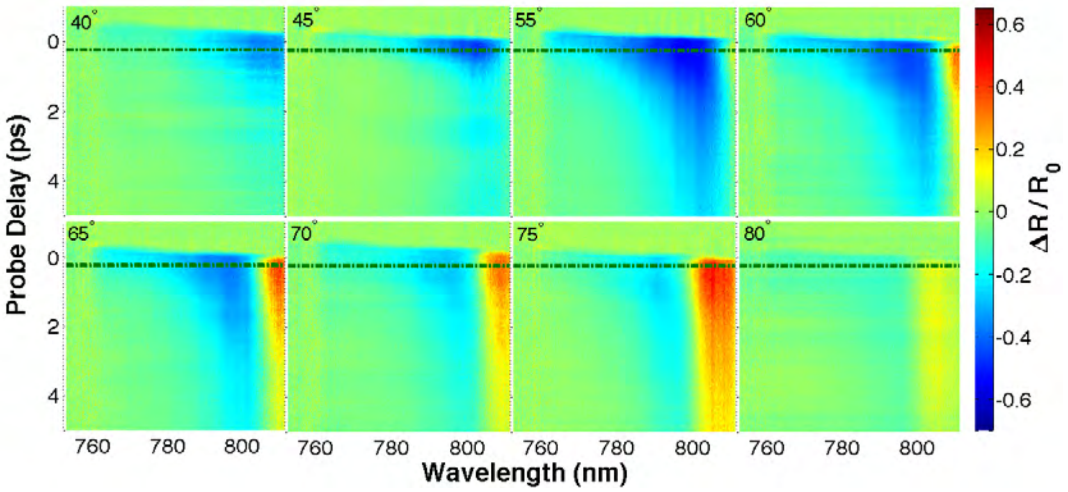

Figure 4.6: Transient change in reflectivity $\Delta R/R_0$ as a function of probing wavelength and probe delay. 2D contour plots show experimental data for incidence angles between 40°-80°. Dash-dot line shows probe delay ~350fs following excitation. [103]

The Drude equation (3.92) shows that pumping of the sample leads to a change in the dielectric function ε_{eff}, resulting in a change of the samples reflectance R. This enables us to resolve the parameters of the Drude model using reflectivity measurements. However, to determine the plasma frequency ω_p and scattering rate Γ simultaneously, two independent measurements should be made. In some works this is performed by measuring the reflectivity and transmission of the sample. However, this is not always possible, in particular for opaque and optically dense samples which transmit light poorly. Alternatively, one can estimate these parameters by assuming that the optically absorbed energy is transferred completely to the production of electron-hole pairs and then guess the optical mass of the carriers. In this section we have measured the pump-probe reflectivity of the sample as a function of wavelength for a fixed pump fluence of 2.5±0.5mJ/cm^2. The results of the pump-probe measurements for incidence angles between 40°-80° are shown in Fig. 4.6. It is important to note that despite a considerable change in reflectance of the sample being expected as the incidence angle is scanned (up to 50%), the major contributing factor to the change in reflectance following the optical excitation is due to changes in the dielectric function of the *nc-Si:H* layer. We analyse the reflectivity as a function of wavelength for a fixed probe delay time of $\tau \sim$350fs. This delay time is chosen as it allows sufficient time for the plasma to build up and the electrons to reach equilibrium, while being short enough to avoid significant population decay due to recombination or diffusion of carriers. These fixed τ curves of reflectivity change versus probing wavelength are shown in Fig. 4.7. A distinct transition is seen as the probing wavelength is scanned, exhibiting a Fabry-Perot fringe attributed to a change in the real part of the dielectric function. The position of the fringe shifts to shorter wavelengths as the optical path inside the sample increases with the incidence angle. This observation is consistent with with the blue-shift of the Fabry-Perot fringes as the dielectric function within the *nc-Si:H* layer decreases due to the pumped free carriers [134]. The fixed τ curves were fitted simultaneously with the Drude model incorporated into the optical model. The simultaneous iterative best-fitting procedure reveals the values of the plasma frequency $\omega_p = 1.2^{+0.3}_{-0.2} \times 10^{15} s^{-1}$ and damping rate $\Gamma = 2^{+1.2}_{-1} \times 10^{15} s^{-1}$.

Although we do expect some dependence of the plasma frequency and scattering rate, this type of measurement is not sensitive enough to resolve such a trend. The weak dependence of these parameters on incidence angle is confirmed by calculations; Fig. 4.8 shows that the absorbed energy is only weakly dependent on angle due to multiple reflections in the multilayer structure of the sample. Calculation of the absorption coefficient is performed through use of an optical model, using Fresnel formulae and the optical functions of the layers, predicting a change of $A = 0.025 \rightarrow 0.04$ over the incidence angles measured. Although this predicts a higher plasma frequency for larger angles this dependence is masked by experimental error.

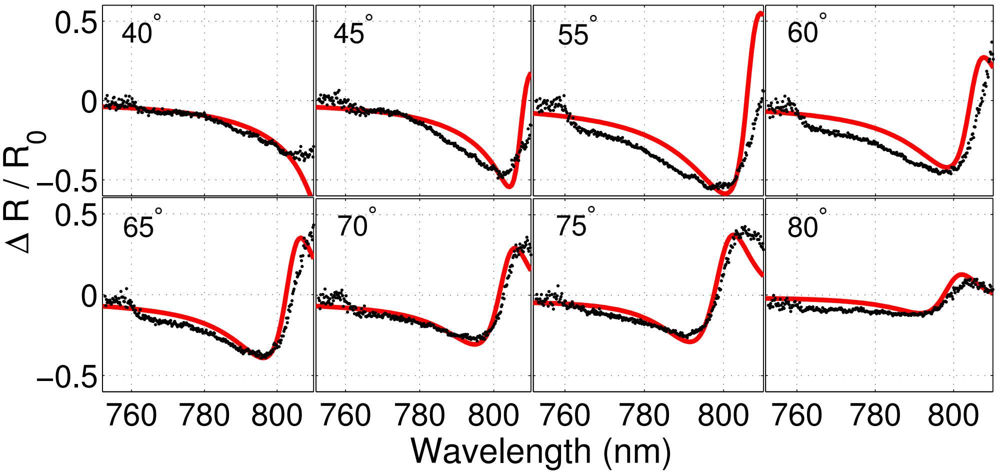

Figure 4.7: Transient change in reflectivity recorded at different incidence angles between 40°-80°. Black dots depict the reflectivity change, $\Delta R/R_0$, extracted from the measurements shown in Fig. 4.6. Red solid line represents the Drude model fitting.

Comparison of the values of ω_p and Γ to those published in the literature for bulk silicon and embedded *nc-Si* lead to some interesting postulations. Sokolowski-Tinten et. al. [34] estimated a scattering frequency $\Gamma = 9.9 \times 10^{14}\mathrm{s}^{-1}$, which they attribute to carrier-carrier scattering, although these measurements are at a plasma frequency an order of magnitude greater than ours. Sabbah *et. al.* [32] estimate $\Gamma = 1.25 \times 10^{13}\mathrm{s}^{-1}$ at plasma frequencies well below the one in this study. It is important to note here that the measurements performed are for single angle of incidence measurements. A number of works using Terahertz pulses have recently been published [43, 44], which propose scattering rates in the region $\Gamma = 3 \times 10^{13}\mathrm{s}^{-1}$-$\Gamma = 1.25 \times 10^{14}\mathrm{s}^{-1}$ at nearly the same plasma frequencies used here. It is however important to note that due to the dependence of the scattering rate on the probing frequency these values should be considered carefully [44]. All of these studies, summarised in Tab. 4.2, despite proposing quite different scattering rates, agree that the scattering process is governed by carrier-carrier interactions. It is apparent from our studies that in this sample of *nc-Si:H* the scattering rate is an order of magnitude faster than previously reported.

In order to understand these differences it is useful to know the effective mass of the carriers, this allows one to calculate the carrier density N_{eh} from the plasma frequency, ω_p. The effective mass of the carriers can be calculated by measuring the reflectivity

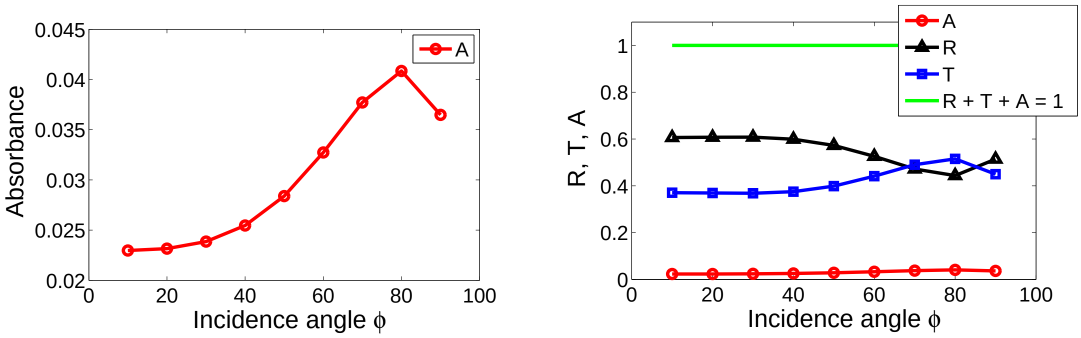

(a) (b)

Figure 4.8: (a) Change in the absorbance of *nc-Si:H* as a function of incidence angle, calculated using Fresnel formulae for multiple reflections and utilising the dielectric function dispersions of each layer from ellipsometry measurements. (b) Change in reflectance (black triangles), transmission (blue squares) and absorbance (red circles) as a function of incidence angle again calculated as in (a).

change $\Delta R(\lambda, \tau)/R_0$, for a fixed angle of $\phi_i = 70°$, as a function of the pumping fluence, F, between 0.14 and 2.3mJ/cm^2. The results from this measurement are shown in Fig. 4.9. In a manner akin to that of measurements with varying incidence angle, there is an observed Fabry-Perot fringe toward the red side of the spectrum. The data were analysed by fitting with the same Drude approximation as in the previous measurement, fitting as a function of wavelength for a fixed probe delay of ~350fs. Fig. 4.10 shows the fixed τ measurements and are in reasonable agreement with those seen in Fig. 4.7. The plasma frequencies retrieved from this measurement are plotted as a function of the pumping fluence in Fig. 4.11. The dependence of the graph is seen to be linear, however the y-intercept does not correspond to the plasma frequency in absence of the optical pump, but rather the detection limit of the apparatus used. The slope of the graph was found by a linear fit to be $\Delta = 6.1 \times 10^{29}$cm^2/mJs^2, which was used to estimate the reduced optical mass from,

$$\omega_p^2 = \frac{1}{m}\frac{AF}{d}\frac{e^2}{\hbar\omega\varepsilon_0 m_e} = \Delta F, \tag{4.2}$$

where A = 0.4 is the absorbance calculated from the optical model (including the effect of free carrier absorption within the sample) at a delay time of 350fs and d is the thickness of the *nc-Si:H* layer. The optical mass of the carriers estimated was found to be $m_{\text{eff}} = 0.17^{+0.05}_{-0.03}$. The value measured here is close to that found in samples of bulk

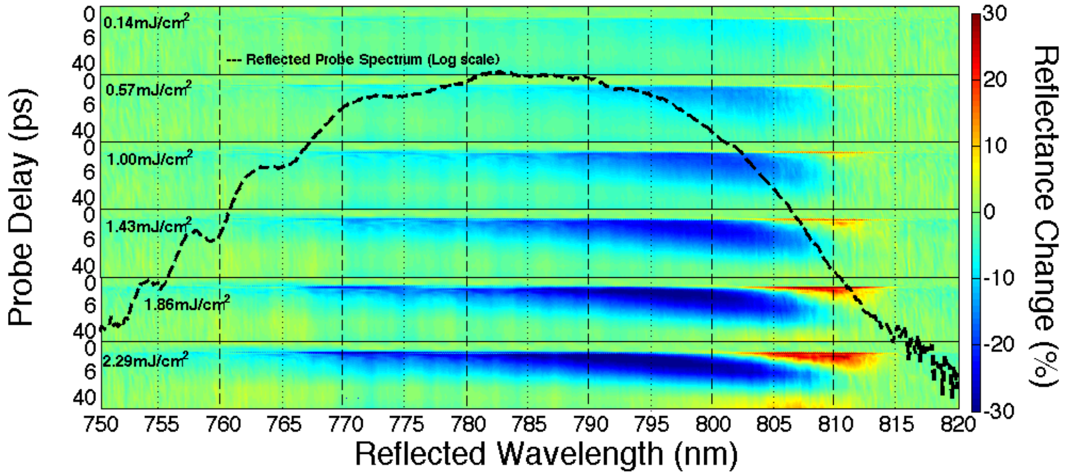

Figure 4.9: Transient change in reflectivity plotted for a range of pump fluences between 0.14-2.3mJ/cm^2. The change in reflectivity $\Delta R/R_0$ are plotted as a function of probe delay and probing wavelength. An overlay of the probe spectrum is plotted (dashed line) on a logarithmic scale. [103]

silicon from other time-resolved reflectivity measurements [32, 34] ($m_{Si} = 0.15$) corresponding to the band edge reduced optical mass. This requires that non-parabolicity effects can be discounted [132]. Using the effective mass of the carriers it was then possible to deduce the carrier density N_{eh} (plotted on the right axis of Fig. 4.11).

The value of the carrier concentration here is an average value over the size of the beam spot. In measurements of scattering outlined in section 4.2 we have proven that at the probe delay here the majority of carriers are localised within the silicon nanocrystals, thus the true concentration can be greater by a factor of $1/f$, where $f = 0.35$ is the fractional volume of the nanocrystals in the layer. Knowledge of the effective mass of the carriers and the carrier concentration allows the mean free path of the carriers to be calculated. For an ambipolar electron-hole plasma this is given classically by, $l = v_f/\Gamma$, where v_f is the Fermi velocity. For the data shown in Fig. 4.7 the mean free path is $l \sim 0.3$nm. This value, unusually short compared to similar measurements in these types of materials, leads to important conclusions about the carrier interactions. Firstly, that the carrier is confined within the crystallites, as scattering restricts its escape from the excitation volume. Second, that the carrier is self-confined and finally, that the carriers mutual interaction is strong. It can also be deduced that scattering from

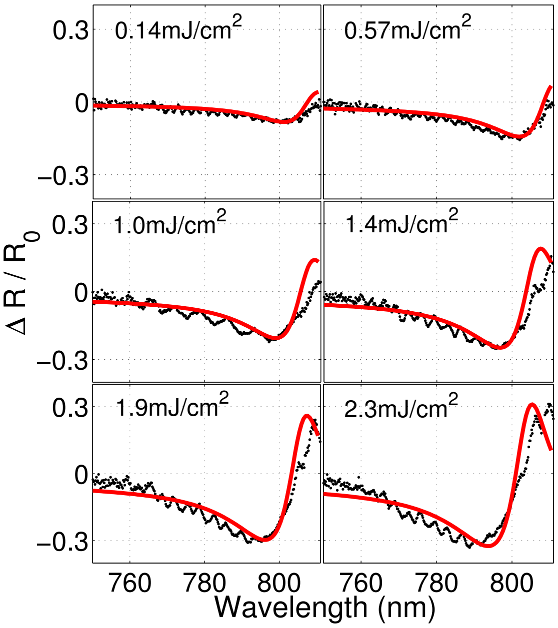

Figure 4.10: Transient change in reflectivity recorded at various pump fluences between 0.14-2.3mJ/cm^2. Black dots depict the reflectivity change, $\Delta R/R_0$, extracted from the measurements shown in Fig. 4.9. Red solid line represents the Drude model fitting.

the nanocrystalline boundaries does not contribute as their length scale is an order of magnitude larger. We also note that scattering from defects and from phonons can be discounted as the scattering rate measured is too fast to fit these mechanisms [139]. It is therefore reasonable to assume that carrier-carrier processes are responsible for this fast scattering rate.

This assumption requires some elaboration. Calculation of the average distance between carriers r_0 can be found from the carrier concentration within each of the nanocrystals 2.9×10^{20}cm^3, providing $r_0 = (3/4N)^{1/3} = 1.3nm$. Conversely, the scattering rate provides a distance, $r_s = (Nl)^{-1/2} = 3$nm, greater than the average distance between the carriers, suggesting a strong carrier-carrier interaction. In accordance with Fermi-liquid theory [139] the interaction length scales with temperature as $(k_bT/E_f)^2$. Under the experimental conditions here, this factor approaches unity at $T = 10^4$K. Corresponding to the temperature at which the coulomb screening is zero and limitation due to Pauli exclusion principle is ineffective. The extremely high temperature of the electronic sub-system that this requires is not out of reach of the carrier concentration

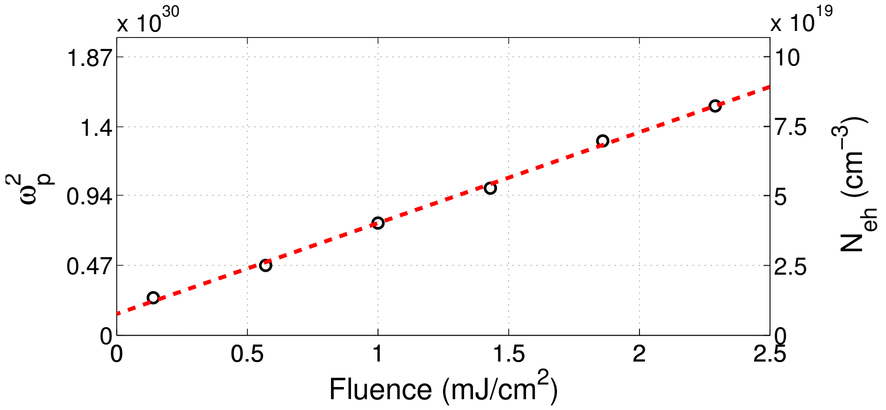

Figure 4.11: LHS y-axis: Plasma frequency ω_p calculated through Drude model fitting of data in Fig. 4.9 as a function of pump fluence. RHS y-axis: Carrier concentration N_{eh} calculated from values of plasma frequency using effective mass of carriers approximated using Eq. 4.2.

found here [132]. For a classical gas of electrons at the Fermi temperature the screening radius can be approximated [140] by $(\varepsilon_0 k_b T/Ne^2)^{1/2}$ providing an estimate of 1.7 nm, this supports the argument of strong interactions between hot carriers. Another factor that can lead to this high scattering rate is that of spatial confinement [141], known to increase the strength of the Coulomb interaction. A similar influence is expected to effect scattering, not yet explored in depth in the literature [103].

Table 4.2: Summary of calculated carrier concentrations N_{eh} and scattering times Γ for samples of *nc-Si:H* measured using a variety of techniques.

Study	ω_p	N_{eh}	Γ
NPRL (800nm) [103]	$1.25 \times 10^{15}\text{s}^{-1}$	$2.9 \times 10^{20}\text{cm}^{-3}$	$2 \times 10^{15}\text{s}^{-1}$
Sokolowski (625nm) [34]	...	$\sim 10^{22}\text{cm}^{-3}$	$9.9 \times 10^{14}\text{s}^{-1}$
Sabbah (800nm) [32]	...	$5 \times 10^{18}\text{cm}^{-3}$	$1.25 \times 10^{13}\text{s}^{-1}$
Cooke (THz) [43]	...	$3 \times 10^{18}\text{cm}^{-3}$	$3 \times 10^{13}\text{s}^{-1}$
Shimakawa (THz) [44]	...	$6 \times 10^{19}\text{cm}^{-3}$	$1.25 \times 10^{14}\text{s}^{-1}$

4.4 Ellipsometry

4.4.1 Nano-crystalline Silicon *nc-Si:H*

The discussion and results in this section are based on the paper: **Electron dynamics in hydrogenated nano-crystalline silicon studied by time-resolved ellipsometry, Unpublished (2012)**

Measurements of time-resolved ellipsometry have been performed as described in section 3.2.2. A novel pump-probe rotating compensator ellipsometer (RCE) has been used, described in detail here [99]. The ellipsometer utilises a polariser prior to the sample, in oder to set the polarisation axis of the incident light to $P = 45^\circ$. The sample is set to an incidence angle of $\phi_i = 65^\circ$, corresponding closely to the samples Brewster angle. Following the sample the ellipsometer uses a rotating compensator positioned in a mechanical rotation mount, which is capable of 0-360° rotation and an analyser (Glan-Thompson polariser) set to an angle of $A = 0^\circ$. The light from the ellipsometer $I_d(\lambda,\tau)$ is detected via a spectrometer (Ocean Optics USB2000+ VIS-NIR). Analysis of the detected intensity $I_d(\lambda,\tau)$ is performed using a standard Fourier series equation, given by Eq. 3.48 [142, 143]. The parameters resolved $\Psi(\lambda,\tau)$, $\Delta(\lambda,\tau)$ represent the change in amplitude and phase of the light following the sample. The RCE, positioned in the probe arm of the apparatus, was calibrated and compared to measurements made on the same sample of *nc-Si:H* using a commercial ellipsometer. Fig. 4.12 shows that the two ellipsometers (home-built RCE and Horiba Jobin-Yvon) are in very good agreement for both of the ellipsometric parameters Ψ & Δ.

By varying the probe delay (τ) the ellipsometric parameters are resolved as a function of time over the first 25ps following optical excitation. The relative changes in the ellipsometric parameters $\delta\Psi/\Psi_0$ and $\delta\Delta/\Delta_0$ are plotted as a function of wavelength in Fig. 4.13(a) & 4.13(b). Although these measurements provide some idea of the time-scales involved upon excitation of the sample it is not clear what processes are responsible. To gain a better insight into these processes we must convert the ellipsometric parameters to a change in dielectric function of the sample. For the particu-

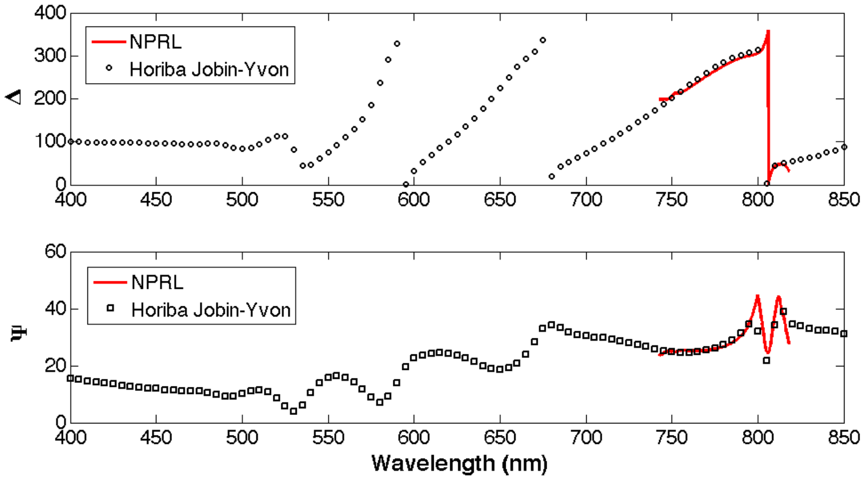

Figure 4.12: Ellipsometric angles Ψ & Δ measured with commercial ellipsometer (Horiba Jobin-Yvon) [open symbols] and compared with measurements made with home-built ellipsometer (without optical pumping) [solid line].

lar sample used here we propose (as in the previous section) that the *nc-Si:H* layer is solely responsible for the changes seen in the amplitude and phase of the light following light reflection. An optical model utilising a transfer matrix formulation and based on measurements of scanning electron microscopy (SEM), x-ray diffraction (XRD) and micro-Raman analysis was used to model the optical parameters of the sample prior to excitation with the pump pulse ($\tau < \tau_0$). For probe delays following excitation the model should be adapted to correspond to the values of the ellipsometric parameters at $\tau > \tau_0$.

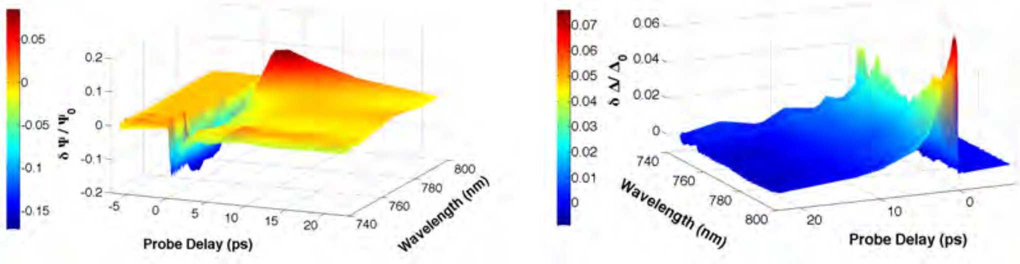

(a) (b)

Figure 4.13: (a) Transient change in ellipsometric angle $\delta\Psi/\Psi_0$ plotted as a function of probing wavelength and probe delay. (b) Transient change in ellipsometric angle $\delta\Delta/\Delta_0$ plotted as a function of probing wavelength and probe delay.

Fitting of the time-resolved ellipsometry data is achieved via two methods (shown in Fig. 4.14), the first finds the complex dielectric function ($\varepsilon_{nc-Si} = \varepsilon'_{nc-Si} - i\varepsilon_{nc-Si}''$) by varying each component (real and imaginary) independently in order to best fit the values of $\Psi(\lambda,\tau)$ and $\Delta(\lambda,\tau)$. The second method uses a Drude model approximation, which describes the contribution of free carriers excited in the conduction band to the dielectric function. The unperturbed dielectric function ($\varepsilon_0 = \varepsilon'_0 - i\varepsilon_0''$) for each wavelength is modified by adding a contribution depending on the probe delay, such that using the Drude approximation the dielectric function at each probe delay is given by,

$$\varepsilon(\tau) = \varepsilon_0 + \varepsilon_d(\tau) \tag{4.3}$$

where ε_d is given by the Drude model in equation 3.92. Combination of Eqs. 4.3 & 3.92 provide the Drude parameters ω_p and Γ. Fig. 4.14 (a, b) shows values of the ellipsometric parameters averaged over all probing wavelengths, (c, d) the dielectric functions of the *nc-Si:H* layer and (e, f) the Drude parameters. The change in dielectric function described by the Drude model approach is in good agreement with those found by the 'brute force' method described above.

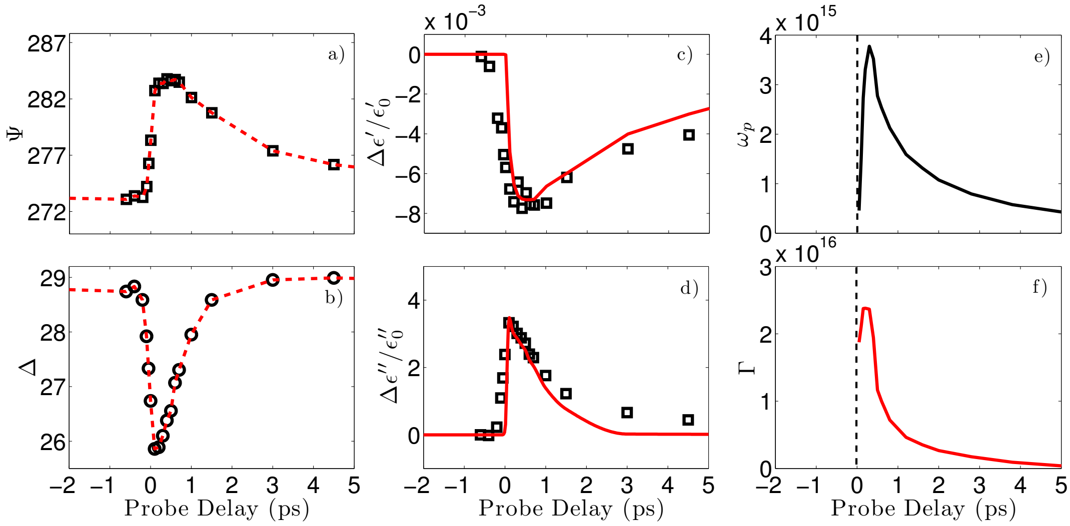

Figure 4.14: (a)-(b) Change in ellipsometric angles, Ψ and Δ, averaged over all probing wavelengths as a function of probe delay over the first 5ps following excitation. (c)-(d) Change in the dielectric function $\Delta\varepsilon'/\varepsilon'_0$ & $\Delta\varepsilon''/\varepsilon''_0$ found from 'brute' force fitting of the functions (symbols) and through Drude model approximation (solid) line. (e)-(f) change in the Drude model parameters ω_p & Γ.

A distinct positive change in the imaginary part of the dielectric function and a much smaller negative change in the real part are measured, corresponding well with other measurements on these types of silicon materials [39, 44, 144]. The change in absorption exhibits a characteristic time scale of ∼4ps, in which time the change has reached almost zero. However, the change in the real component persists for much longer, proceeding over tens of picoseconds, this can be seen in Appendix C. The timescales and mechanisms responsible have been discussed using scattering measurements (Sec. 3.2.4). Measurements of the Drude parameters reveal more interesting features of the time-scales and mechanisms involved in carrier excitation, transport and relaxation after optical excitation. As described in the previous section, the effective mass of the carriers can be estimated through pump fluence dependent measurements of reflectivity change in conjunction with Drude modelling of the system. Using the effective mass $m_{\text{eff}} = 0.17$ we are able to resolve the carrier concentration N_{eh} as a function of time. Fig. 4.15 plots the carrier concentration against probe delay.

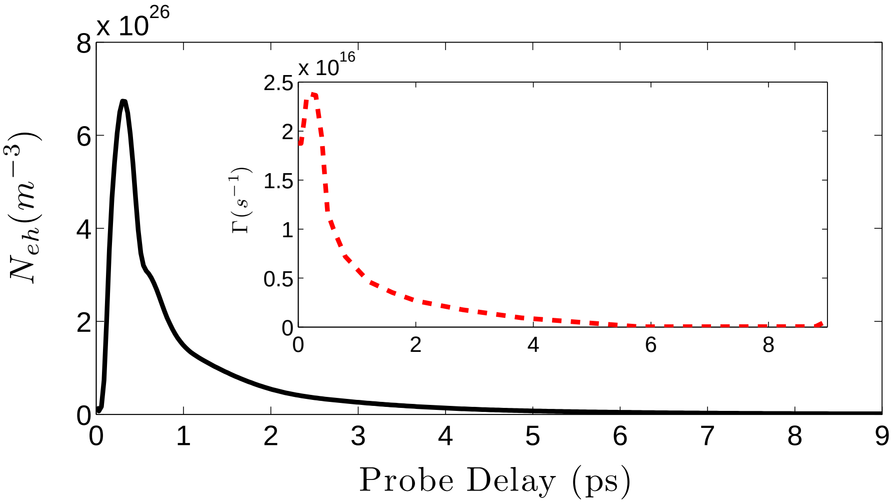

Figure 4.15: Transient change in carrier concentration N_{eh} as a function of probe delay. Inset: corresponding change in scattering frequency Γ.

The graph shows a relatively high peak carrier concentration of $\sim 7 \times 10^{20}\text{cm}^{-3}$, although consistent with concentrations estimated in other works [19, 34], this provides an insight into the mechanism of excitation. We see that the carriers are excited on roughly the same timescale as the pulse duration ∼80fs. Given the assumption that carriers are excited linearly according to the equation,

$$N = \frac{AF}{\hbar\omega}, \tag{4.4}$$

where A is the absorbance of the sample, F is the pumping fluence and ω is the pump frequency. This equation provides an estimate of $N_{\text{est}} \sim 10^{18}\text{cm}^{-3}$, well below the carrier concentration measured here. This high carrier concentration can be due to nonlinear absorption of carriers [50], although nonlinear dependency of carrier concentration was not measured as a function of the pumping fluence. Alternatively the absorption coefficient of the sample may be altered during the time in which the pump pulse is still 'on'. The mechanism of excitation here is complicated and has not been studied in depth. Electrons are expected to be far from equilibrium and as such do not behave in a straightforward manner. The precise mechanism by which excitation occurs should be studied in more detail as a function of both probing energy E_p and pump fluence F.

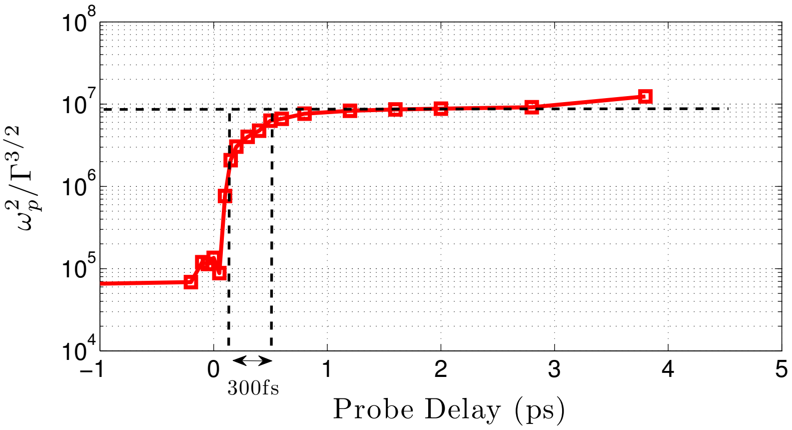

Figure 4.16: Fraction $\omega_p^2/\Gamma^{3/2}$ as a function of probe delay over the first ~5ps after optical excitation. The fraction yields a constant for electron-electron (-like) interactions. After ~300fs the fraction has reached a constant level and we assume that carrier-carrier interactions are the dominant process at this time-scale. For later probe delays thermal processes (not modelled by the Drude approximation) start to play a significant role and accuracy is lost.

Following excitation we expect the electrons to reach equilibrium within ~0.3ps [13]. This timescale seems to be set by the time in which the pump and probe are still strongly interacting with each other. After this time it is possible to infer some interesting behaviour of the carriers. The first thing to note is the method by which the carriers interact, either through carrier-carrier scattering, carrier-phonon interactions, scattering from boundaries or from defect states etc. To understand which of these is responsible the length scales of the scattering process should be understood. This can be achieved for carrier-carrier interactions by considering the fraction $\omega_p^2/\Gamma^{3/2}$. This fraction provides a constant for $e-e$ scattering which assumes $\omega_p^2 \propto N_{eh}$ and $\Gamma = v_f/l \propto N_{eh}^{2/3}$. Fig. 4.16 shows the dependence of this fraction as a function of the probe delay. It can be seen that immediately after optical excitation $\tau = 0$ there is a sharp rise indicating that the electrons are out of equilibrium or some other process is responsible for the scattering seen at these times. After approximately 300fs there is a flattening of the graph suggesting that the major scattering contribution is from carrier-carrier interactions. This trend persists for a further ~3.5ps, corresponding to the point at which the scattering rate, calculated using the Drude model, has become very small and accuracy in both parameters (ω_p & Γ) are lost. We expect that after this time thermal effects due to phonon interactions start to play a role and masks the carrier-carrier contribution. Othonos *et. al.* [12] claim that phonon processes become effective between 4-15ps in semiconductors, corresponding well to the times measured here. An in depth look at the processes, rates and concentrations measured within the timescale 0.3-5ps will be studied in the following sections (Sec.4.5 & 4.6)

4.4.2 Silicon Nitride SiN_x

In order to corroborate the measurements made on samples of *nc-Si:H* we have also looked at a sample of silicon nitride, SiN_x. We begin, as before, by looking at the reflectivity from the sample as a function of the probe delay. This provides a convenient measure of the strength of the response within the sample to optical pumping, as well as providing a quick method to optimise the overlap of the pump and probe (by scanning the probe over the pump spot until a maximum $\Delta R/R_0$ is measured). The apparatus to measure the sample are the same as those described in section 3.1. The measured transient reflectivity change $\Delta R(\tau)/R_0$ exhibits a small negative change in reflectance of about 2% (see Fig. 4.17). The reflectivity change seen here is much smaller than that observed in the previous sample, being almost at the level of noise ($\sim 1\%$). We see that the reflectivity reaches zero after 2.5ps, however, as we see later, this corresponds to the point at which the change in reflectivity of the sample is no longer visible, due to the low SNR, not the point at which there is no change due to the dielectric function.

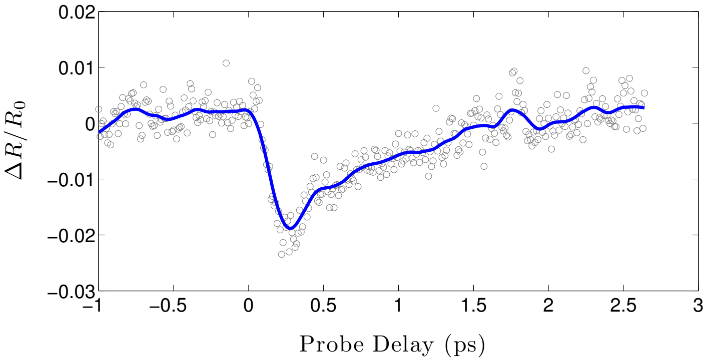

Figure 4.17: Transient change in reflectivity $\Delta R/R_0$ measured in a sample of SiN_x as a function of probe delay, experimental data (symbols) and smoothed data (solid line).

To understand the processes occurring in this sample, time-resolved ellipsometry measurements have been taken. Figs. 4.18(a) & 4.18(b) show the change in amplitude $\delta\Psi/\Psi_0$ and phase $\delta\Delta/\Delta_0$ imparted by the sample on the incident probe pulse following excitation with the pump. The change in the ellipsometric parameters are plotted as a function of probing wavelength, it can be seen that for longer wavelengths there is a greater percentage change in the values. We also note that although the reflectivity change appeared to be zero for probe delays after 2.5ps, in fact the change in the dielectric function which imparts an amplitude and phase shift to the incident light is still present. To further illustrate this point the averaged values of the ellipsometric parameters are plotted in Fig. C.5 in Appendix C. Also plotted is the quality of fit for these parameters.

As before an optical model based on measurements of SEM and absorption spectra has been constructed. Iterative fitting of the temporal ellipsometric parameters using a Drude model approximation provides the dielectric function of the SiN_x layer, we assume here that the silicon substrate does not play a role in the dielectric function change

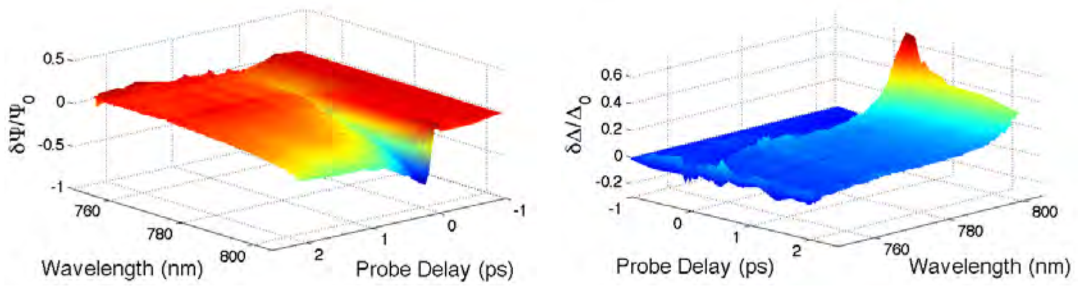

(a) (b)

Figure 4.18: (a) Transient change in ellipsometric angle $\delta\Psi/\Psi_0$ plotted as a function of probing wavelength and probe delay. (b) Transient change in ellipsometric angle $\delta\Delta/\Delta_0$ plotted as a function of probing wavelength and probe delay.

as we have not been able to measure any signal from this material at the pump fluences and probing energies used in this study. Fig.4.19 (a, b) shows the change of the dielectric function ($\Delta\varepsilon'/\varepsilon_0'$, $\Delta\varepsilon''/\varepsilon_0''$), which exhibits the same qualitative changes seen in the sample of *nc-Si:H*. A large increase in the imaginary component of the dielectric function (∝absorption coefficient) is seen along with a much smaller decrease in the real part. The extracted Drude parameters are plotted in Fig.4.19 (c, d) showing an increase in both the plasma frequency ω_p and scattering frequency Γ. The scattering rate measured also reaches approximately the same level as that seen in *nc-Si:H*.

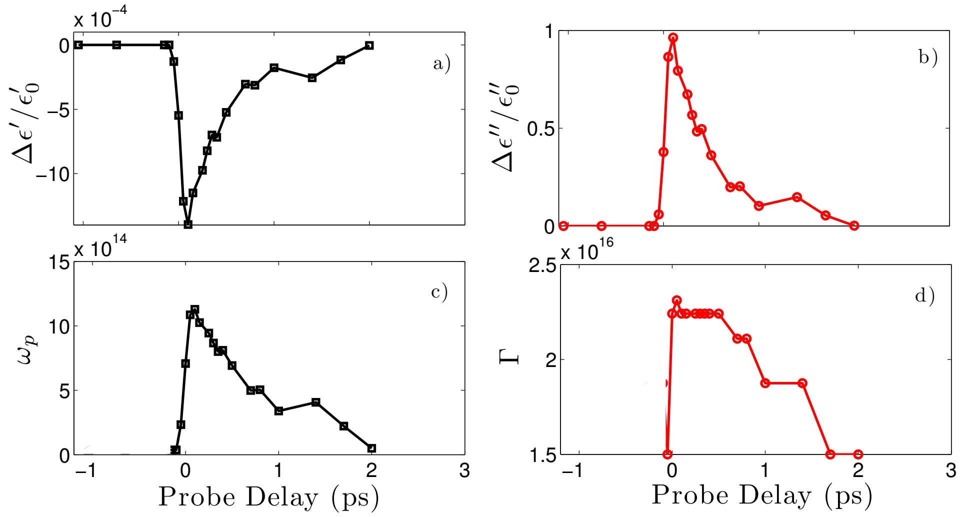

Figure 4.19: (a)-(b) Transient change in dielectric function of *SiN*$_x$ sample $\Delta\varepsilon'/\varepsilon_0'$ & $\Delta\varepsilon''/\varepsilon_0''$, found via fitting of the Drude model. (c)-(d) Calculated Drude parameters over the first few picoseconds.

The mechanism by which the carriers scatter can be checked by looking at the fraction $\omega_p^2/\Gamma^{3/2}$ as described in section 3.2.2. This fraction is plotted as a function of the probe delay τ and would show a constant for carrier-carrier interactions for the reasons described previously. Fig. 4.20(a) shows this fraction with probe delay, however no levelling of the graph is seen for the data measured. This implies that carrier-carrier scattering may not be responsible. An alternative mechanism for the scattering process to proceed is that of collisions with defects. In order to test this theory one can look to see if the collision length $L = v_f/\Gamma$ is constant with the probe delay, suggesting that no matter how many carriers are excited and/or subsequently decay the scattering length is fixed i.e. likely to be from a boundary which does not change with time. Fig. 4.20(b) shows a plot of the collision length L with probe delay, the 'flattening' of the graph immediately after excitation of the carriers ($\tau = 0$) suggests that the dominant process in this sample could indeed be collisions with fixed boundaries or defects. There is still some slight dependence with probe delay suggesting that although collisions with defects dominates the scattering, other processes cannot be disregarded completely. The collision length measured is retrieved using the fermi velocity $v_f = (\hbar/m)(3\pi^2 N_{eh})^{1/3}$ and the scattering rate Γ, $L = v_f/\Gamma$. Where the carrier concentration is found from Eq. 3.93 using an effective mass for carriers in silicon nitride samples of $m_{\text{eff}} = 0.4$ [145]. The collision length is found to be $L \approx 1\dot{A}$, which points toward scattering from defects and impurities in the sample, typical for these types of SiN_x materials [38]. However so far the data in inconclusive.

4.5 Solving the Fermi integrals

As we have seen in section 4.4 the scattering process in *nc-Si:H* is governed by electron-electron interactions. To make sense of the scattering rate observed it is important to understand the electron (and hole) distribution within the conduction band (valence band). Dependent on whether the electron interactions obey quantum or classical laws, the scattering rate obeys quite different dependence with carrier concentration [15, 37]. To get an idea of the regime that the system is operating under, we can model a Fermi-Dirac distribution of electrons for a parabolic conduction/valence band. Given that the system has a finite, non-zero temperature, the excited states of the N-electron system

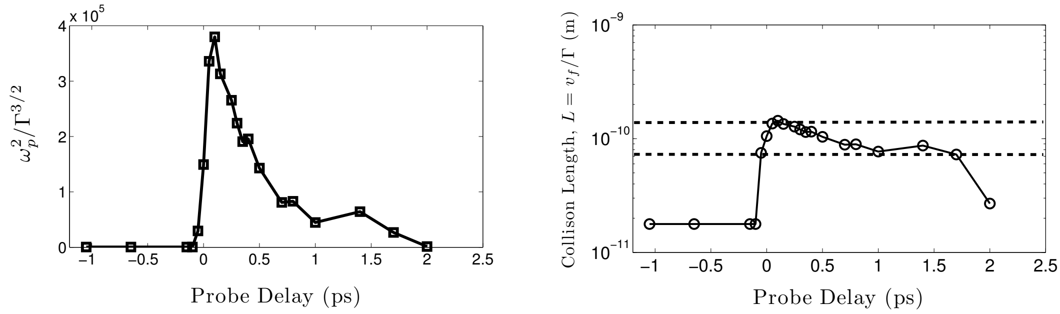

(a)

(b)

Figure 4.20: (a) Fraction $\omega_p^2/\Gamma^{3/2}$ as a function of probe delay, no flattening of the graph is seen suggesting that carrier-carrier collisions are not the dominant process in this material. (b) Collision length, $L = v_f/\Gamma$ as a function of probe delay, The graph is relatively flat over the experimental region suggesting that collisions with fixed boundaries dominate the scattering process.

should be modelled using statistical mechanics (see Appendix E). The total internal energy of the system is given by,

$$u = \int \frac{d\vec{k}}{4\pi^3} \varepsilon(\vec{k}) f(\varepsilon(\vec{k})), \tag{4.5}$$

Similarly the electron density by,

$$n = \int \frac{d\vec{k}}{4\pi^3} f(\varepsilon(\vec{k})). \tag{4.6}$$

Integrals of these types can be converted into spherical coordinates to retrieve the carrier concentration,

$$n = \int_{-\infty}^{\infty} d\varepsilon g(\varepsilon) f(\varepsilon) = \frac{(m)^{3/2}}{\sqrt{2}\pi^2\hbar^3} \int_{-\infty}^{\infty} d\varepsilon \frac{\varepsilon^{1/2}}{\exp((\varepsilon-\mu)/k_bT)+1}, \tag{4.7}$$

where $g(\varepsilon) = \frac{m}{\hbar^2\pi^2}\sqrt{\frac{2m\varepsilon}{\hbar^2}}$ is the density of states such that $g(\varepsilon)d\varepsilon = (1/V) \times$ the number of 1-electron energy levels. For the moment we will neglect the slightly different contribution for holes. We may also write down the energy for the system as (see Eq. 4.5),

$$
\begin{aligned}
u = \frac{(\hbar\omega - E_g)}{2} n = \int_{-\infty}^{\infty} d\varepsilon g(\varepsilon) f(\varepsilon) \varepsilon \\
= \frac{(m)^{3/2}}{\sqrt{2}\pi^2\hbar^3} \int_{-\infty}^{\infty} d\varepsilon \frac{\varepsilon^{3/2}}{\exp((\varepsilon - \mu)/k_b T) + 1},
\end{aligned}
\tag{4.8}
$$

where ω is the pump frequency and E_g is the band gap of the sample and we have taken all the non energy-dependent parameters outside of the integral. The term $(\hbar\omega - E_g)/2$ is known as the excess energy Δ. From the experiments performed previously it is possible to solve these equations to find the temperature T and chemical potential μ. Certain assumptions should be made in order for this to be true,

1. The set of equations is only valid for times much shorter than the electron-hole recombination time. This means that the number of electrons and holes are the same and energy is exchanged between them to achieve equilibrium.

2. The temperature of electrons and holes are the same.

The set of equations (4.7 & 4.8) can only be solved analytically for the classical ($T_n \ll T$) and quantum regimes ($T_n \gg T$), where T_n is the fermi temperature and is defined by,

$$
T_n = \frac{\hbar^2}{2m}(3\pi n)^{2/3}. \tag{4.9}
$$

However, as we know, the carrier concentration and the excess energy Δ through experimentation, we are able to solve this problem numerically.

To do this we should first re-scale the parameters to reduce the complexity of the calculation. We do this via the transformations: $\beta = 1/k_b T$, $x = \beta\varepsilon$, $y = \beta\mu$, $\tilde{\beta} = \hbar\omega\beta$ and $\tilde{n} = n/C(\hbar\omega)^{3/2}$, where $C = (2m)^{3/2}/2\pi^2\hbar^3$.

$$
f_1 = \tilde{\beta}^{-3/2} \int_0^{\infty} dx \frac{x^{1/2}}{\exp(x-y)+1} - \tilde{n}, \tag{4.10}
$$

$$
f_2 = \tilde{\beta}^{-5/2} \int_0^{\infty} dx \frac{x^{3/2}}{\exp(x-y)+1} - (\tilde{n} - \tilde{E}\tilde{n}), \tag{4.11}
$$

where $\tilde{E} = E_g/\hbar\omega$ is the rescaled band gap energy. To solve this new set of equations we can simply iterate,

$$\begin{pmatrix} y \\ \tilde{\beta} \end{pmatrix} = \begin{pmatrix} y \\ \tilde{\beta} \end{pmatrix} - \begin{pmatrix} \partial f_1/\partial y & \partial f_1/\partial \tilde{\beta} \\ \partial f_2/\partial y & \partial f_2/\partial \tilde{\beta} \end{pmatrix}^{-1} \begin{pmatrix} f_1 \\ f_2 \end{pmatrix}. \tag{4.12}$$

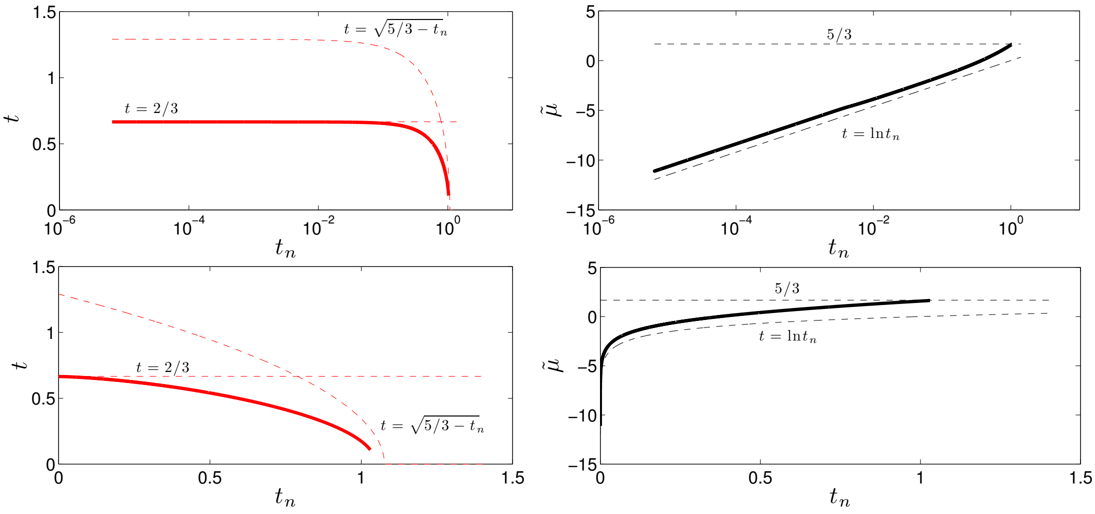

Figure 4.21: Calculated scaled temperature $t = t/\Delta$ and chemical potential $\tilde{\mu} = \mu/\Delta$ against the scaled Fermi temperature t_n, for a simple semiconductor material with parabolic density of states and equal effective mass for electrons and holes $m_e = m_h$ (solid lines). Dotted lines represented the asymptotic limits of the functions for high and low carrier density (quantum and classical limits respectively).

Figure 4.21 shows the solution to these equations, solved numerically through equation 4.12. The asymptotes are calculated for the low and high density limits such that the scaled temperature $t = (k_b)T/\Delta$ and chemical potential $\tilde{\mu} = \mu/\Delta$ in the high density and low density limits of $t_n = T_n/\Delta$ are given by,

$$t = \begin{cases} 2/3, & t_n \ll 1 \\ \sqrt{5/3 - t_n}, & \frac{5}{3} - t_n \ll 1 \end{cases} \tag{4.13}$$

and,

$$\tilde{\mu} = \begin{cases} \ln t_n (+\frac{1}{3}\ln\frac{4\pi}{3}), & t_n \ll 1 \\ \sqrt{5/3 - t_n}, & \frac{5}{3} - t_n \ll 1 \end{cases} \tag{4.14}$$

These asymptotes are only valid for a symmetrical system in which the electrons and holes can be modelled with the same DoS and effective mass $m_e = m_h = m_{\text{eff}}$. For a more realistic approach we need to include the separate effective masses for electrons and holes, as well as including the number of degenerate points in the band structure η. To perform this calculation a system of 3 equations; (1) the number of electrons, (2) the number of holes and (3) the total energy of the system. The numerical solution is calculated (as in the symmetric case), for values $\eta_e = 6$, $\eta_h = 2$ [146] and $m_e = 0.26$ and $m_h = 0.32$ [147] and is shown in appendix F. The result is shown in Fig. 4.22, here we see the temperature of the system scaled by the excess energy $\tilde{t}$, and the scaled chemical potentials for both electrons and holes ($\tilde{\mu}_e$, $\tilde{\mu}_h$). The figure also shows the experimental region for probe delays corresponding to $\tau = 0.3ps \rightarrow 5ps$. In this range the electrons and holes should have had time to reach equilibrium and have not had sufficient time to completely recombine. In this region the calculated values of the scaled temperature $\tilde{t}$ and chemical potentials $\tilde{\mu}_{e(h)}$, averaged over the experimental region are found to be,

- $\langle t \rangle$ = 0.61
- $\langle \tilde{\mu}_e \rangle$ = -1.79
- $\langle \tilde{\mu}_h \rangle$ = -1.55

suggesting that we are in a region somewhere between the classical and quantum regimes, starting, for low densities, in the classical regime and moving toward the quantum regime as the electron (hole) concentration increases. To check this result further we assume that we are operating in a purely classical regime and calculate the scattering rate as a function of carrier concentration.

4.6 Rutherford Scattering

To understand the high scattering rate measured through experiment we look at the predicted scattering rate from classical Rutherford scattering. This calculation was first performed for dense plasmas almost 80 years ago [148]. We use this estimation to fit the experimental data for the probe delay region $\tau = 0.3ps \rightarrow 5ps$. First we will discuss

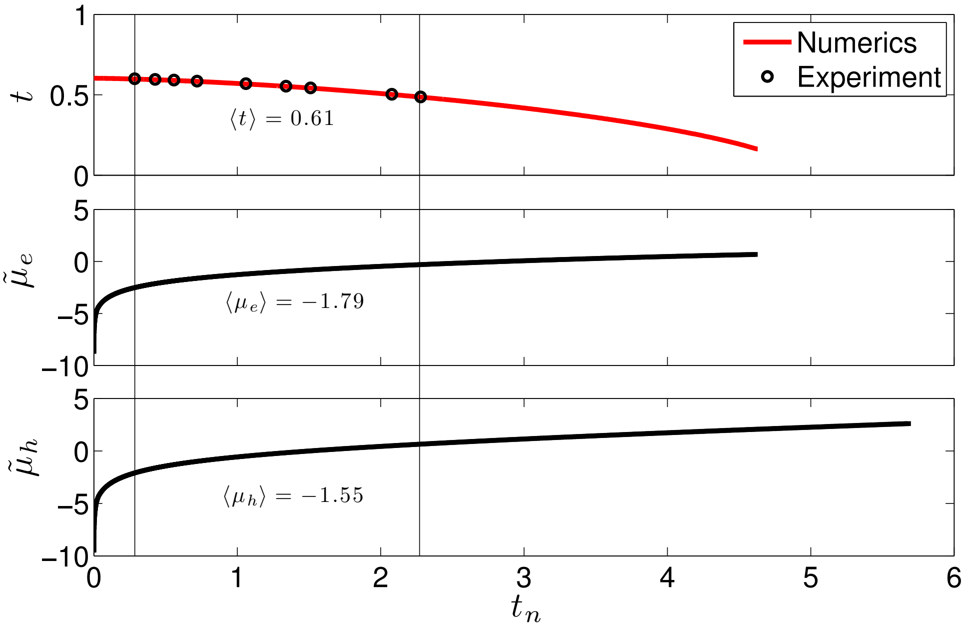

Figure 4.22: Scaled temperature t and chemical potential $\tilde{\mu}$ as a function of scaled Fermi-temperature t_n. The solid lines are calculated for a typical crystalline silicon material with $\eta_e = 6$ equivalent valleys in the conduction band and $\eta_h = 2$ equivalent valleys in the valence band and with effective masses for electrons and holes $m_e = 0.26$ and $m_h = 0.32$ [147]. Symbols represent the range of experimental data shortly following optical excitation (0.3ps - 5ps) and averaged values over this range are presented suggesting that the data is within the classical limit and edging toward the quantum limit.

the assumptions and approximations required for this calculation.

According to Lifshitz [148] a classical non-degenerate plasma can be described using Rutherford scattering. The transport scattering cross-section is found by integrating over all scattering angles χ with a factor of $(1 - \cos\theta)$ to find,

$$\sigma_t = \pi \rho^2 \ln \Lambda, \tag{4.15}$$

The integral is truncated at large and small scattering angles due to it's divergent nature under these conditions. Where, for small angles, there is a cut off due to Debye shielding (see appendix G). The minimum distance between particles, ρ, with velocity v is found by energy conservation, such that,

$$\frac{mv^2}{2} = \frac{e^2}{\rho}, \tag{4.16}$$

and the Coulomb logarithm, $\ln\Lambda$, is a result of truncation of the integral and contains information about screening. Using this information the transport cross-section is therefore,

$$\sigma_t = \frac{4\pi e^4}{m^2 v^4} \ln\Lambda \tag{4.17}$$

Recalling that $nl\sigma_t = 1$ and $l = v\tau$ the scattering rate is given by,

$$\tau^{-1} = \frac{4\pi n e^4}{m^2 v^3} \ln\Lambda \tag{4.18}$$

which can be written using the method outlined in appendix G by,

$$\tau^{-1} = \Gamma = \frac{1}{3\pi^{1/2}} n_e \left(\frac{e^2}{4\pi\varepsilon_0}\right)^2 \frac{4\pi}{m_e^{1/2} T_e^{3/2}} \ln\Lambda. \tag{4.19}$$

Fitting of Eq. 4.19 to the experimental data for our given time range ($\tau = 0.3$ps $\rightarrow$ 5ps) over which the classical equation can be used 'accurately' provides a linear fit whose gradient is a measure of the system temperature. Here we set the Coulomb logarithm, $\ln\Lambda$, to unity, the consequences of this are discussed later. We find through the fitting process an electronic system temperature $(k_b)T_e \simeq 0.3eV$. This value corresponds reasonably to the expected excess energy pumped into the system $\Delta = (\hbar\omega - E_g) = (1.55eV - 1.1eV) = 0.45eV$. This provides some interesting observations about the behaviour of the electron system.

The first point to note is that in the classical limit ($\mu \ll 0$) the distribution of electrons conserves the average temperature $T \sim 0.3eV$ while the chemical potential is reduced to correspond to the decrease in carrier concentration. This suggests that as the concentration of electrons decreases there is no preference for recombination for particles with higher energy. This means that energy per unit volume is decreasing but average energy remains constant. The second point is illustrated by our assumption that the Coulomb logarithm is equal to unity. For the argument (given in Sec. G.1.1) that the

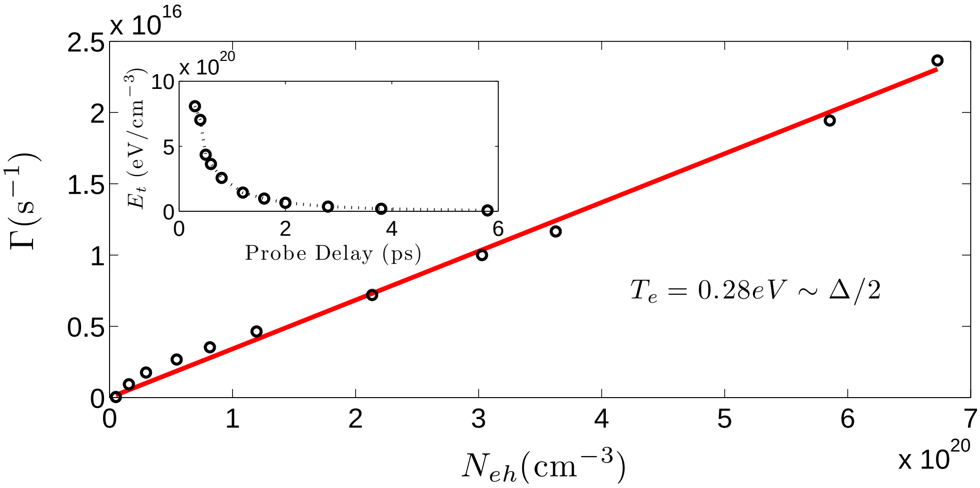

Figure 4.23: Experimentally measured scattering rate Γ against carrier concentration N_{eh} (symbols) provides a linear trend, fitting of Eq. G.22 (solid line) provides the temperature of carriers over the range of probe delays, 0.3-5ps. This suggests that the electron temperature stays the same and no preference is given to recombination of carriers with higher energies. Inset: Total energy within the nc-Si for probe delays between 0.3-5ps.

Coulomb logarithm is divergent for large impact parameter b i.e. for small scattering angles. The Debye screening length, given by,

$$r_D = \sqrt{\frac{T\varepsilon_0}{4\pi n e^2}}, \tag{4.20}$$

is therefore the parameter that controls the Coulomb logarithm to be finite. In this scenario $\Lambda = -\ln\theta_{\min}$, where $\theta_{\min}$ is the minimum possible scattering angle in which scattering is still seen. i.e. smaller angles correspond to larger impact parameters in which Coulomb scattering is not observed. The Debye radius should therefore be larger than the scattering distance for this to be the case. We note that scattering can be a quantum or classical event depending on the minimum distance that particles reach during a scattering event. The product of the minimal distance and the momentum of the particle is given as,

$$mv\rho = \frac{e^2}{2v\varepsilon_0}, \tag{4.21}$$

Scattering is classical, according to the Pauli exclusion principle, if,

$$\frac{e^2}{\hbar v} \gg 1, \tag{4.22}$$

therefore the minimum angle that scattering is possible is given by, $\theta_{\min} = e^2/Tr_D \ll 1$. For quantum scattering,

$$\frac{e^2}{\hbar v} \ll 1, \tag{4.23}$$

the minimum scattering angle is given by, $\theta_{\min} = \frac{\hbar}{mvr_D} \ll 1$. To understand the scattering process occurring in the experiment performed, we can check the fraction,

$$\frac{e^2}{\hbar v} \equiv \sqrt{\frac{E_0}{T}}, \qquad \text{where,} \qquad E_0 = \frac{me^4}{2\hbar^2}. \tag{4.24}$$

In the case presented, where we set the Coulomb logarithm equal to unity, this fraction is large and we should take the logarithm in the classical limit.

$$\text{i.e.} \quad \ln\Lambda = \ln\frac{Tr_D}{e^2}. \tag{4.25}$$

However we find that for the temperature measured ($T \sim 0.3$eV) the Coulomb logarithm is small ($\ln\Lambda \ll 1$). We should now look at the assumptions we have made to come to this point. The parameter which informs us as to which regime we belong is given by Eq. 4.24 and we may re-write this equation as follows,

$$\frac{e^2}{\hbar v} = \frac{v_0}{v} = \sqrt{\frac{E_{\text{ryd}}}{T}}. \tag{4.26}$$

where $E_{\text{ryd}} = 13.6eV$ is the Rydberg energy. This parameter is indeed large for the temperature measured in our experiment (corresponding to $v = 10^8\text{ms}^{-1}$), suggesting that we should use the classical limit of the Coulomb logarithm, given by Eq. 4.25. Now we recall how this was derived. We estimate the scattering cross section to be,

$$\sigma_t = \pi\rho^2 \int d\theta f(\theta)(1-cos\theta), \qquad f(\theta) = \frac{sin\theta}{4\sin^2(\theta/2) + \left(\frac{\rho}{r_D}\right)^2}. \tag{4.27}$$

For the case of no screening $r_D = \infty$ the equation is logarithmically divergent at $\theta = 0$. For $r_D \gg \rho$ we have a finite but logarithmically large value $\ln r_D/\rho \gg 1$ and for a well screened potential $r_D \ll \rho$ there is no special contribution from small angles i.e the whole integral is a constant. We must therefore put $\ln\Lambda = 1$ (see appendix H) in the case that $r_d \ll \rho$. The values retrieved from experiment provide $\rho = 0.62$nm while $r_D = 0.16$nm suggesting that putting the Coulomb logarithm to unity is indeed the correct thing to do.

Chapter 5

Summary & Conclusions

This work has predominantly shown the development and application of a set of novel techniques to study semiconductor materials. This set of techniques is particularly useful when studying opaque semiconductors as there is no need for transmission measurements. All of the measurements utilise femtosecond pulses centred at 800nm with a pulse duration of $\sim$50fs, providing information about the transient nature of the electron dynamics in these types of materials. Of particular interest is the ability to discern carrier dynamics in composite nano-structured materials. The most simple procedure outlined is that of reflectometry, which has been successfully used to measure the plasma frequency and scattering rate in a sample of nano-structured silicon embedded in an amorphous silicon matrix. This was performed using a single fluence multiple-incidence-angle approach [103] to minimise errors and corroborate results. Measurements made, reveal a plasma frequency of $\omega_p = 1.2^{+0.3}_{-0.2} \times 10^{15}\text{s}^{-1}$, similar to measurements of other silicon-based materials under the same conditions [34]. A scattering rate of $\Gamma = 2^{+1.2}_{-1} \times 10^{15}\text{s}^{-1}$ is considerably higher than the majority of works under similar conditions. However it has been shown theoretically that scattering rates as fast as this are indeed expected [149, 150]. Development of this technique by control of the pumping fluence leads to further information about the optical parameters of the material. Plotting the plasma frequency against pumping fluence finds a linear trend, fitting of this trend provides information about the effective mass of carriers. For samples of *nc-Si:H* we find $m_{\text{eff}} = 0.17$, very close to that of bulk *c-Si* (0.15).

The samples of *nc-Si:H* have proven interesting to study for many reasons, not least because the carrier dynamics operate on very different characteristic time scales compared to their bulk counterparts. *Nc-Si:H* has found applications in many areas including photovoltaics, optical switching and microelectronics. For these applications it is crucial to understand how different phases of a composite material (such as *nc-Si:H*) contribute to the overall carrier dynamics. We have developed a pump-probe scattering and reflectivity technique [113] capable of discerning the contribution of embedded spheres from the host matrix. Experiments reveal a fast process of carrier decay within the nano-crystals operating over a few picoseconds, $\tau_{dec} = 2.2 \pm 0.2$ps, while recombination within the host matrix occurs on a much slower timescale, occurring over tens of picoseconds, $\tau_{rec} = 22 \pm 4$ps. We propose that carriers, initially excited within the nano-crystals, are transferred to the matrix within $\tau_{trans} = 4.0 \pm 0.7$ps. These measurements are in reasonable agreement with timescales measured in bulk amorphous silicon and other *nc-Si* samples.

We have further studied samples of *nc-Si:H* and SiN_x using a novel time-resolved rotating compensator ellipsometry apparatus. Although there have been a few attempts at this type of measurement before, they have succumbed to errors with regard to modelling of the materials or assumptions made about the measurement process [14, 151]. We have shown that our home-built ellipsometer is in very good agreement with commercial ellipsometry equipment by comparing measurements made in the absence of optical pumping with those from a Horiba Jobin-Yvon ellipsometer. This is achieved by accurate calibration of all the components of our RCE apparatus (polariser, analyser and compensator). Furthermore we have shown that the optical model created for the multilayer samples of *nc-Si:H* is well defined and in good agreement (for film thickness, composition of multiple phase layers and dielectric function dispersions) with SEM, XRD and μ-Raman analysis of the sample. With a fully resolved ('unperturbed') ellipsometry measurement at hand we have modelled the electron dynamics following excitation under the Drude model approximation. This has revealed the transient changes in plasma frequency and scattering rate over the first few picoseconds, after this time our technique loses accuracy.

The measurements of plasma frequency and scattering rate have been used to show that, for samples of *nc-Si:H*, carrier-carrier scattering seems to be the likely process of carrier interaction. While in samples of SiN_x we have shown that, within the experimental error, the scattering length stays relatively constant, suggesting collisions with defects could be the dominant scattering mechanism. Although these measurements are not conclusive. For samples of *nc-Si:H* we have modelled the carrier dynamics using Fermi integrals. This allows us to ascertain whether the system should assume a classical or quantum electron distribution. This model provides the electron temperature and chemical potential for a parabolic semiconductor material with known energy band gap E_g, optical pumping with energy $\hbar\omega_{eh}$, mass of electrons and holes and number of degenerate points in the band structure, η. It was found that, for the carrier densities measured through ellipsometry, the system should adopt a classical distribution at low carrier densities and moves toward, but does not reach, the quantum regime for the highest carrier densities measured. We therefore assume a classical distribution of carriers is reached following excitation. Using this knowledge we model the scattering dynamics through Rutherford scattering. We find a linear relation between scattering rate and carrier concentration for probe delay times of $0.3 \rightarrow 5$ps. This leads to important conclusions about the electron distribution in this time period. First that the electron temperature is conserved over this time, with the total energy (and therefore chemical potential) decreasing with the carrier concentration. And second, we estimate the minimum distance between scattering particles $\rho = 0.62$nm and the Debye shielding radius $r_D = 0.16$nm, suggesting an unscreened potential for scattering events.

The recombination mechanism of carriers in *nc-Si:H* samples is inconclusive and is left to speculation as to the true nature of this process. Fauchet *et. al.* note that Auger recombination is possible [4], although they do not observe the expected delay between carrier recombination and lattice heating. Similarly we have not (yet) measured the characteristic dependence of recombination rate with carrier concentration. Fauchet also rules out sequential emission of phonons due to the long wavelength of phonons expected and the many intermediate levels in the band structure required for this process. Electron-hole recombination is also possible but has not been directly observed to date. Further work is required to resolve this issue. We also note that it would be interesting to control the electron distribution within the band structure, the experimental parameters required for this are not well understood. Many works have shown that (following excitation) a Fermi-Dirac distribution of electrons is produced within the band structure [12, 133, 150], while we describe a classical electron distribution. Control of the photon energies used and well as the size and shape morphology of the samples could lead to a better understanding of this process. Pump fluence dependency should also be checked to see if Auger recombination processes dominate.

Appendix A

Supplementary Material *nc-Si:H*

A Raman spectroscopy measurement on *nc-Si:H* reveals the fraction of *nc-Si* to α-*Si*. For the samples under study there was found to be $\sim 30\%$ *nc-Si*. X-ray diffraction measurements reveal that the average size of the *nc-Si* grains to be $\langle a \rangle = 6$nm.

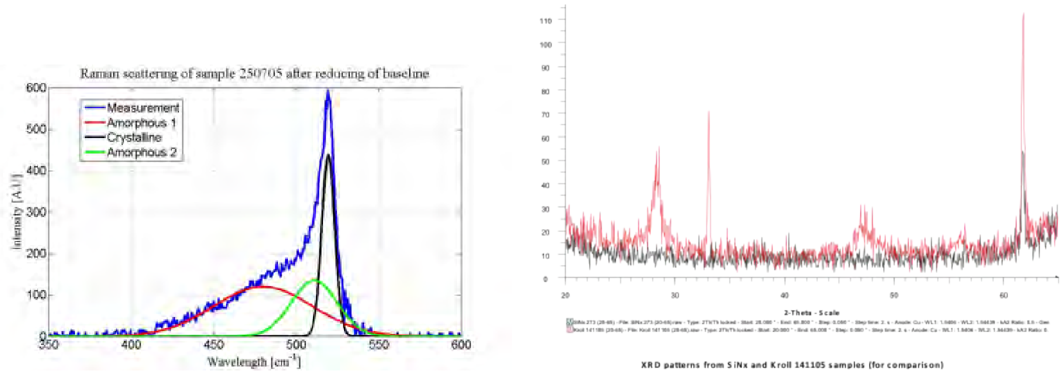

(a) (b)

Figure A.1: (a) A Raman spectroscopy measurement of *nc-Si:H* revealing a 30% fraction of *nc-Si*. (b) X-ray diffraction measurements providing the average size of *nc-Si* grains $\langle 6 \rangle$nm.

Appendix B

Supplementary Material SiN_x

Absorption spectra of SiN_x samples reveals a band gap energy of 2.32eV. Scanning electron microscopy measurements show that the SiN_x layer is $\sim$ 440nm thick. Time resolved photoluminescence measurements reveal the time scales of luminescence for samples of *GaAs* and SiN_x operating on the nanosecond timescale.

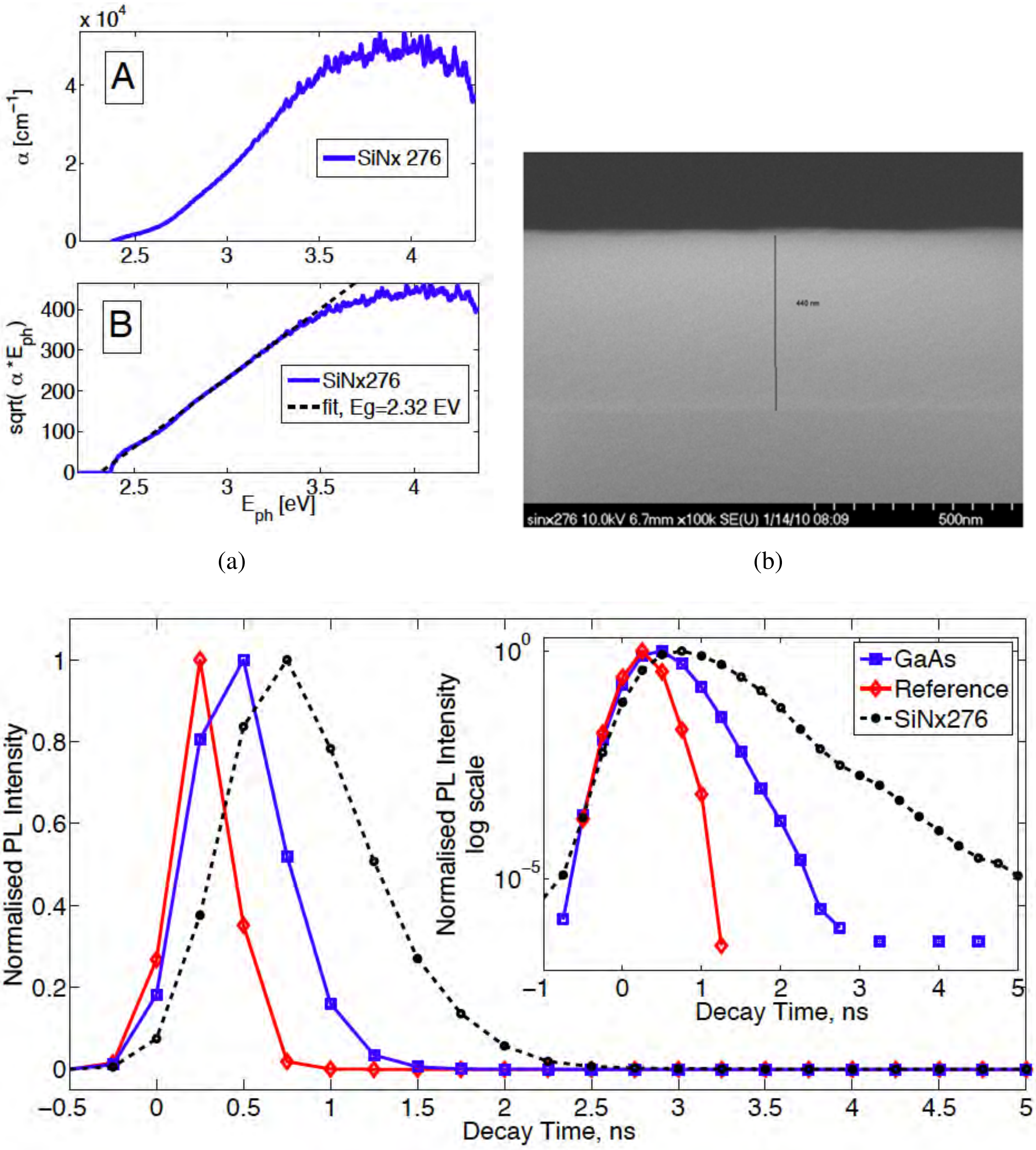

(a) (b)

(c)

Figure B.1: (a) Absorption spectroscopy measurements revealing the band gap energy of SiN_x samples of 2.32eV. (b) SEM measurements provide the SiN_x film layer thickness of $\sim$ 440nm. (c) Time-resolved photoluminescence (TRPL) performed on samples of $GaAs$ and SiN_x revealing characteristic operating timescales in the picosecond region.

Appendix C

Ellipsometry Measurements

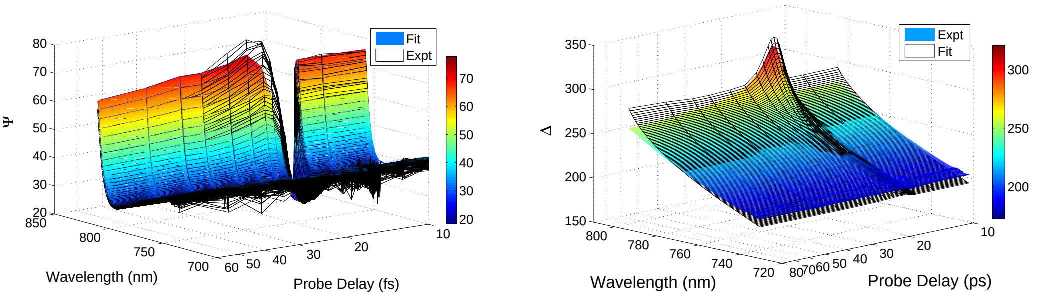

(a) (b)

Figure C.1: (a) Fit for ellipsometric angle Ψ, in samples of *nc-Si:H*, as a function of both probing wavelength λ and probe delay τ (b) Simultaneous fitting of ellipsometric angle Δ for the same parameters.

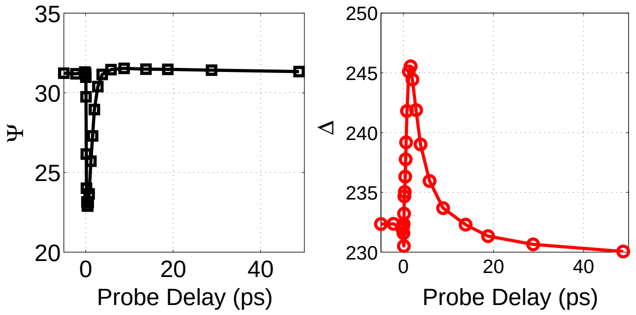

Figure C.2: Ellipsometric parameters of *nc-Si:H*, averaged over the probing bandwidth as a function of the probe delay, revealing quite different characteristic operating timescales for Ψ and Δ.

Figure C.1 shows the quality of fitting for spectroscopic ellipsometry measurements as a function of probe delay. 3D plots show a good fit as a function of the probing wavelength and probe delay for sample of *nc-Si:H*. Fig. C.2: Averaged values of ellipsometric parameters Ψ & Δ over all probing wavelengths. Revealing different timescales for Ψ and Δ.

Fig. C.3 shows the real and imaginary changes of the dielectric function averaged over all probing wavelengths as a function of the probe delay. The dielectric function is plotted for probe delays up to 25ps.

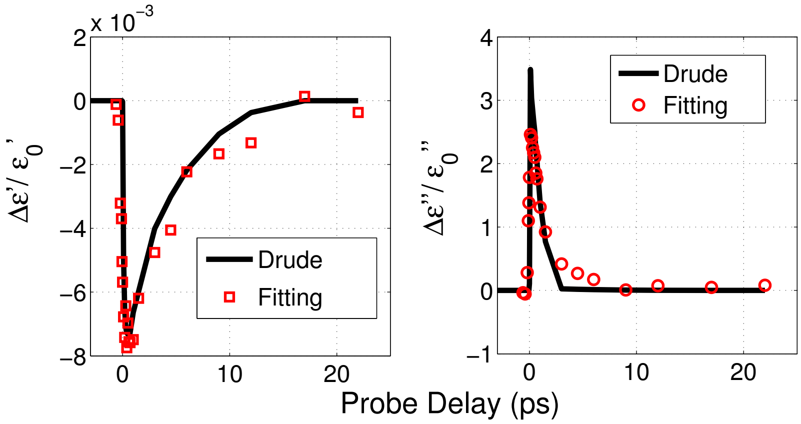

Figure C.3: Change in the real $\Delta\varepsilon'/\varepsilon'_0$ and imaginary $\Delta\varepsilon''/\varepsilon''_0$ components of the dielectric function of *nc-Si:H*, averaged over all probing wavelengths, plotted as a function of probe delay over 25ps following excitation.

Fig. C.4: Ellipsometric angles fitted as a a function of probing wavelength and probe delay for samples of SiN_x.

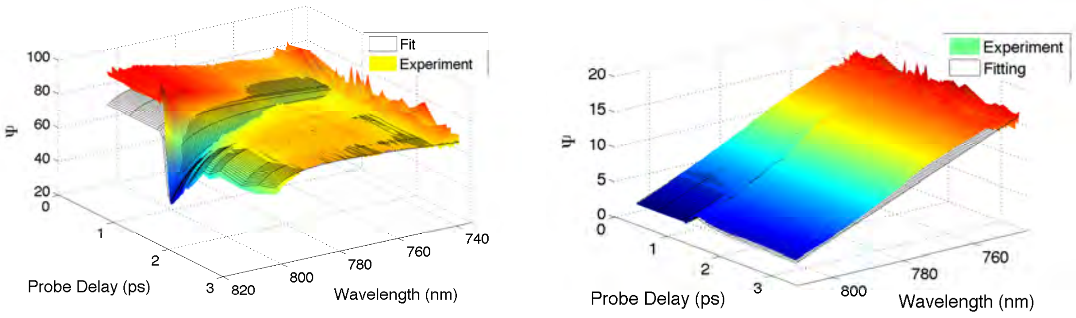

(a) (b)

Figure C.4: (a) Quality of fit for ellipsometric angle Ψ, in samples of SiN_x as a function of both probe wavelength and probe delay. (b) Simultaneous fit for ellipsometric angle Δ.

Fig. C.5: The change in ellispsometric angles for samples of SiN_x averaged over all probing wavelengths.

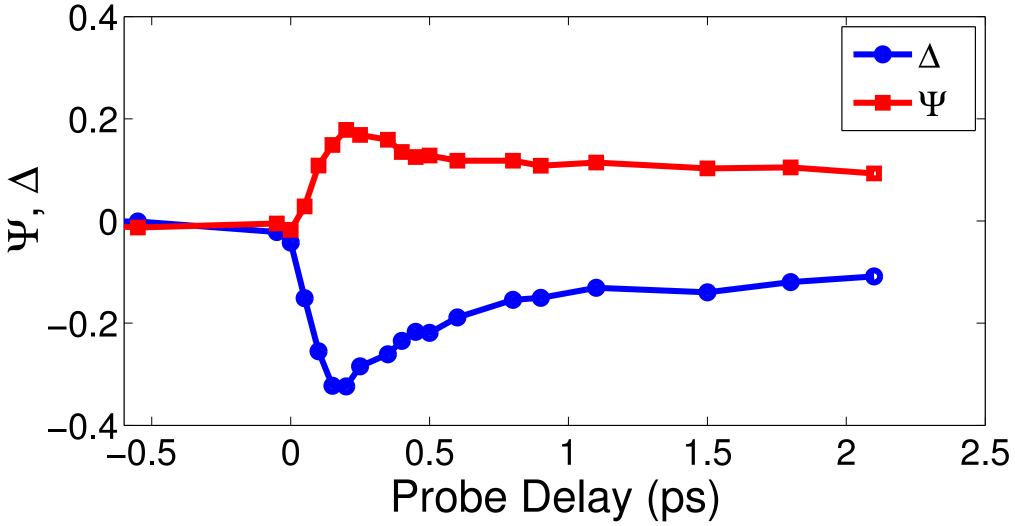

Figure C.5: Average change in Ψ and Δ, in SiN_x, for probe delays up to 2.5ps.

Appendix D

Derivation of RCE intensity

In the following derivation Mueller matrices are utilised to find the intensity detected I in a typical RCE experiment with optical angles $P = 45^\circ$ and $A = 0^\circ$. For a system defined as in Eq. 3.40.

Define the Stoke's parameters in Mueller matrix form.

$$\begin{bmatrix} S_0 \\ S_1 \\ S_2 \\ S_3 \end{bmatrix} \tag{D.1}$$

The Mueller matrices for rotation are;

$$R(\beta) = \begin{bmatrix} 1 & 0 & 0 & 0 \\ 0 & \cos(2\beta) & \sin(2\beta) & 0 \\ 0 & -\sin(2\beta) & \cos(2\beta) & 0 \\ 0 & 0 & 0 & 1 \end{bmatrix} \tag{D.2}$$

Similarly, to rotate the matrix back.

$$R(-\beta) = \begin{bmatrix} 1 & 0 & 0 & 0 \\ 0 & \cos(2\beta) & -\sin(2\beta) & 0 \\ 0 & \sin(2\beta) & \cos(2\beta) & 0 \\ 0 & 0 & 0 & 1 \end{bmatrix} \tag{D.3}$$

For a polariser, P, the Muller matrix,

$$P = \frac{1}{2}\begin{bmatrix} 1 & 1 & 0 & 0 \\ 1 & 1 & 0 & 0 \\ 0 & 0 & 0 & 0 \\ 0 & 0 & 0 & 0 \end{bmatrix} \tag{D.4}$$

For a compensator, C, with retardation δ;

$$C = \begin{bmatrix} 1 & 0 & 0 & 0 \\ 0 & 1 & 0 & 0 \\ 0 & 0 & \cos(\delta) & \sin(\delta) \\ 0 & 0 & -\sin(\delta) & \cos(\delta) \end{bmatrix} \tag{D.5}$$

The matrix for a sample, S, with ellipsometric angles (ψ, Δ) is,

$$S = A\begin{bmatrix} 1 & -\cos(2\psi) & 0 & 0 \\ -\cos(2\psi) & 1 & 0 & 0 \\ 0 & 0 & \sin(2\psi)\cos(\Delta) & \sin(2\psi)\sin(\Delta) \\ 0 & 0 & -\sin(2\psi)\sin(\Delta) & \sin(2\psi)\cos(\Delta) \end{bmatrix} \tag{D.6}$$

where $A = \frac{r_p r_p^* + r_s r_s^*}{2}$ (i.e. the incident intensity I_0).

Putting equations D.1-D.6 into equation 3.40 along with the optical angles and $\delta = \pi/2$ and input Stoke's vector,

$$\text{In} = \begin{bmatrix} S_0 \\ S_1 \\ S_2 \\ S_3 \end{bmatrix} = \begin{bmatrix} 1 \\ 0 \\ 1 \\ 0 \end{bmatrix} \tag{D.7}$$

One finds the output intensity to be;

$$I_{\text{Out}} = \left[\frac{A}{2} + \frac{A}{2}\sin(2C)\cos(2C)\cos(2\psi) - \frac{A}{2}\sin^2(2C)\sin(2\psi)\cos(\Delta) + \frac{A}{2}\cos(2C)\sin(2\psi)\sin(\Delta)\right] \tag{D.8}$$

Using the following trigonometric identities and the ellipsometric definitions of the Stoke's parameters (Eqs. 3.34 & 3.39);

$$\sin(x)\cos(x) = \frac{1}{2}\sin(2x) \qquad \sin^2(x) = \tfrac{1}{2}(1-\cos(2x)) \tag{D.9}$$

The equation to relate detected intensity and the Stoke's parameters is found;

$$I_{\text{out}} = I_0(2 - S_1\sin(4C) - S_2 + S_2\cos(4C) - 2S_3\cos(2C)) \tag{D.10}$$

Appendix E

Deriving the Fermi Integrals

The following section is a summary of calculations of the Fermi integrals given by Ashcroft & Mermin [152]

For a system in thermal equilibrium at temperature T, its properties are calculated by averaging over all possible states of the system. We assign a weight $P(E)$ to the probability that an electron occupies each state E with a Maxwellian distribution e^{-E/k_bT} [152],

$$P(E) = \frac{e^{-E/k_bT}}{\sum e^{-E_\alpha/k_bT}}. \tag{E.1}$$

Here E_α is the energy corresponding to the α^{th} state. We see that the denominator is the partition function, relating to the Helmholtz free energy $F = U - TS$, such that,

$$\sum e^{-E_\alpha/k_bT} = e^{-F_N/k_bT}. \tag{E.2}$$

Thus we are able to recast Eq. E.1 as,

$$P(E) = e^{-(E-F_N)/k_bT}. \tag{E.3}$$

Obeying the Pauli exclusion principle we fill the system one electron at a time, allowing us to define which electron levels are filled, for a given energy E. When operating at thermal equilibrium, the probability f_N that a particular electron level i is filled, is given by the sum of all the independent probabilities that a system of N electrons can take with an electron occupying that level (i),

$$f_N = \sum P_N(E_\alpha). \tag{E.4}$$

The probability that the electron level is unoccupied is just one minus this same function, as, according to Pauli exclusion principle, this is the only two options for the system to be in,

$$f_N = 1 - \sum P_N(E_\gamma), \tag{E.5}$$

where γ represents the number of states the system of electrons can be in, in which the electron level is *not* filled. For a system of $N+1$ electrons in which the extra electron occupies the specific electron level i and all other electrons are left unaltered, we find the state in which the electron level is unoccupied by removing the last electron. We also note that any N electron state with no electron in level i can be constructed from any $N+1$ system *with* an electron in this level. These two states differ only by ε_i, the energy to have an electron in state i. A system of N electrons with an unoccupied level i is the same as a system of $N+1$ electrons with an electron in level i minus the energy to have an electron in that level, which means we can re-write Eq. E.5 [152],

$$f_N = 1 - \sum P(E_\alpha^{N+1} - \varepsilon_i). \tag{E.6}$$

Using Eq. E.3 we find,

$$P(E_\alpha^{N+1} - \varepsilon_i) = e^{(\varepsilon_i - \mu)/k_b T} P_{N+1}(E_\alpha^{N+1}), \tag{E.7}$$

where $\mu = F_{N+1} - F_N$ is the chemical potential. Substitution into Eq. E.6 yields,

$$f_N = 1 - e^{(\varepsilon_i - \mu)/k_b T} \sum P_{N+1}(E_\alpha^{N+1}). \tag{E.8}$$

Thus we find through Eqs. E.4 & E.8 that,

$$f_N = 1 - e^{(\varepsilon_i - \mu)/k_b T} f_{N+1}. \tag{E.9}$$

This equation gives the relation between an N electron system with the electron level i occupied for a given temperature T and a system of $N+1$ electrons under the same conditions. As we consider electron systems of $N \sim 10^{21}$ there is effectively no difference between f_N and f_{N+1}. Solving Eq. E.9 under this assumption provides f_N,

$$f_N = \frac{1}{e^{(\varepsilon_i - \mu)/k_b T} + 1}. \tag{E.10}$$

Given that the dependence of N is governed by the chemical potential (see relation for μ) the number of electrons is given by the sum of probabilities for a given arrangement of electrons f. As the total number of electrons is the sum over all levels, we find the averaged number of electrons in each level,

$$N = \sum_i f = \sum_i \frac{1}{e^{(\varepsilon_i - \mu)/k_b T} + 1}. \tag{E.11}$$

This equation allows us to determine the number of carriers as a function of temperature T and chemical potential μ.

The energies of the electron levels for a given wave vector $\vec{k}$ are given by,

$$\varepsilon(\vec{k}) = \frac{\hbar^2 k^2}{2m}. \tag{E.12}$$

In the independent electron approximation the internal energy of the system U is the sum over all one-electron levels $\varepsilon(\vec{k})$ times the mean number of electrons in each level $f(\varepsilon(\vec{k}))$, so,

$$U = 2\sum_k \varepsilon(\vec{k}) f(\varepsilon(\vec{k})), \tag{E.13}$$

where the constant 2 is due to the spin of electrons. The energy density $u = U/V$ is then given by,

$$u = \int \frac{d\vec{k}}{4\pi^3} \varepsilon(\vec{k}) f(\varepsilon(\vec{k})), \tag{E.14}$$

Similarly the electron density is given by,

$$n = \int \frac{d\vec{k}}{4\pi^3} f(\varepsilon(\vec{k})). \tag{E.15}$$

Integrals of these types can be converted into spherical coordinates to retrieve the carrier concentration,

$$n = \int_{-\infty}^{\infty} d\varepsilon g(\varepsilon) f(\varepsilon) = \frac{(m)^{3/2}}{\sqrt{2}\pi^2\hbar^3} \int_{-\infty}^{\infty} d\varepsilon \frac{\varepsilon^{1/2}}{\exp((\varepsilon-\mu)/k_bT)+1}, \tag{E.16}$$

where $g(\varepsilon) = \frac{m}{\hbar^2\pi^2}\sqrt{\frac{2m\varepsilon}{\hbar^2}}$ is the density of states such that $g(\varepsilon)d\varepsilon = (1/V) \times$ the number of 1-electron energy levels. For the moment we will neglect the slightly different contribution for holes. We may also write down the energy for the system as (see Eq. E.14),

$$\begin{aligned} u = \frac{(\hbar\omega - E_g)}{2} n &= \int_{-\infty}^{\infty} d\varepsilon g(\varepsilon) f(\varepsilon) \varepsilon \\ &= \frac{(m)^{3/2}}{\sqrt{2}\pi^2\hbar^3} \int_{-\infty}^{\infty} d\varepsilon \frac{\varepsilon^{3/2}}{\exp((\varepsilon-\mu)/k_bT)+1}, \end{aligned} \tag{E.17}$$

where ω is the pump frequency and E_g is the band gap of the sample for the corresponding photon energies and we have taken all the non energy-dependent parameters outside of the integral. The term $(\hbar\omega - E_g)/2$ is known as the excess energy Δ.

Appendix F

Temperature & Chemical Potential Calculation

Given Fermi integral equations,

$$n = \frac{(2m_e)^{3/2}}{2\pi^2\hbar^3}\int_0^\infty d\varepsilon \frac{\varepsilon^{1/2}}{\exp(\beta(\varepsilon-\mu_e))+1} \tag{F.1}$$

$$n = \frac{(2m_h)^{3/2}}{2\pi^2\hbar^3}\int_0^\infty d\varepsilon \frac{\varepsilon^{1/2}}{\exp(\beta(\varepsilon-\mu_h))+1} \tag{F.2}$$

$$(\hbar\omega - E_g)n = \frac{(2m_e)^{3/2}}{2\pi^2\hbar^3}\int_0^\infty d\varepsilon \frac{\varepsilon^{3/2}}{\exp(\beta(\varepsilon-\mu_e))+1} + \frac{(2m_h)^{3/2}}{2\pi^2\hbar^3}\int_0^\infty d\varepsilon \frac{\varepsilon^{3/2}}{\exp(\beta(\varepsilon-\mu_h))+1} \tag{F.3}$$

Which can be re-scaled via $x = \beta\varepsilon$, $y_{e(h)} = \beta\mu_{e(h)}$, $\tilde{\beta} = \hbar\omega\beta$ and $\tilde{n} = n/C_e(\hbar\omega)^{3/2}$. Where $C_e = (2m_e)^{3/2}/2\pi^2\hbar^3$.

$$f_1 = \tilde{\beta}^{-3/2}\int_0^\infty dx \frac{x^{1/2}}{\exp(x-y_e)+1} - \tilde{n} \tag{F.4}$$

$$f_2 = m^*\tilde{\beta}^{-3/2}\int_0^\infty dx \frac{x^{1/2}}{\exp(x-y_h)+1} - \tilde{n} \tag{F.5}$$

$$f_3 = \tilde{\beta}^{-5/2}\int_0^\infty dx \frac{x^{3/2}}{\exp(x-y_e)+1} + m^*\tilde{\beta}^{-5/2}\int_0^\infty dx \frac{x^{3/2}}{\exp(x-y_h)+1} - (\tilde{n} - \tilde{E}\tilde{n}) \tag{F.6}$$

Where $m^* = m_h^3/m_e^3$ and $\tilde{E} = E_g/\hbar\omega$. This is solved by iteration of,

$$\begin{pmatrix} y_e \\ y_h \\ \tilde{\beta} \end{pmatrix} = \begin{pmatrix} y_e \\ y_h \\ \tilde{\beta} \end{pmatrix} - \begin{pmatrix} \partial f_1/\partial y_e & \partial f_1/\partial y_h & \partial f_1/\partial \tilde{\beta} \\ \partial f_2/\partial y_e & \partial f_2/\partial y_h & \partial f_2/\partial \tilde{\beta} \\ \partial f_3/\partial y_e & \partial f_3/\partial y_h & \partial f_3/\partial \tilde{\beta} \end{pmatrix}^{-1} \begin{pmatrix} f_1 \\ f_2 \\ f_3 \end{pmatrix} \tag{F.7}$$

Solutions for $\tilde{\beta}$ provide the temperature dependence T on n, while y_e and y_h yield the chemical potential for electrons μ_e and holes μ_h respectively.

Appendix G

Rutherford Scattering for Electron-Electron Collisions

The following sections are a summary of calculations of Rutherford scattering between electrons prepared for a lecture course in plasma physics at M.I.T by Prof. I. Hutchinson [153]

G.1 Binary collisions

Consider equation of motion for two particles,

$$m_1 \ddot{r}_1 = F_{12}; \qquad m_2 \ddot{r}_2 = F_{21}. \tag{G.1}$$

We discuss interactions between particles using (only) the Coulomb force, such that;

$$F_{12} = \frac{e^2}{4\pi\varepsilon_0} \frac{\vec{r}}{r^3}, \tag{G.2}$$

where b is the impact parameter. The stationary target problem shown in Fig. G.1, is solved by considering conservation of angular momentum,

$$m_r r^2 \dot{\theta} = \text{const.} = m_r b v_1. \tag{G.3}$$

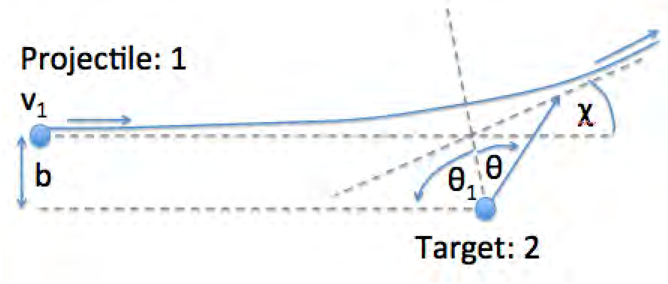

Figure G.1: Collision scheme for calculation of scattering rate between electrons in a classical electron gas dominated by the Coulomb interaction. The projectile scatters from a target at a distance described by the impact parameter, b, at an angle χ.

G.1.1 Cut-off Estimates

When the particles scatter they slow down. The two main routes for relaxation of a particle moving through a background of scatters are,

- Energy loss
- Momentum Loss

Energy loss for electron-electron collisions provide;

$$\frac{dK}{dl} = Kn_2 \frac{m_1 m_2}{(m_1+m_2)^2} 8\pi {b_{90}}^2 \Big[\ln|b| \Big]_{\text{min}}^{\text{max}}, \tag{G.4}$$

where K is the kinetic energy of the particle, b_{90} is the impact parameter resulting in a 90° scattering event. This equation diverges at both $b \to 0$ and $b \to \infty$ due to the approximations used to derive the equations above.

- We are using small angle approximation for scattering events.
- We assume Coulomb force but do not include screening, which is essential for a plasma.

The small angle approximation breaks down at $b = b_{90}$, therefore we should truncate the integral, i.e. ignore results for $b < b_{90}$. For the second approximation we use Debye shielding, which says that in reality the potential varies like,

$$\phi \propto \frac{\exp \frac{-r}{r_D}}{r}. \tag{G.5}$$

So the integral should be cut off at $b = r_D$. These corrections provide the solution,

$$\frac{dK}{dl} = Kn_2 \frac{m_1 m_2}{(m_1 + m_2)^2} 8\pi {b_{90}}^2 \ln|\Lambda|, \tag{G.6}$$

where Λ is given by,

$$\Lambda = \frac{\lambda_D}{b_{90}} = \left(\frac{\varepsilon_0 T_e}{ne^2}\right)^{1/2} \bigg/ \left(\frac{e^2}{4\pi\varepsilon_0 m_r v_1^2}\right), \tag{G.7}$$

and $\ln\Lambda$ is known as the Coulomb logarithm. The energy loss collision frequency is then given by,

$$\tau_K^{-1} = v_1 \frac{1}{K}\frac{dK}{dL} = n_2 v_1 \frac{m_1 m_2}{(m_1 + m_2)^2} 8\pi {b_{90}}^2 \ln|\Lambda|. \tag{G.8}$$

Using equations for $b_{90} = \frac{e^2}{4\pi\varepsilon_0}\frac{1}{m_r v_r^2}$ and m_r into this equation we find,

$$\tau_K^{-1} = n_2 \frac{e^4}{(4\pi\varepsilon_0)^2} \frac{8\pi}{m_1 m_2 v_1^3} \ln\Lambda. \tag{G.9}$$

The energy loss cross section is given by $(1/K)dK/dl = \sigma_K n_2$.

G.2 Thermal Electron-Electron Collisions

We must now consider projectiles and targets with not just one initial velocity but for both species moving, obeying Maxwellian distributions. This requires some heuristic calculations. The Maxwellian distribution is given by,

$$f_e(\vec{v}) = n_e \left(\frac{m_e}{2\pi T_e}\right)^{3/2} \exp\left(-\frac{m(\vec{v} - \vec{v_d})^2}{2T_e}\right). \tag{G.10}$$

where v_d is the drift velocity. The total momentum loss per unit volume,

$$-\frac{dp}{dt} = \int\int \vec{v_r} \frac{m_1 m_2}{m_1 + m_2} v_r 4\pi b_{90}^2 \ln\Lambda f_1 f_2 d^3 v_1 d^3 v_2, \tag{G.11}$$

where $\vec{v_r}$ is the relative velocity $\vec{v_1} - \vec{v_2}$ and b_{90} is given by,

$$b_{90} = \frac{e^2}{4\pi\varepsilon_0}\frac{1}{m_r v_r^2}, \tag{G.12}$$

where m_r is the reduced mass. We now transform to the relative velocity frame. The distribution functions f_j are taken to be shifted Maxwellians in the CoM frame, where j is an integer representing the particle.

$$f_j = n_j \left(\frac{m_j}{2\pi T_e}\right)^{3/2} \exp\left(-\frac{m_j(\vec{v_j}-\vec{v_d})^2}{2T_e}\right), \tag{G.13}$$

where $m_1\vec{v}_{d1} + m_2\vec{v}_{d2} = 0$ and we write down,

$$\begin{aligned} f_1 f_2 = n_1 n_2 \left(\frac{m_1}{2\pi T_e}\right)^{3/2} \left(\frac{m_2}{2\pi T_e}\right)^{3/2} \exp\left(-\frac{m_1 v_1^2}{2T_e} - \frac{m_2 v_2^2}{2T_e}\right) \\ \times \left\{1 + \frac{\vec{v_1} m_1 \overrightarrow{v_d 1}}{T_e} + \frac{\vec{v_2} m_2 \overrightarrow{v_d 2}}{T_e}\right\}, \end{aligned} \tag{G.14}$$

to first order in $\vec{v_d}$. Converting to CoM co-ordinates [1].

$$f_1 f_2 = n_1 n_2 \left(\frac{M}{2\pi T_e}\right)^{3/2} \left(\frac{m_r}{2\pi T_e}\right)^{3/2} \exp\left(-\frac{MV^2}{2T_e} - \frac{m_r v_r^2}{2T_e}\right) \times \left\{1 + \frac{m_r}{T}\vec{v_d}.\vec{v_r}\right\}, \tag{G.15}$$

where $M = m_1 + m_2$. It can be shown that $d^3v_1 d^3v_2 = d^3v_r d^3V$ and we write,

$$\begin{aligned} -\frac{d\vec{p}}{dt} = \int\int \vec{v_r} m_r v_r 4\pi b_{90}^2 \ln\Lambda n_1 n_2 \left(\frac{M}{2\pi T_e}\right)^{3/2} \left(\frac{m_r}{2\pi T_e}\right)^{3/2} \\ \times \exp\left(-\frac{MV^2}{2T_e} - \frac{m_r v_r^2}{2T_e}\right) \times \left\{1 + \frac{m_r}{T}\vec{v_d}.\vec{v_r}\right\} d^3v_r d^3V. \end{aligned} \tag{G.16}$$

Since nothing apart from the exponential term depends on V we perform the integral to

---

[1] To evaluate the integral properly we make some simplifications

- Ignore variations of $\ln\Lambda$ with v and replace with thermal value $\Lambda = \lambda_D/b_{90}(v_1)$
- The drift velocity $\vec{v_d}$ is small relative to the typical thermal velocity

find,

$$-\frac{d\vec{p}}{dt} = \int \vec{v_r} m_r v_r 4\pi b_{90}^2 \ln\Lambda n_1 n_2 \left(\frac{M}{2\pi T_e}\right)^{3/2} \left(\frac{m_r}{2\pi T_e}\right)^{3/2} \exp\left(-\frac{m_r v_r^2}{2\pi}\right) \left\{1 + \frac{m_r}{T_e}\vec{v_d}.\vec{v_r}\right\} d^3 v_r \tag{G.17}$$

The integral is performed by making the substitution $\vec{u} = \vec{v}/v_e$ and $\vec{u_d} = \vec{v_d}/v_e$ where $v_e = \sqrt{T_e/m_e}$ (see appendix H).

$$-\frac{dp}{dt} = v_d v_{rt} m_r 4\pi b_{90}^2(v_{rt}) \ln\Lambda n_1 n_2 \int \frac{u_x^2}{u^3} \hat{f}_0(v_r) d^3\vec{v}_r, \tag{G.18}$$

$$= v_d v_{rt} m_r 4\pi b_{90}^2(v_{rt}) \ln\Lambda n_1 n_2 \frac{2}{3(2\pi)^{3/2}}, \tag{G.19}$$

where $v_{rt} \equiv T_e/m_r$, $b_{90}(vert)$ is the 90° impact parameter evaluated at v_{tr} and $\hat{f}_0$ is the normalised unshifted maxwellian. Which gives,

$$-\frac{dp}{dt} = \frac{2}{3(2\pi)^{1/2}} \left(\frac{e^2}{4\pi\varepsilon_0}\right)^2 \frac{4\pi}{m_r^2 v_{rt}^3} \ln\Lambda n_1 n_2 m_r v_d, \tag{G.20}$$

This is the general result of momentum loss for two Maxwellian distributions drifting through each other with small drift velocity. We then need to fix one species in order to find the collision frequency, such that the momentum density, when species 2 is fixed, is $n_1 m_1 v_d$.

$$\tau_{12}^{-1} = \frac{1}{m_1 n_1 v_d}\frac{dp}{dt} = \frac{2}{3(2\pi)^{1/2}} n_2 \left(\frac{e^2}{4\pi\varepsilon_0}\right)^2 \frac{4\pi}{m_r^2 v_{rt}^3}\frac{\ln\Lambda}{m_1}, \tag{G.21}$$

for electron-electron collisions we see that $m_r = 1/2m_e$ and $v_{rt} = \sqrt{T_e/m_e}$ to find,

$$\tau_{ee}^{-1} = \frac{1}{3\pi^{1/2}} n_e \left(\frac{e^2}{4\pi\varepsilon_0}\right)^2 \frac{4\pi}{m_e^{1/2} T_e^{3/2}} \ln\Lambda. \tag{G.22}$$

However, this equation should be considered carefully, because the electrons are indistinguishable it is not straightforward to define two ‘drifting Maxwellian’ distributions of the same particle. A more specific approach should be taken in order to rigorously prove this.

Appendix H

Useful Integrals

H.1 Spherical Integrals

To solve integral of type,

$$\int \frac{u_x}{u^3} f_0 d^3v \tag{H.1}$$

We use the spherical symmetry of the electron distribution f_0

$$\int \frac{u_x^2}{u^3} f_0 d^3v = \frac{1}{3}\int \frac{u_x^2+u_y^2+u_z^2}{u^3} f_0 d^3v = \frac{1}{3}\int \frac{u_x^2}{u^3} f_0 d^3v \tag{H.2}$$

$$= \frac{1}{3}\int_0^\alpha \frac{v_e}{v} f_0 4\pi v^2 dv \tag{H.3}$$

$$= \frac{2\pi v_e}{3}\int_0^\alpha f_0 2v dv \tag{H.4}$$

$$= \frac{2\pi v_e}{3}\frac{n_e}{(2\pi)^{3/2} v_e^3}\int_0^\alpha \exp\left(-\frac{v^2}{2v_e^2}\right) dv^2 \tag{H.5}$$

$$= \frac{2\pi v_e}{3}\frac{n_e}{(2\pi)^{3/2} 2} = \frac{2}{3(2\pi)^{1/2}} n_e \tag{H.6}$$

H.2 Approximations of Integrals

For an integral of the type,

$$L(\alpha) = \int_0^1 \frac{dx}{x+a} \tag{H.7}$$

When we estimate the order of magnitude for small values of the parameter $\alpha \ll 1$ we break the integral into two parts,

$$L(\alpha) \approx \int_0^\alpha \frac{dx}{\alpha} + \int_\alpha^1 \frac{dx}{x} = 1 + \ln\frac{1}{\alpha} \approx \ln\frac{1}{\alpha} \tag{H.8}$$

Using this approximation the integral is positive for $\alpha \ll 1$ but if you look at the solution at $\alpha = 1/2$ we find a negative answer. But the integral is positive for all α! If we now look at the integrals exact solution,

$$L(\alpha) = \ln\left(1 + \frac{1}{\alpha}\right) \tag{H.9}$$

Now when we look at the solution for $\alpha = 1/2$ we have $L = \ln(3/2) \approx 1$, a positive answer.

References

[1] J. Weiner. *Ultrafast Optics*. Wiley, 2009. 1, 37, 38

[2] B.J. Whitaker. *Imaging in Molecular Dynamics: Technology and Applications*. Cambridge University Press, 2003. 2

[3] K. Sokolowski-Tinten. Timescales in the response of materials to femtosecond laser excitation. *Applied Physics A*, 76:767–769, 2004. 2

[4] A. Esser. Ultrafast recombination and trapping in amorphous silicon. *Physical Review B*, 41(5):2879–2884, 1990. 9, 101

[5] T. Shih, M. T. Winkler, T. Voss, and E. Mazur. Dielectric function dynamics during femtosecond laser excitation of bulk ZnO. *Applied Physics A*, 96(2):363–367, March 2009.

[6] Dzmitry A. Yarotski, Richard D. Averitt, Nicolas Negre, Scott A. Crooker, Antoinette J. Taylor, Giovanni P. Donati, Andreas Stintz, Luke F. Lester, and Kevin J. Malloy. Ultrafast carrier-relaxation dynamics in self-assembled InAs/GaAs quantum dots. *Journal of the Optical Society of America B*, 19(6):1480, June 2002. 2

[7] S. Furukawa and T. Miyassato. Quantum size effects on the optical band gap of microcrystalline Si:H. *Physical Review B*, 38(8):5726–5729, 1988. 2

[8] Valentina Cesari, Wolfgang Langbein, Paola Borri, Marco Rossetti, Andrea Fiore, S. Mikhrin, I. Krestnikov, and A. Kovsh. Ultrafast gain dynamics in 1.3μm InAsGaAs quantum-dot optical amplifiers: The effect of p doping. *Applied Physics Letters*, 90(20):201103, 2007.

[9] H. Benisty. Intrinsic mechanism for the poor luminescence properties of quantum-box systems. *Physical Review B (Rapid)*, 44(19):8–11, 1991.

[10] D.R. Paul and L.M. Robeson. Polymer nanotechnology: Nanocomposites. *Polymer*, 49(15):3187–3204, July 2008.

[11] Amy C. Turner-Foster, Mark A. Foster, Jacob S. Levy, Carl B. Poitras, Reza Salem, Alexander L. Gaeta, and Michael Lipson. Ultrashort free-carrier lifetime in low-loss silicon nanowaveguides. *Optics express*, 18(4):3582–91, February 2010. 2

[12] Andreas Othonos. Probing ultrafast carrier and phonon dynamics in semiconductors. *Journal of Applied Physics*, 83(4), 1998. 3, 4, 9, 86, 102

[13] T. Ichibayashi and K. Tanimura. Ultrafast Carrier Relaxation in Si Studied by Time-Resolved Two-Photon Photoemission Spectroscopy: Intravalley Scattering and Energy Relaxation of Hot Electrons. *Physical Review Letters*, 102(8):1–4, February 2009. 4, 85

[14] H. R. Choo, X. F. Hu, M. C. Downer, and V. P. Kesan. Femtosecond ellipsometric study of nonequilibrium carrier dynamics in Ge and epitaxial Si1-xGex. *Applied Physics Letters*, 2(September):1507–1509, 1993. 100

[15] Bo E. Sernelius. Generalzied Drude approach to the conductivity relaxation time due to electron-hole collisions. *Physical Review B*, 40(18):2–4, 1989. 6, 89

[16] E. Hendry, M. Koeberg, J. Pijpers, and M. Bonn. Reduction of carrier mobility in semiconductors caused by charge-charge interactions. *Physical Review B*, 75(23):4–7, June 2007.

[17] Tae-In Jeon and D. Grischkowsky. Nature of Conduction in Doped Silicon. *Physical Review Letters*, 78(6):1106–1109, February 1997. 4

[18] J-C. Diels. *Ultrashort Laser Pulse Phenomena: Fundamentals, Techniques and Applications on a Femtosecond Time Scale*. Academic Press, 1996. 4, 37, 67

[19] C. V. Shank. Time-resolved reflectivity measurements of femtosecond-optical-pulse-induced phase transitions in silicon. *Physical Review Letters*, 50(6), 1983. 4, 5, 68, 84

[20] M. Lannoo and G. Allan. Theory of radiative and nonradiative transitions for semiconductor nanocrystals. *Journal of Luminescence*, 70:170–184, 1996. 4, 8

[21] M. Kubinyi. Picosecond decay of photoinduced absorption in undoped amorphous and polycrystalline silicon thin films. *Thin Solid Films*, 263(1):99–104, July 1995.

[22] Lu Hu and Gang Chen. Analysis of Optical Absorption in Silicon Nanowire Arrays for Photovoltaic Applications. *Nano Letters*, 7(11), 2007. 4

[23] Rohit P. Prasankumar, Prashanth C. Upadhya, and Antoinette J. Taylor. Ultrafast carrier dynamics in semiconductor nanowires. *Physica Status Solidi (B)*, 246(9):1973–1995, September 2009. 4

[24] V. Klimov, D. McBranch, C. Leatherdale, and M. Bawendi. Electron and hole relaxation pathways in semiconductor quantum dots. *Physical Review B*, 60(19):13740–13749, November 1999.

[25] S. Lyon. Spectroscopy of hot carriers in semiconductors. *Journal of Luminescence*, 35(3):121–154, June 1986.

[26] S. K. Sundaram and E. Mazur. Inducing and probing non-thermal transitions in semiconductors using femtosecond laser pulses. *Nature Materials*, 1(4):217–24, December 2002. 69

[27] M. Alonso, I. Marcus, M. Garriga, A. Goñi, J. Jedrzejewski, and I. Balberg. Evidence of quantum confinement effects on interband optical transitions in Si nanocrystals. *Physical Review B*, 82(4):1–8, July 2010. 4

[28] Po-Chi Ou, Wei-Rein Liu, Ho-Jei Ton, Ja-Hon Lin, and Wen-Feng Hsieh. Ultrafast relaxation and absorption saturation at near exciton resonance in a thin ZnO epilayer. *Journal of Applied Physics*, 109(1):013102, 2011. 5

[29] X. Y. Chen, W. Z. Shen, H. Chen, R. Zhang, and Y. L. He. High electron mobility in well ordered and lattice-strained hydrogenated nanocrystalline silicon. *Nanotechnology*, 17(2):595–599, January 2006.

[30] Clemens Burda, Xiaobo Chen, Radha Narayanan, and Mostafa a El-Sayed. *Chemistry and properties of nanocrystals of different shapes.*, volume 105. ACS Chemical Reviews, April 2005.

[31] Victor I. Klimov. Optical Nonlinearities and Ultrafast Carrier Dynamics in Semiconductor Nanocrystals. *The Journal of Physical Chemistry B*, 104(26):6112–6123, July 2000. 5

[32] A. J. Sabbah and D. M. Riffe. Femtosecond pump-probe reflectivity study of silicon carrier dynamics. *Physical Review B*, 66(165217):1–11, 2002. 5, 65, 68, 76, 78, 80

[33] C. A. D. Roeser, A. M. Kim, J. P. Callan, L. Huang, E. N. Glezer, and Y. Siegal. Femtosecond time-resolved dielectric function measurements by dual-angle reflectometry. *Review of Scientific Instruments*, 74(7):3413–3422, 2003. 5

[34] K. Sokolowski-Tinten. Generation of dense electron-hole plasmas in silicon. *Physical Review B*, 61(4):2643–2650, 2000. 6, 49, 65, 76, 78, 80, 84, 99

[35] J. M. Liu. Picosecond time-resolved plasma and temperature-induced changes of reflectivity and transmission in silicon. *Applied Physics Letters*, 41(7):643, 1982. 6, 68

[36] D. Hulin, M. Combescot, J. Bok, A. Antonetti, and Van Vechten. Energy Transfer during Silicon Irradiation by Femtosecond Laser Pulse. *Physical Review Letters*, 52(22):1998–2001, 1998. 6

[37] Monique Combescot and Roland Combescot. Conductivity relaxation time due to electron-hole collisons in optically excited semiconductors. *Physical Review B*, 35(15):7986–7992, 1987. 6, 9, 89

[38] N. Daldosso and L. Pavesi. Nanosilicon photonics. *Laser & Photonics Review*, 3(6):508–534, November 2009. 6, 7, 89

[39] L. Fekete, P. Kužel, H. Němec, F. Kadlec, A. Dejneka, J. Stuchlík, and A. Fejfar. Ultrafast carrier dynamics in microcrystalline silicon probed by time-resolved terahertz spectroscopy. *Physical Review B*, 79(115306):1–13, March 2009. 6, 84

[40] Lyubov Titova, Tyler Cocker, David Cooke, Xiongyao Wang, Al Meldrum, and Frank Hegmann. Ultrafast percolative transport dynamics in silicon nanocrystal films. *Physical Review B*, 83(8):1–9, February 2011.

[41] L. Bagolini, A. Mattoni, G. Fugallo, and L. Colombo. Quantum Confinement by an Order-Disorder Boundary in Nanocrystalline Silicon. *Physical Review Letters*, 104(17):1–4, April 2010. 40

[42] A. D. Yoffe. Semiconductor quantum dots and related systems: Electronic, optical, luminescence and related properties of low dimensional systems. *Advances in Physics*, 50(1):1–208, January 2001. 6

[43] D. Cooke, A. MacDonald, A. Hryciw, J. Wang, Q. Li, A. Meldrum, and F. Hegmann. Transient terahertz conductivity in photoexcited silicon nanocrystal films. *Physical Review B*, 73(193311), May 2006. 6, 76, 80

[44] K. Shimakawa, T. Itoh, H. Naito, and S. O. Kasap. The origin of non-Drude terahertz conductivity in nanomaterials. *Applied Physics Letters*, 100(13):132102, 2012. 6, 72, 76, 80, 84

[45] Sylvain G. Cloutier, Pavel A. Kossyrev, and Jimmy Xu. Optical gain and stimulated emission in periodic nanopatterned crystalline silicon. *Nat Mater*, 4(12):887–891, 12 2005. 8

[46] W. L. Wilson, P. F. Szajowski, and L. E. Brus. Quantum confinement in size-selected, surface-oxidized silicon nanocrystals. *Science (New York, N.Y.)*, 262(5137):1242–4, November 1993. 8

[47] Rita Spano, Nicola Daldosso, Massimo Cazzanelli, Luigi Ferraioli, Luca Tartara, Jin Yu, Vittorio Degiorgio, Emmanuel Giordana, Jean M. Fedeli, and Lorenzo Pavesi. Bound electronic and free carrier nonlinearities in silicon nanocrystals at 1550nm. *Opt. Express*, 17(5):3941–3950, Mar 2009. 8

[48] Alejandro Martínez, Javier Blasco, Pablo Sanchis, José V. Galán, Jaime García-Rupérez, Emmanuel Jordana, Pauline Gautier, Youcef Lebour, Sergi Hernández, Rita Spano, Romain Guider, Nicola Daldosso, Blas Garrido, Jean Marc Fedeli, Lorenzo Pavesi, and Javier Martí. Ultrafast all-optical switching in a silicon-nanocrystal-based silicon slot waveguide at telecom wavelengths. *Nano Letters*, 10(4):1506–1511, 2010. 8

[49] Fryad Z. Henari, Kai Morgenstern, Werner J. Blau, Vladimir A. Karavanskii, and Vladimir S. Dneprovskii. Third-order optical nonlinearity and all-optical switching in porous silicon. *Applied Physics Letters*, 67(3):323, 1995.

[50] Y. J. Ma, J. I. Oh, D. Q. Zheng, W. A. Su, and W. Z. Shen. Tunable nonlinear absorption of hydrogenated nanocrystalline silicon. *Optics letters*, 36(17):3431–3, September 2011. 8, 38, 85

[51] F. E. Doany, D. Grischkowsky, and C.-C. Chi. Carrier lifetime versus ion-implantation dose in silicon on sapphire. *Applied Physics Letters*, 50(8):460, 1987. 9

[52] A. J. Sabbah and D. M. Riffe. Measurement of silicon surface recombination velocity using ultrafast pump–probe reflectivity in the near infrared. *Journal of Applied Physics*, 88(11):6954–6956, 2000. 9

[53] F. E. Doany and D. Grischkowsky. Measurement of ultrafast hot-carrier relaxation in silicon by thin-film-enhanced, time-resolved reflectivity. *Applied Physics Letters*, 52(1):36–38, 1988. 9

[54] W. Kutt, A. Esser, and K. Seibert. Femtosecond studeis of plasma formation in crystalline and amorphous silcon. *Proc. SPIE*, 1269(154), 1990.

[55] Theodore Sjodin, Hrvoje Petek, and Hai-lung Dai. Ultrafast Carrier Dynamics in Silicon : A Two-Color Transient Reflection Grating Study on a (111) Surface. *Physical Review Letters*, 81(25):1–4, 1998. 9

[56] V. Marecek. The preparation of thin layers of ge and si by chemical hydrogen plasma transport. *Solid-State Electronics*, 11:683–684, 1968. 10

[57] S. Usui and M. Kikuchi. Properties of heavily doped gdsi with low resistivity. *Journal of Non-Crystalline Solids*, 34(1):1 – 11, 1979. 10

[58] W. E. Spear, G. Willeke, P. G. LeComber, and A. G. Fitzgerald. Electronic-properties of microcrystalline silicon films prepared in a glow-discharge plasma. *Journal de Physique*, 42(NC4):257–260, 1981. 10

[59] A. V. Shah, J. Meier, E. Vallat-Sauvain, N. Wyrsch, U. Kroll, C. Droz, and U. Graf. Material and solar cell research in microcrystalline silicon. *Solar Energy Materials and Solar Cells*, 78(1-4):469–491, July 2003. 10, 11

[60] B. E. Warren and B. L. Averbach. The effect of cold-work distortion on x-ray patterns. *Journal of Applied Physics*, 21(6):595–599, 1950. 11

[61] H. P. King and L. E. Alexander. *X-ray Diffraction Procedures*. Wiley, 1981.

[62] C. E. Bouldin, E. A. Stern, B. von Roedern, and J. Azoulay. Structural study of hydrogenated *a*-ge using extended x-ray absorption fine structure. *Phys. Rev. B*, 30:4462–4469, Oct 1984. 11

[63] N. Beck, P. Torres, J. Fric, Z. Remes, A. Prouba, Stuchlikova, N Fejfar, A. Wyrsch, M Vanecek, J. Kocka, and A. Shah. Optical and electrical properties of undoped microcrystalline silicon deposited by the vhf-gd with different dilutions of silane in hydrogen. In *Advances in Microcyrstalline and Nanocrystalline Silicon Semiconductors*, volume 452, pages 761–766. Materials Research Society Symposium Proceedings, 1997. 12

[64] A. Poruba, A. Fejfar, Z. Remes, J. Springer, M. Vanecek, J. Kocka, J. Meier, P. Torres, and A. Shah. Optical absorption and light scattering in microcrystalline silicon thin films and solar cells. *Journal of Applied Physics*, 88(1):148–160, 2000. 11

[65] D. J. Lockwood. *Light Emission in Silicon: Light Emissions in Silicon: From Physics to Devices*, volume 1. Academic Press, 1997. 12

[66] R. W. Collins. Advances in microcyrstalline and amorphous silicon semiconductors. In *MRS Symposium Proceedings*, 1996. 12

[67] R. A. Street. Luminescence in amorphous semiconductors. *Adv. Phys.*, 30(593), 1981. 12

[68] Nae-Man Park, Chel-Jong Choi, Tae-Yeon Seong, and Seong-Ju Park. Quantum Confinement in Amorphous Silicon Quantum Dots Embedded in Silicon Nitride. *Physical Review Letters*, 86(7):1355–1357, February 2001. 12, 13

[69] B. Delley and E. F. Steigmeier. Size dependence of band gaps in silicon nanostructures. *Applied Physics Letters*, 67(16):2370–2372, 1995. 13

[70] G. Allan, C. Delerue, and M. Lannoo. Electronic structure of amorphous silicon nanoclusters. *Phys. Rev. Lett.*, 78:3161–3164, Apr 1997. 13

[71] Kunji Chen, Xinfan Huang, Jun Xu, and Duan Feng. Visible photoluminescence in crystallized amorphous si:h/sin[sub x]:h multiquantum-well structures. *Applied Physics Letters*, 61(17):2069–2071, 1992. 13

[72] X. F. Huang, Z. F. Li, Wu. W, K. J. Chen, X. Y. Chen, and Z. G. Liu. Microstructures and optical properties in crystallized a-si:h multi-quantum wells using excimer laser annealing. *Journal of Non-Crystalline Solids*, 198:821–824, 1996.

[73] Mingxiang Wang, Xinfan Huang, Jun Xu, Wei Li, Zhiguo Liu, and Kunji Chen. Observation of the size-dependent blueshifted electroluminescence from nanocrystalline si fabricated by krf excimer laser annealing of hydrogenated amorphous silicon/amorphous-sin[sub x]:h superlattices. *Applied Physics Letters*, 72(6):722–724, 1998. 13

[74] Nae-Man Park, Tae-Soo Kim, and Seong-Ju Park. Band gap engineering of amorphous silicon quantum dots for light-emitting diodes. *Applied Physics Letters*, 78(17):2575, 2001. 13

[75] D. Chekulaev. *Experimental Study of Ultrafast Carrier Dynamics and Plasmons in Nanostructures*. PhD thesis, University of Birmingham, 2011. 14

[76] M. Molinari, H. Rinnert, and M. Vergnat. Evolution with the annealing treatments of the photoluminescence mechanisms in a-sin[sub x]:h alloys prepared by reactive evaporation. *Journal of Applied Physics*, 101(12):123532, 2007. 13

[77] H.G. Tompkins and W.A. McGahan. *Spectroscopic Ellipsometry and Reflectometry: A User's Guide*. A Wiley-Interscience publication. John Wiley & Sons, 1999. 15

[78] H. Fujiwara. *Spectroscopic Ellipsometry*. John Wiley & Sons, Hoboken, 1st edition, 2003. 15, 17, 20, 31, 35, 41, 53, 54

[79] H. G. Tompkins and E. A. Irene. *Handbook of Ellipsometry*. Springer-Verlag GmbH & Co., 2005. 15, 19

[80] D. Brewster. *Treatise on Optics*. Longman, Rees, Orme, Brown, Green, and Taylor, 1831. 15

[81] K. Seshan. *Handbook of Thin Film Deposition Processes and Technology*. Noyes Publications, Westwood, NJ, 2^{nd} edition, 1999. 16

[82] D. Clarke and J.F. Grainger. *Polarized light and optical measurement*. International series of monographs in natural philosophy. Pergamon Press, 1971. 16, 31

[83] A. M. Taylor. Photoelectric analysis of elliptically polarised light. *University of Southampton*, (1):758–768, 1949. 17

[84] Joungchel Lee, P. I. Rovira, Ilsin An, and R. W. Collins. Rotating-compensator multichannel ellipsometry: Applications for real time Stokes vector spectroscopy of thin film growth. *Review of Scientific Instruments*, 69(4), 1998.

[85] Stefan Zollner, K. D. Myers, J. M. Dolan, D. W. Bailey, and C. J. Stanton. Theory of femtosecond ellipsometry in Ge at 1.5 eV. *Thin Solid Films*, 313-314:568–573, 1998.

[86] Dan Dalacu and Ludvik Martinu. Spectroellipsometric characterization of plasma-deposited Au / SiO 2 nanocomposite films. *Journal of Applied Physics*, 87(1):228–235, 2000. 17

[87] Blaine Johs. Regression calibration method for rotating element ellipsometers. *Thin Solid Films*, 234:395–398, 1993. 17

[88] Rolf H. Muller and Joseph C. Farmer. Fast, self-compensating spectral-scanning ellipsometer. *Review of Scientific Instruments*, 55(3):371–374, 1984. 18

[89] N.M. Bashara, A.B. Buckman, A.C. Hall, and University of Nebraska (Lincoln campus). Electrical Materials Laboratory. *Proceedings of the Symposium on Recent Developments in Ellipsometry: Electrical Materials Laboratory, University of Nebraska, Lincoln, Nebraska, U.S.A., August 7-9, 1968*. North-Holland Publishing Company, 1969. 18

[90] J.C. Maxwell and J.J. Thompson. *A Treatise on Electricity and Magnetism*. Number v. 1 in Clarendon Press series. Clarendon, 1904. 18

[91] R.M.A. Azzam and N.M. Bashara. *Ellipsometry and polarized light*. North-Holland personal library. North-Holland Pub. Co., 1977. 20, 35

[92] P. Drude. Zur elektronentheorie der metalle. *Annalen der Physik*, 306(3), 1900. 24

[93] J. Lee, P. I. Rovira, I. An, and R. W. Collins. Alignment and calibration of the mgf_2 biplate compensator for applications in rotating-compensator multichannel ellipsometry. *J. Opt. Soc. Am. A*, 18:1980, 2001. 25

[94] O. S. Heavens. *Physics of Thin Films*, volume 2. Academic Press, 1964. 26, 46

[95] R. C. Jones. A New Calculus for the Treatment of Optical Systems. *Journal of the Optical Society of America*, 31, 1941. 29, 41

[96] A. Röseler and W. Molgedey. Improvement in accuracy of spectroscopic ir ellipsometry by the use of ir retarders. *Infrared Physics*, 24(1):1–5, 1 1984. 32, 33

[97] J. Shah. *Ultrafast Spectroscopy of Semiconductors and Semiconductor Nanostructures*. Springer Series in Solid-State Sciences. Springer, 1999. 37

[98] Marijn A. M. Versteegh, Tim Kuis, H. T. C. Stoof, and Jaap I. Dijkhuis. Ultrafast screening and carrier dynamics in ZnO: Theory and experiment. *Physical Review B*, 84(3):1–19, July 2011. 38

[99] T. Roger and A. Kaplan. Time-resolved Ellipsometry to Study Extreme Non-equilibrium Electron Dynamics in Nanostructured Semiconductors. *MRS Proceedings Spring Meeting 2012*, 2012. 40, 81

[100] J. H. W. G. Den Boer, G. M. W. Kroesen, and F. J. De Hoog. Spectroscopic rotating compensator ellipsometry in the infrared: retarder design and measurement. *Measurement of science and techology*, 8:484–492, 1997. 42, 44

[101] F. L. McCrackin, E. Passaglia, R. R. Stromberg, and H. J. Steinberg. Measurement of the thickness and refractive index of very thin films and the optical properties of surfaces by ellipsometry. *Journal of Research of the National Bureau of Standards A. Physics and Chemistry*, 67A(4), 1963. 44

[102] M. Ghezzo. Method for calibrating the analyser and the polarizer in an ellipsometer. *Brit. J. Appl. Phys.*, 2(2):1483–1485, 1969. 44

[103] T. Roger, W. He, I. Yurkevich, and A. Kaplan. Enhanced carrier-carrier interaction in optically pumped hydrogenated nanocrystalline silicon. *Applied Physics Letters*, 101(14), 2012. 49, 73, 74, 78, 80, 99

[104] H. Gleiter. Nanostructured materials: basic concepts and microstructure. *Acta Materialia*, 48(1):1–29, 1 2000. 49

[105] T. S. Gates, G. M. Odegard, S. J. V. Frankland, and T. C. Clancy. Computational materials: Multi-scale modeling and simulation of nanostructured materials. *Composites Science and Technology*, 65(15–16):2416–2434, 12 2005.

[106] Iván Mora-Seró, Sixto Giménez, Francisco Fabregat-Santiago, Roberto Gómez, Qing Shen, Taro Toyoda, and Juan Bisquert. Recombination in quantum dot sensitized solar cells. *Accounts of Chemical Research*, 42(11):1848–1857, 2012/09/08 2009.

[107] J. A. Elliott. Novel approaches to multiscale modelling in materials science. *Int. Mat. Rev.*, 56(4):207–225, 2011.

[108] D. Pitsa and M. G. Danikas. Interface features in polymer nanocomposites: A review of proposed models. *Nano*, 06(06):497–508, 2012/09/08 2011. 49

[109] Emmanouil Lioudakis, Andreas Othonos, A. G. Nassiopoulou, Ch. B. Lioutas, and N. Frangis. Influence of grain size on ultrafast carrier dynamics in thin nanocrystalline silicon films. *Applied Physics Letters*, 90(19):191114, 2007. 49, 72

[110] N. C. Greenham, Xiaogang Peng, and A. P. Alivisatos. Charge separation and transport in conjugated-polymer/semiconductor-nanocrystal composites studied by photoluminescence quenching and photoconductivity. *Phys. Rev. B*, 54:17628–17637, Dec 1996.

[111] Qiang Zhang, Tolga Atay, Jonathan R. Tischler, M. Scott Bradley, Vladimir Bulovic, and NurmikkoA. V. Highly efficient resonant coupling of optical excitations in hybrid organic//inorganic semiconductor nanostructures. *Nat Nano*, 2(9):555–559, 09 2007.

[112] Andriy V. Kyrylyuk, Marie Claire Hermant, Tanja Schilling, Bert Klumperman, Cor E. Koning, and Paul van der Schoot. Controlling electrical percolation in multicomponent carbon nanotube dispersions. *Nat Nano*, 6(6):364–369, 06 2011. 49

[113] J. Barreto, T. Roger, and a. Kaplan. Resolving the ultrafast dynamics of charge carriers in nanocomposites. *Applied Physics Letters*, 100(24):241906, 2012. 49, 50, 70, 71, 72, 73, 74, 100

[114] J. C. Maxwell Garnett. Colours in Metal Glasses and in Metallic Films. *Philosophical Transactions of the Royal Society A: Mathematical, Physical and Engineering Sciences*, 203(359-371):385–420, January 1904. 52

[115] Horiba Jobin-Yvon. Semiconductor library. PsiDelta Software, 2012. 53

[116] G. E. Jellison and F. A. Modine. Parameterization of the optical functions of amorphous materials in the interband region. *Applied Physics Letters*, 69(3):371, 1996. 54

[117] A. R. Bloomer and I Forouhi. Optical dispersion relations for amorphous semiconductors and amorphous dielectrics. *Physical Review B*, 34(10), 1986. 54

[118] I Bloomer and A. R. Forouhi. Optical properties of crystalline semiconductors and dielectrics. *Physical Review B*, 38(3):1865–1874, 1988. 54, 55, 56, 57

[119] R. W Collins, Joohyun Koh, H Fujiwara, P. I Rovira, A. S Ferlauto, J. A Zapien, C. R Wronski, and R Messier. Recent progress in thin film growth analysis by multichannel spectroscopic ellipsometry. *Applied Surface Science*, 154–155(0):217–228, 2 2000. 54

[120] R. de L. Kronig and H. A. Kramers. On the theory of absorption and dispersion in the x-ray spectra. *Zeitschrift Fur Physik*, 48(3-4):174–179, 1928. 55

[121] L. Ding, T. Chen, Y. Liu, C. Ng, and S. Fung. Optical properties of silicon nanocrystals embedded in a SiO2 matrix. *Physical Review B*, 72(12):1–7, September 2005. 56, 72

[122] J. Tauc, R. Grigorovici, and A. Vancu. Optical properties and electronic structure of amorphous germanium. *Physica Status Solidi B*, 15(2):627–637, 1966. 56, 58

[123] D. A. G. Bruggemann. Berechnung verschiedener physikalischer konstanten von heterogen substanzen. *Annalen der Physik*, 24:636–679, 1935. 57, 60

[124] Rolf Landauer. The electrical resistance of binary metallic mixtures. *Journal of Applied Physics*, 23(7):779–784, 1952. 57

[125] G. W. Milton. The coherent potential approximation is a realizable effective medium scheme. *Comm. Math.*, 99(4):463–500, 1985. 57

[126] S. Torquato and S. Hyun. Effective-medium approximation for composite media: Realizable single-scale dispersions. *Journal of Applied Physics*, 89(3):1725–1729, 2001. 57

[127] H. Ma, R. Xiao, and P. Sheng. Third-order optical nonlinearity enhancement through composite microstructures. *J. Opt. Soc. Am. B*, 15:1022, 1998. 58

[128] G. W. Milton. *Theory of Composites*. Cambridge University Press, 2002.

[129] A.H. Sihvola and Institution of Electrical Engineers. *Electromagnetic Mixing Formulas and Applications*. IEE Electromagnetic Waves Series. Institution of Electrical Engineers, 1999. 58

[130] Dali Zhang, Elena Cherkaev, and Michael P. Lamoureux. Stieltjes representation of the 3D Bruggeman effective medium and Padé approximation. *Applied Mathematics and Computation*, 217(17):7092–7107, May 2011. 58

[131] B. R. Nag. *Electron Transport in Compound Semiconductors*. Springer Series in Solid State Physics, 1980. 62

[132] Henry M. Van Driel. Kineics of high-density plasmas generated in Si by 1.06- and 0.53-um picosecond laser pulses. *Physical Review B*, 35(15):8166–8176, 1987. 65, 78, 80

[133] A. Esser, H. Heesel, H. Kurz, C. Wang, G. N. Parsons, and G. Lucovsky. Femtosecond spectroscopic study of ultrafast carrier relaxation in hydrogenated amorphous silicon a-Si:H. *Journal of Applied Physics*, 73(3):1235, 1993. 65, 71, 102

[134] M. C. Downer and C. V. Shank. Ultrafast heating of silicon on sapphire by femtosecond optical pulses. *Phys. Rev. Lett.*, 56:761–764, Feb 1986. 65, 71, 75

[135] Ilya A. Shkrob and Robert A. Crowell. Ultrafast charge recombination in undoped amorphous hydrogenated silicon. *Phys. Rev. B*, 57:12207–12218, May 1998. 65, 72

[136] C. F. Bohren. *Absorption and scattering of light by small particles*. Number 6. Wiley, 2009. 66

[137] Jan Valenta, Robert Juhasz, and Jan Linnros. Photoluminescence spectroscopy of single silicon quantum dots. *Applied Physics Letters*, 80(6):1070–1072, 2002. 72

[138] M. Lenner, A. Kaplan, Ch. Huchon, and R. Palmer. Ultrafast laser ablation of graphite. *Physical Review B*, 79(18):1–11, May 2009. 74

[139] J. B. Roy and P. K. Basu. Free carrier absorption in ingaas due to alloy disorder. *physica status solidi (b)*, 167(1):K69–K72, 1991. 79

[140] P. Nozieres and D. Pines. *Theory Of Quantum Liquids*. Number v. 2 in Advanced Book Classics. Westview Press, 1999. 80

[141] L. E. Brus. Electron–electron and electron-hole interactions in small semiconductor crystallites: The size dependence of the lowest excited electronic state. *Soc. Phot-Opt. Instr. Eng.*, 180:23–29, 2005. 80

[142] D. Aspnes. Optical properties of thin films. *Thin Solid Films*, 89(3):249–262, March 1982. 81

[143] P. S. Hauge. Automated Mueller matrix ellipsometry. *Optics Communications*, 17(April):74–76, 1976. 81

[144] E. Lioudakis, A. G. Nassiopoulou, and A. Othonos. Ultrafast carrier dynamics in highly implanted and annealed polycrystalline silicon films. *Journal of Physics: Conference Series*, 10:263–266, January 2005. 84

[145] A. V. Shaposhnikov, I. P. Petrov, V. A. Gritsenko, and C. W. Kim. Electronic band structure and effective masses of electrons and holes in the α and β phases of silicon nitride. *Physics of the Solid State*, 49(9):1628–1632, September 2007. 89

[146] Abram Ioffe Institute. Ioffe website, 2012. 93

[147] D. M. Riffe. Temperature dependence of silicon carrier effective masses with application to femtosecond reflectivity measurements. *Journal of the Optical Society of America B*, 19(5):1092, May 2002. 93, 94

[148] E. M. Lifshitz and L. P. Pitaevski. *Physical Kinetics*. Butterworth-Heinemann, 1981. 93, 94

[149] P. M. Fauchet, D Hulin, R Vanderhaghen, A Mourchid, and W L Nighan Jr. The properties of free carriers in amorphous silicon. *Journal of Non-Crystalline Solids*, 141:76–87, 1992. 99

[150] A. Mourchid, D. Hulin, R. Vanderhaghen, W. L. Nighan Jr, K. Gzara, and P. M. Fauchet. Femtosecond Spectroscopic Determination of the Properties of Free Carriers in a-Si:H. *Solid State Communications*, 74(11):1197–1200, 1990. 99, 102

[151] Chang-ki Min, David G Cahill, and Steve Granick. Time-resolved ellipsometry for studies of heat transfer at liquid/solid and gas/solid interfaces. *Review of Scientific Instruments*, 81(074902):1–7, 2010. 100

[152] N.W. Ashcroft and N.D. Mermin. *Solid state physics*. Science: Physics. Saunders College, 1976. 112, 113

[153] I. H. Hutchinson. Introduction to plasma physics: Chapter 3. Lecture Course / Online, 2001. 118